

UNIVERSITY OF CRETE

DOCTORAL THESIS

**Collective behavior and chimera
states in networks of nonlinear
oscillators and coupled lasers**

Author:

Joniald Shena

Supervisor:

Prof. G. P. Tsironis

*A thesis submitted in fulfillment of the requirements
for the degree of Doctor of Philosophy*

in

Nonlinear and Statistical Physics
Department of Physics

Acknowledgements

I would like to thank my supervisor, Prof. Giorgos Tsironis and Dr. Ioanna Chitzanidi for introducing me to the physics of non-linear phenomena and giving me the opportunity to work on such a fascinating subject. I am grateful for their guidance, encouragement and trust during this work.

A good support system is important for surviving and staying sane during these years. I feel very grateful to my colleagues, the people I worked with, during my stay in Professor Tsironis' group. They were always there to listen and help me giving important advice. Also I want to thank the people of the Physics Department, because every student needs to be close to the best professional in order to be productive and contented while working.

I also want to thank my spiritual friends Nikos, Kyriakos and Aleksandra for our endless scientific discussions and for providing the support and friendship that I needed.

This thesis is dedicated to my family, for being always next to me, helping me and supporting me, even when I turned to be a great trouble and my Anna for her support and understanding.

Contents

Abstract	17
Preface	19
1 Laser dynamics	23
1.1 Introduction	23
1.2 Classical Electromagnetic Fields	25
1.2.1 The paraxial approximation	25
1.2.2 Normal mode expansion of the electromagnetic field in a resonator	27
1.3 The quantum dynamics of the material	32
1.3.1 The atom energy absorption from the electric field . . .	32
1.3.2 The rotating wave approximation	35
1.3.3 The electric dipole interaction	36
1.3.4 The rotating frame and the phenomenological decay terms	38
1.3.5 The density matrix operator	40
1.4 Rate equations	43
1.4.1 Equations for quadratic quantities	43
1.4.2 Adiabatic elimination of the polarization	45

1.4.3	Linear stability	48
1.4.4	Semiconductor lasers	50
1.5	Coupled Lasers	52
1.5.1	Spacial Overlap	52
1.5.2	Optical feedback	53
1.5.3	Eigenmodes of a single waveguide	55
1.5.4	Evanescent waves coupling	58
2	Synchronization and Chimera states	63
2.1	Introduction	63
2.2	The synchronization from individual oscillators to a discrete lattice	64
2.2.1	Synchronization by external action	65
2.2.2	Synchronization of two interacting periodic oscillators	70
2.2.3	Two coupled lasers	73
2.2.4	Synchronization in a discrete lattice	75
2.3	Chimera states	77
2.3.1	Globally coupled oscillators	78
2.3.2	Identical coupled oscillators	80
2.3.3	General coupling function and additional features	83
2.3.4	Experiments and applications	87
3	Turbulent chimeras in large semiconductor laser arrays	91
3.1	Introduction	91
3.2	Coupled semiconductors lasers	93

	7
3.3 Effect of optical frequency detuning	98
3.4 The influence of noise	102
3.5 Suitable measures	102
3.6 Optical frequency detuning and chimera states	105
3.7 Conclusions	107
4 Multi-clustered chimeras in large semiconductor laser arrays with nonlocal interactions	109
4.1 Introduction	109
4.2 The Model	114
4.3 Collective dynamics	118
4.4 Conclusions	123
5 Class B lasers in star networks with optoelectronic feedback	125
5.1 Introduction	125
5.2 The Model and Stability analysis	126
5.3 Two coupled lasers	131
5.4 Star network of coupled lasers	134
5.5 Conclusions	140
A Chimeras classification	145
A.1 The chimeras temporal classification scheme	145

List of Figures

1.1	Energy level diagram for two-level atom, showing decay rates γ_a and γ_b for the probabilities $ C_a ^2$ and $ C_b ^2$	39
1.2	Relaxation oscillations of the laser electric field. From top to bottom $\gamma = 0.001$, $\gamma = 0.0005$ and $\gamma = 0.0001$ where $P = 1.2$	47
1.3	Pitchfork bifurcation for the laser electric field for $\gamma = 0.001$	48
1.4	The Fabry-Perot cavity model with an external cavity to use in deriving the rate equations in the case of optical feedback.	54
2.1	A limit cycle for a two-dimensional dynamical system. The form of it can be any closed curve. The neighboring trajectories are attracted to the cycle. (redrawn from Figure 7.1 of [Arkady et al., 2001])	66
2.2	(a) The synchronization region on the plane of parameters v, ϵ , where the borders of the synchronization region are straight lines. (b) The observed frequency dependence on frequency detuning. (redrawn from Figure 7.4 of [Arkady et al., 2001])	70
2.3	The observed frequencies versus the coupling constant ϵ of five coupled oscillators. The coupling function is $q(x) = \sin x$. Increasing the coupling strength the oscillators starts to form clusters moving gradually to the full synchronization. (redrawn from Figure 11.1 of [Arkady et al., 2001])	75
2.4	The mean frequency in time of the individual oscillators in an array of 100 phase oscillators with random natural frequencies. The coupling function is $q(x) = \sin x$. (a) $\epsilon = 4$. (b) $\epsilon = 1$ and (c) $\epsilon = 0.2$. (redrawn from Figure 11.2 of [Arkady et al., 2001])	76

2.5	(a) Numerical simulations for a typical evolution of K for the Kuramoto model. (b) Dependence of the parameter K on the coupling strength ϵ (redrawn from Figure 2 and 3 of [Strogatz, 2000])	79
2.6	(a) Numerical results of the spatial distribution of the phases obtained for an array of 512 oscillators with periodic boundary conditions. Parameter: $a = 1.457$ and $\epsilon = 4$.(b) Spatial profiles of the long-time average of the order parameter amplitude K . (c) The same for the phase order parameter Θ , (d) and for the actual frequencies. With the blue color we present the numerical results while the red color indicates the theoretical curves. (redrawn from Figure 1 and 2 of [Kuramoto et al., 2002])	81
2.7	The order parameter K over time for 128 coupled oscillators in each population. (a) Stable chimeras, (b) breathing chimeras and (c) long-period breather (redrawn from Figure 2 of [Abrams et al., 2008])	84
2.8	Two chimera trajectors with different initial conditions for 200 oscillators. This difference is very small (10^{-3}) showing the sensitivity in initial conditions. The color coded the time average of the frequency for each oscillator. (redrawn from Figure 2 of [Omel'Chenko et al., 2010])	85
2.9	Transition from a classical chimera state with one incoherent domain to multichimera states with two (a)-(d), and three (c)-(d) incoherent domains. The left column shows snapshot of the amplitude of the FitzHugh-Nagumo oscillator and the right column shows the corresponding time average of each oscillator frequency. From the top to the bottom the range of coupling between the oscillators is decreasing. (redrawn from Figure 4 of [Omelchenko et al., 2013])	86
3.1	Amplitude maxima and minima of the electric field. The coupling strength η has been rescaled to the relaxation oscillation frequency Ω_r . Blue color refers to the first laser and red to the second one. Other parameters are: $T\Omega_r = 20, p = 0.5, \frac{1}{\Omega_r} = 20, a = 5$	94

- 3.2 Snapshots of the amplitude of the electric field in an array of $M = 200$ lasers for different coupling strengths without detuning: (a) $\frac{\eta}{\Omega_r} = 0.006$, (b) $\frac{\eta}{\Omega_r} = 0.01$, (c) $\frac{\eta}{\Omega_r} = 0.02$, (d) $\frac{\eta}{\Omega_r} = 0.07$. Other parameters: $T\Omega_r = 20$, $p = 0.5$, $\frac{1}{\Omega_r} = 20$ and $a = 5$ 97
- 3.3 Extrema of the amplitude of the electric field in dependence of the detuning, for different values of the coupling strength. (a) $\frac{\eta}{\Omega_r} = 0.01$, (b) $\frac{\eta}{\Omega_r} = 0.025$, (c) $\frac{\eta}{\Omega_r} = 0.0635$, (d) $\frac{\eta}{\Omega_r} = 0.08$. The difference in the detuning $\Delta\omega_r$ has been rescaled by the relaxation oscillation frequency Ω_r . Other parameters: $T\Omega_r = 20$, $p = 0.5$, $M = 2$, $\frac{1}{\Omega_r} = 20$ and $a = 5$ 98
- 3.4 a) In the absence of coupling ($\eta = 0$) each laser is a limit cycle with stable amplitude equal to \sqrt{p} and a neutral rotating phase with different frequency ω_j . b) The linear distribution of detunings in space interval. 99
- 3.5 Top: The electric field in the complex unit circle. Bottom: Snapshots of the amplitude of the electric field for different coupling strengths and constant detuning. (a) $H = 0.008$, (b) $H = 0.014$, (c) $H = 0.026$. The red circle denotes the steady state solution of the amplitude of the electric field. Other parameters: $\Delta = 0.01$, $T\Omega_r = 20$, $p = 0.5$, $\frac{1}{\Omega_r} = 20$ and $a = 5$ 101
- 3.6 Snapshots of the amplitude of the electric field for different coupling strengths as in Fig.3.5 (b) with random distribution of detunings and standard deviation equal to $\omega_j/2\Omega_r$ 103
- 3.7 Spatio-temporal evolution of the local curvature for different values of the coupling strength: (a) $H = 0.008$, (b) $H = 0.014$, (c) $H = 0.026$. Other parameters as in Fig. 3.5. 103
- 3.8 $g_0(t)$ over time. (a) $H = 0.008$, (b) $H = 0.014$, (c) $H = 0.026$. Other parameters as in Fig. 3.5. 104

- 3.9 Dependence of the temporal mean $\langle g_0 \rangle_t$ on parameters H and Δ . Points (a) ($H = 0.008, \Delta = 0.01$), (b) ($H = 0.014, \Delta = 0.01$), and (c) ($H = 0.026, \Delta = 0.01$), correspond to Figs. 3.7(a-c). The boundary between full synchronization (red) and full desynchronization (blue) marks the regions where turbulent chimeras emerge. Other parameters as in Fig. 3.5. 106
- 3.10 (a) The temporal mean $\langle g_0 \rangle_t$ as a function of the system size normalized to $\tilde{M} = 1000$. (b) (ϕ_{50}, ϕ_{150}) -projection. Initial phases for all lasers are random and fixed while ϕ_{50} and ϕ_{150} are varied. The color bar shows the value of the temporal mean $\langle g_0 \rangle_t$. Parameters: $H = 0.014, \Delta = 0.01, T\Omega_r = 20, p = 0.5, \frac{1}{\Omega_r} = 20$ and $a = 5$. Other parameters as in Fig. 3.5. 107
- 4.1 Conceptual model of (a) the overlap of the electric fields in nonlocally coupled waveguide lasers, (b) a laser array coupled by a common highly-reflective (HR) mirror via an external cavity. (FAC stands for Fast-Axis Collimating lens). . . . 113
- 4.2 (a) The maxima of intensity in dependence on the delay time τ for a semiconductor laser with optical feedback. Parameters: $p = 1, a = 4, T = 200$, and $k = 0.12$. (b) Blow-up. (Redrawing from P.h.d thesis [Dahms, 2011], Fig.2.5) 116
- 4.3 Bifurcation diagrams of intensity for the first laser as a function of τ . Parameters: $p = 1.155, a = 5, T = 1710$, and $k = 0.135$. (Redrawing from [Junges et al., 2015], Fig.3) 116
- 4.4 (a): Dependence of the temporal mean $\langle g_0(t) \rangle_t$ on parameters k and R . (b): Snapshot of the amplitude of the electric field (left), spatio-temporal evolution of the local curvature (middle), and the local order parameter (right) for fixed $k = 0.21$ and four different coupling ranges: (I) $R = 2$, (II) $R = 9$, (III) $R = 29$, and (IV) $R = 50$. Other parameters: $T = 392, p = 0.23, a = 2.5$, and $C_p = 0$ 117

- 4.5 Dependence of the temporal mean $\langle g_0(t) \rangle_t$ on parameters k and C_p for different values of nonlocal coupling range: (a) $R = 40$, (c) $R = 64$, and (e) $R = 88$. Dependence on parameters R and C_p of the temporal mean $\langle g_0(t) \rangle_t$ for different values of the coupling strength: (b) $k = 0.075$, (d) $k = 0.15$, and (f) $k = 0.225$. Other parameters: $T = 392$, $p = 0.23$, and $a = 2.5$ 119
- 4.6 Dependence of the temporal mean $\langle g_0 \rangle_t$ on parameters k and C_p for different values of nonlocal coupling range: (a) $R = 40$, (b) $R = 64$, and (c) $R = 88$ for $\tau = 1$ with other parameters as in Fig.4.5. 120
- 4.7 The electric field in the complex unit circle (top), spatio-temporal evolution of the local curvature (middle), and spatio-temporal evolution of the local order parameter (bottom) for different coupling ranges and phases: (I) $R = 88, C_p = 0.1\pi, k = 0.15$ (II) $R = 64, C_p = 0.06\pi, k = 0.15$, (III) $R = 40, C_p = 0.1\pi, k = 0.15$, (IV) $R = 27, C_p = 0.1\pi, k = 0.15$, and (V) $R = 64, C_p = 0.4\pi, k = 0.225$. Other parameters: $T = 392, p = 0.23$, and $a = 2.5$ 121
- 4.8 The spatio-temporal evolution of the local curvature for different coupling ranges and phases as in Fig.4.7 for $\tau = 1$ 121
- 5.1 Saddle-node (SN) and Hopf bifurcation stability in terms of the steady state intensity $|E|^2$ and f . (redrawn from Figure 4.6 of [Erneux et al., 2010]) 129
- 5.2 High-gain bifurcation diagram. The figure represents the stationary amplitude of the laser field ($|E|$) versus the bias voltage (B). The thick line marks the stable state interval. With H we denote the Hopf bifurcation point, with LP the saddle node and with BP the branch point of a pitchfork bifurcation. The constant value of B has been indicated by the arrow. Other parameters: $\gamma = 0.003125$, $P = 1.66$, $\beta = 0.0521$, $a = 5.8$, and $f = -0.6$ 130

- 5.3 Schematic diagram of optoelectronic feedback of two coupled lasers. The optical power emitted by the first or the second laser is detected by a photodiode with a fixed bandwidth. The electrical output is fed back to each laser through an amplifier. The remain intensity of each laser, after the beam splitter, has been coupled by the overlap of the electric fields in a nonlinear crystal. 131
- 5.4 a) Stationary amplitude of the laser field for both the first ($|E|$) and the second ($|E_H|$) laser versus the coupling strength. The thick line represent the stable interval. Active and passive states of initial conditions for the first and the second laser respectively, are denoted by the red color and the opposite case by the green color. Passive and passive states are denoted by the black color. The (LP) notation indicates a saddle-node bifurcation where the (BP) a pitchfork bifurcation. b) The top view of (a). The values of the fixed parameters are: $\gamma = 0.003125$, $\beta = 0.0512$, $P = 1.66$, $a = 5.8$, $B = 0.37$ and $f = -0.6$ 133
- 5.5 The limit cycle after the Hopf bifurcation before each branch point as is shown in Fig.5.4. 135
- 5.6 The Floquet multipliers for the limit cycles as is shown in Fig. 5.5. 135
- 5.7 Order parameter Δ_0 in the η - t space for $N = 10$. a) The system starts with periphery passive-hub active, b) periphery passive-hub passive and c) periphery active-hub passive. Other parameters as in Fig.5.4. 137

- 5.8 Phase diagram in the η - N parametric space. Four dynamical regions are separated by curves that correspond to the continuation of the bifurcation points shown in Fig.5.4 using the same colors (red and green are saddle-node bifurcations, while black curve is a pitchfork). In region *I* the coupling is weak enough and all three initial conditions (IC) shown in the inset are stable and constitute steady states of the system. In region *II* the active periphery drifts the hub to the active state. In region *III* the active hub drifts the periphery in the active state. In region *IV* the whole network goes to the active state. In the inset the inner circle represents the hub and the outer circle represents the periphery, while the active state is denoted with blue color and the passive state with yellow. Other parameters are $\gamma = 0.003125$, $\beta = 0.0512$, $P = 1.66$, $a = 5.8$, $B = 0.37$ and $f = -0.6$ 138
- 5.9 Phase diagram in the $\eta - N$ parametric space as in Fig.5.8. The black solid lines correspond to the continuation of the steady states calculated by the Matcont while the red points depict the results from the brutal, fourth order Runge-Kutta integration method of the system. 139
- A.1 The correlation coefficients p_{ij} for the case of turbulent chimeras (see Fig. 3.5 bottom (b)). 148
- A.2 The distribution function h of the absolute values $|p_{ij}|$ 148
- A.3 (a) Snapshot of the amplitude of the amplitude-mediated chimera, (c) Temporal evolution of the modulus, (e) Snapshot of the amplitude of electric field. (b), (d) and (f) $g_0(t)$ and h_0 from the data shown in (a),(d) and (f). 149

Abstract

The synchronization of coupled oscillators is a fascinating demonstration of self-organization which is omnipresent in nature and in many physical phenomena like the collective behavior of coupled metronomes, chemical systems like the Belousov-Zhabotinsky reaction, and technological systems like the synchronization of a power grid. Collective synchrony is crucial in many biological processes like the heart beat or in the human brain where synchronization of neurons is vital for various cognitive tasks. In other situations, oscillators are ordered into chains or lattices, where each element interacts only with its nearest neighbors. Such structures are common for systems like semiconductor laser, where synchronization is important for engineering applications.

Semiconductor laser arrays have been investigated experimentally and theoretically from the viewpoint of temporal and spatial coherence for the past forty years. In this thesis, we are focusing on a rather novel complex collective behavior, namely chimera states, where synchronized clusters of emitters coexist with unsynchronized ones. For the first time, we find such states exist in large diode arrays based on quantum well gain media with nearest-neighbor interactions. By employing a recently proposed figure of merit for classifying chimera states, we provide quantitative and qualitative evidence for the observed dynamics. The corresponding chimeras are identified as turbulent according to the irregular temporal behavior of the classification measure.

For a nonlocal coupling scheme the dynamics of a large array of coupled semiconductor lasers has also been studied numerically. Our focus is again on chimera states. In laser systems, such states have been found for global and nearest-neighbor coupling, mainly in small networks. The technological advantage of large arrays has motivated us to study a system of 200 nonlocally coupled lasers with respect to the emerging collective dynamics. The nonlocal nature of the coupling allows us to obtain robust chimera states

with multiple (in)coherent domains. We find that multiclustered chimera states exist in a wide region of the parameter space and we provide quantitative characterization for the obtained spatiotemporal patterns. By proposing two different experimental setups for the realization of the nonlocal coupling scheme, we are confident that our results can be confirmed in the laboratory.

Finally, we have demonstrated a bistable star network of coupled class B lasers. The theoretical model we use is originated from numerical and experimental studies of a CO_2 laser with an intracavity electro-optic modulator that exhibits bistability. We demonstrate pinning between the peripheral and central elements, an activation spreading where the activated periphery turns on the center element, an activated center which drifts the periphery into the active region and an activation of the whole system from the passive into the active region. Similar dynamical behavior has also been recently found in complex networks of coupled bistable chemical reactions. The current work aims at bringing those novel results from electrochemical networks into the field of laser arrays dynamics.

Preface

Lasers are enabling components in multiple platform applications spanning optical communication networks to laser surgery and sensing. They can be treated as excellent examples of coupled nonlinear oscillators displaying a large variety of useful phenomena. Arrays of coupled lasers are promising devices for applications that require high optical power from a laser source. They are also unstable devices and the main problem is to determine conditions for stable operation (stable phase-locking). Phase locking of an array of diode lasers increases the output power and reduces the overall needed lasing threshold. Recent works include impressive advances in high-speed lasers with low-power consumption, high-power vertical external cavity surface emitting lasers and high-speed beam steering with phased vertical cavity laser arrays. Of special importance for next generation applications such as laser radars, is the design of photonic integrated semiconductor laser arrays that consist of a very large number of properly coupled photonic emitters. Moreover, it is well known that phase locking of an array of diode lasers is a highly effective method in beam shaping because it increases the output power and reduces the overall needed lasing threshold.

The task for a proper lasers modelling may be realized through different levels of sophistication and it requires a full quantum treatment but many laser dynamical properties may be captured by a semiclassical approach. Rather than treating this topic in great depth, the first chapter aims to give the basic elements that we consider necessary for a better understudying of the laser rate equations model before we move to the main part of this thesis which is the dynamical investigation of this model. We have attempted to present a dynamical system suitable for the description of an array of mutually coupled solid states lasers. The meaning of the semi-classical approach is to treat the electromagnetic field purely classically and to describe the active medium with the quantum theory. The connection between these two parts comes through the interaction of radiation with matter in terms of a phenomenological classical polarization.

We start in Chapter 1 by the description of the electromagnetic field from Maxwell equations presenting the wave equation in a medium which play a central role in optical physics and quantum optics. Then, we move inside the optical cavity where by introducing the cavity losses we obtain an equation describing the oscillations forced by the laser medium in the cavity. Then, we discuss the wave functions for atomic systems and study their evolution under the influence of applied perturbations. We use the simple atomic model, the two-level atom subject to a resonant or nearly resonant classical field. After the density matrix representation and through the adiabatic elimination of the polarization we finally get the rate equations for class B lasers. At the end of the chapter, we discuss the theoretical framework needed for a proper coupling between each laser.

The material of Chapter 2 represents the minimum knowledge required to follow the rest of this thesis. It addresses the theory of synchronization and more specifically the idea of chimera states. By synchronization we mean that a large part of the system of oscillators spontaneously locks to a common frequency, forgetting the differences in the natural frequencies of the individual oscillators. Into this frame, the most common behavior is when all oscillators have the same frequency, the so called complete or full synchronization. However, synchronization manifests itself in another scenario where the system splits into synchronized and unsynchronized domains. The last scenario corresponds to the so called "chimera state" where a spatio-temporal pattern of a system of oscillators with identical natural frequencies splits into coexisting regions of locked and unlocked phase.

In this chapter we start by describing a self-sustained oscillator which is interacting with a periodic external force. This interaction may lead to complete locking of the oscillation phase to that of the force. Then we develop a phase dynamics approach for two coupled oscillators that is valid for a weak coupling. The problem here reduces to coupled equations for the phases difference between the two sites. A one-dimensional chain of oscillators is the next step where we assume only nearest neighbour interactions. This approach is a natural generalization of the system of two coupled systems which after a numerical investigation provides cluster formations. Finally, by considering a non-local interaction we demonstrate that N mutually coupled oscillators having different or similar natural frequencies in the presence of a phase-lag term split into coexisting regions of coherent and incoherent

oscillations forming chimera states. At the end of the chapter we present examples and experimental works proving the existence of chimera states into a large range of different fields as well as additional features like breathing and multichimera states.

In Chapter 3 we report our investigation on the emergence of a complex collective behavior, in a large system of coupled semiconductor lasers. This behavior involves the emergence of chimera states which we manage to achieve for large arrays with nearest-neighbor interactions for the first time. The crucial parameters are the coupling strength and the relative detuning between the lasers. By employing very recently developed mathematical measures for classifying chimera states, we provide quantitative evidence of the observed dynamics. A systematic study in the optical frequency detuning and coupling strength parameter space, shows that the region of chimera states lies between full synchronization and desynchronization. A slight change in the initial conditions may produce different values for these measures. However, the range of the obtained values ensures the existence of chimeras, the nature of which is turbulent. Finally, we found out that the system size also has an effect on the calculated values, which saturate for arrays with more than 200 emitters. The present results represent a significant advance in the understanding of the existence criteria for the formation of chimera states and the underlying dynamics responsible for their emergence. Moreover, such investigations provide a path for multiple technological applications for next generation photonic emitters.

Chimera states have been found in a semiconductor laser arrays with global and nearest-neighbor coupling or in the presence of time delays. However, the intermediate case between global and local coupling has never been studied before, e.g., due to experimental difficulties. With our investigation in Chapter 4, we aim to fill this gap. In fact, we provide a full scan of the coupling range (from local to global) and observe regions of different dynamics including smooth wave structures, localized breathers, and turbulent chimeras. Moreover, in our system we manage to observe robust multi-clustered chimeras, i.e. states with multiple (in)coherent domains which we have not found for local coupling. Therefore, apart from the multistability which is crucial for the emergence of the chimera states in all types of coupling, the nonlocality in the coupling kernel used in our case brings additionally the feature of the chimera multiplicity. Another important point of our study is a careful selection of the parameters relevant for experimental

realizations. We suggest two different experimental setups (a wave guide laser and a laser array) and study the effects of three, experimentally accessible parameters: the real and imaginary part of the coupling strength and the range of the coupling.

In Chapter 5 we deal with coupled bistable lasers systems. Such networks of coupled bistable units support the spreading or the retreating of an initial activation, but more interestingly, they support the formation of localized stationary patterns dependent on the coupling strength and the degree distribution of the nodes. Rich dynamical behavior has been recently found in complex networks of coupled bistable chemical reactions and the current work aims at bringing these novel results from electrochemical networks into the field of laser arrays dynamics. Here we have numerically demonstrated a bistable star network of coupled class B lasers that supports stationary patterns and activation spreading determined by the number of coupled lasers to the central unit, by the coupling strength and the initial conditions. This has been applied to a dynamical system of coupled CO_2 lasers with optoelectronic feedback. In our analysis we focus on the simple case where the laser arrays form star networks where each bistable element is connected to a central one, the hub. This connectivity structure is often found in many natural or engineered systems that consist of dynamical elements interacting with each other through a common medium and it has also been used in optically coupled semiconductor lasers where synchronization phenomena were investigated. After careful numerical calculations and by eliminating the phase difference between the central laser and any peripheral unit, we demonstrate a stationary activation between the peripheral and the central elements, a spreading activation of the activated periphery through the center element, a spreading activation from the active center to the peripheral inactivated lasers and an activation of the whole system from the passive into the operative region.

Chapter 1

Laser dynamics

1.1 Introduction

In this chapter we will review the history of the development of solid state lasers and provide a derivation and description of the equations that we use in the whole text of this thesis. We will draw material from original manuscripts as well as studies and established textbooks on photonics.

We develop a dynamical model suitable for the description of an array of mutually coupled solid states lasers. This model considers the propagation of the electric field along the compound system as well as the evolution of the carrier densities within each laser. Phenomenological coupling, passive optical feedback, and in more detail evanescent wave coupling are accounted for in this framework, under weak to moderate coupling conditions. We systematically describe the solid state laser dynamics on the spectrum of monochromatic solutions. By assuming single-longitudinal-mode operation, two level atoms of the active medium, and slowly varying approximation, the dynamical model can be reduced to rate equations. These equations capture the essential features of the response of a single-mode laser and give a good agreement between theory and experiment. For larger coupling, higher-order terms lead to a smaller threshold reduction, reflected itself in the spectrum of the monochromatic solutions and in the dynamics of the optical power.

Modeling lasers may be realized with different ways. Rigorously it requires a full quantum treatment but many laser dynamical properties may be captured by semiclassical or even purely classical approaches. In this thesis we chose the middle point of view, the semi-classical approach, and try

to extract analytically as much information as possible. The meaning of the semi-classical approach is to treat the electromagnetic field purely classically and to describe the active medium with the quantum theory. The connection between these two descriptions comes through the dipole moment of the medium and its interaction with the optical field. The self-consistent set of laser equations for the electromagnetic field and for the state of the medium which interacts with this field will determine the final result of rate equations as well as the structure of this chapter. At the end, we will describe in detail the coupling scheme and the main dynamical properties of those equations.

For a review of this chapter, we will start in section 2 with the description of the electromagnetic field from Maxwell equations. We will present the paraxial approximation and the wave equation in a medium which play a central role in optical physics and quantum optics. Then, we move inside the optical cavity by expanding the field as a superposition of eigenfunctions and eigenmodes. By introducing the cavity losses we obtain equation describing the oscillations forced by the laser medium in the cavity. In section 3 we are concerned with the interaction of classical electromagnetic fields with simple atomic systems. We discuss the wave functions for atomic systems and study their evolution under the influence of applied perturbations. Time dependent perturbation theory and the rotating wave approximation are used to predict transitions from one level (usually the ground state) to an excited state. We use the simple atomic model, the two-level atom subject to a resonant or nearly resonant classical field. We then discuss the nature of the electric-dipole interaction and finally we generalize our treatment by including various kinds of damping with the help of the density operator. After the density matrix representation, we obey in section 4 the Bloch equations for a two level atomic medium and through the adiabatic elimination of the polarization we finally get the rate equations for class B lasers. Then we analyze the basic dynamical properties of rate equations and their linear stability. The case of semiconductor lasers has also been accounted in this section. There, we give a short proof for the deriving of the appropriate rate equations in a more phenomenological approach, without looking into detail. Finally, in section 5 we discuss the theoretical framework needed for a proper coupling between each laser. After an introduction on the phenomenological coupling, we introduce the field rate equations in the presence of an external cavity feedback as well as a great detail of the evanescent wave coupling.

1.2 Classical Electromagnetic Fields

1.2.1 The paraxial approximation

Inside a macroscopic medium, Maxwell's equations are given by:

$$\begin{aligned}\nabla \times \mathcal{E} &= -\frac{\partial B}{\partial t} & \nabla \times D &= p_f \\ \nabla \times H &= J + \frac{\partial D}{\partial t} & \nabla \times B &= 0,\end{aligned}\quad (1.1)$$

where the displacement electric field D is given by

$$D = \epsilon \mathcal{E} + P, \quad (1.2)$$

where the permittivity ϵ includes the contributions of the medium and P is the induced polarization which is splitting, in general, into two parts. The first part is the contribution of all atoms of the medium and can be represented as:

$$P = \epsilon \chi \mathcal{E} \quad (1.3)$$

The second part, comes from the interaction of the field with the active medium. The magnetic field H is given by

$$H = \frac{B}{\mu} - M, \quad (1.4)$$

where μ is the permeability of the medium and M is the magnetization of the medium. In this thesis we will consider only nonmagnetic materials for which $M = 0$. The current density J is often related to the applied electric field \mathcal{E} by the relation $J = \zeta \mathcal{E}$, where ζ is the conductivity of the medium. In the process we find $\nabla \times \nabla \times \mathcal{E} = \nabla(\nabla \cdot \mathcal{E}) - \nabla^2 \mathcal{E}$. In optics $\nabla \cdot \mathcal{E} = 0$, since most of the light field has a slight change along the direction of propagation.

From Eq. 1.1 we arrive at:

$$\nabla^2 \mathcal{E} = \mu \frac{\partial J}{\partial t} + \mu \epsilon \frac{\partial^2 \mathcal{E}}{\partial t^2} + \mu \frac{\partial^2 P}{\partial t^2} \quad (1.5)$$

We can replace $\mu \epsilon$ by $1/c^2$, where c is the speed of light in the medium. Saturation effects slightly complicate the matter since the field inhomogeneities lead to an inhomogeneity of the medium. However, for the majority of quantum electronics systems the wave beams have the form:

$$\begin{aligned} \mathcal{E}(\mathbf{r}, t) &= E(\mathbf{r}, t) e^{-i(\omega t - kz)} \\ P(\mathbf{r}, t) &= \mathcal{P}(\mathbf{r}, t) e^{-i(\omega t - kz)} \end{aligned} \quad (1.6)$$

where ω is the field oscillation frequency and k is a constant vector in the direction of propagation of the field with the magnitude $|k| \equiv \omega/c$. The complex amplitude is a slowly varying function in space and in time, so that Eq. 1.6 describes a monochromatic wave beam. By "slowly varying" we mean that the scale of time for variations in phase, and in amplitude, is much larger than the field oscillation period. These approximation leads to the inequalities

$$\left| \frac{\partial^2 E}{\partial t^2} \right| \ll 2\omega \left| \frac{\partial E}{\partial t} \right| \quad \left| \frac{\partial^2 E}{\partial x_j^2} \right| \ll 2k \left| \frac{\partial E}{\partial x_j} \right| \quad \left| \frac{\partial^2 \mathcal{P}}{\partial t^2} \right| \ll 2\omega \left| \frac{\partial \mathcal{P}}{\partial t} \right|, \quad (1.7)$$

where, by differentiation a few terms of Eq. 1.6, we get:

$$\begin{aligned} \nabla^2 \mathcal{E} &\sim \left(\nabla_{\perp}^2 E - k^2 E + 2ik \frac{\partial E}{\partial z} \right) e^{-i(\omega t - kz)} \\ \frac{\partial \mathcal{E}}{\partial t} &\sim -i\omega E e^{-i(\omega t - kz)} \\ \frac{\partial^2 \mathcal{E}}{\partial t^2} &\sim - \left(\omega^2 E + 2i\omega \frac{\partial E}{\partial t} \right) e^{-i(\omega t - kz)} \\ \frac{\partial^2 P}{\partial t^2} &\sim - \left(\omega^2 \mathcal{P} + 2i\omega \frac{\partial \mathcal{P}}{\partial t} \right) e^{-i(\omega t - kz)} \end{aligned} \quad (1.8)$$

Inserting Eq. 1.8 into the wave Eq. 1.5 we arrive at a parabolic equation:

$$\nabla_{\perp}^2 E + 2i \left(k \frac{\partial E}{\partial z} + \frac{\omega}{c^2} \frac{\partial E}{\partial t} \right) + i\omega\mu\zeta E + \left(\frac{\omega^2}{c^2} - k^2 \right) E = -\mu\omega^2 \mathcal{P} - i2\omega\mu \frac{\partial \mathcal{P}}{\partial t} \quad (1.9)$$

In general, the polarization \mathcal{P} is a complex field with a real and an imaginary part and here we are interested only in the imaginary part. Moreover, the latter assumes its simplest form when the dispersion law $\omega = ck$ is valid. After this simplification, we take the imaginary part and we have

$$\frac{\partial E}{\partial z} + \frac{1}{c} \frac{\partial E}{\partial t} + \frac{\zeta}{2c\epsilon} E = -\frac{k}{2\epsilon} \mathcal{P} \quad (1.10)$$

This equation play a central role in optical physics and quantum optics. It tell us how light propagates through a medium and specifically how the imaginary parts of the polarization act. The real part has to do with the phase velocity with which the electromagnetic wave propagates in the medium. The effects described by this phase are those associated with the index of refraction of the medium, such as dispersion and self focusing and are not showing in this thesis. What is shown is the field amplitude that is driven by the imaginary part of the polarization. This component gives rise to absorption and emission.

1.2.2 Normal mode expansion of the electromagnetic field in a resonator

Consider the electric field E and the magnetic field H inside a volume V bounded by a surface S of perfect conductivity. This mean that the real boundary conditions on the metallized (S_1) and the open (S_2) areas of the surface are replaced by the ideal ones $(\mathbf{n} \times E)_{s_1} = 0$ and $(\mathbf{n} \times H)_{s_2} = 0$. We will expand E and H in terms of two orthonormal sets of vector fields E_{λ} and H_{λ} , respectively:

$$\begin{aligned} E(\mathbf{r}, t) &= \sum e_\lambda(t) E_\lambda(\mathbf{r}) \\ H(\mathbf{r}, t) &= \sum h_\lambda(t) H_\lambda(\mathbf{r}) \end{aligned} \quad (1.11)$$

This system obey the relations [Hall et al., 1970]:

$$\begin{aligned} k_\lambda E_\lambda &= \nabla \times H_\lambda \\ k_\lambda H_\lambda &= \nabla \times E_\lambda \end{aligned} \quad (1.12)$$

If we take the curl of both sides and neglect the $\nabla \cdot E$ or $\nabla \cdot H$, using the identity $\nabla \times \nabla \times A = \nabla(\nabla \cdot A) - \nabla^2 A$ we have:

$$\begin{aligned} \nabla^2 E_\lambda + k_\lambda^2 E_\lambda &= 0 \\ \nabla^2 H_\lambda + k_\lambda^2 H_\lambda &= 0 \end{aligned} \quad (1.13)$$

The functions $E_\lambda(\mathbf{r})$ and $H_\lambda(\mathbf{r})$ are orthogonal and satisfy the normalization conditions [Yariv, 1989]:

$$\int_{V_c} E_\lambda E_\mu dV = V_c \delta_{\lambda\mu} \quad \int_{V_c} H_\lambda H_\mu dV = V_c \delta_{\lambda\mu} \quad (1.14)$$

From the paraxial approximation Eq. 1.8 and from the definition of the field expansion Eq. 1.11, the time-dependent expansion coefficients satisfy the equations,

$$\frac{d^2 e_\lambda}{dt^2} + \omega_\lambda^2 e_\lambda = 0 \quad \frac{d^2 h_\lambda}{dt^2} + \omega_\lambda^2 h_\lambda = 0 \quad (1.15)$$

where $\omega_\lambda = k_\lambda c$.

We now turn to free oscillations in a real cavity. In the absence of the

bulk losses the field in such a cavity can be approximated by a series Eq. 1.11 which is the system of equations for an ideal cavity. In order to find the expansion for $\nabla \times E$ we make use of the vector identity:

$$\begin{aligned}\nabla(E \times \nabla \times E_\lambda) &= (\nabla \times E)(\nabla \times E_\lambda) - E \cdot \nabla \times \nabla \times E_\lambda \\ \nabla(E \times k_\lambda H_\lambda) &= k_\lambda H_\lambda (\nabla \times E) - E \cdot \nabla \times (k_\lambda H_\lambda) \\ \nabla(E \times H_\lambda) &= H_\lambda (\nabla \times E) - k_\lambda E E_\lambda\end{aligned}\quad (1.16)$$

Integrating this identity over the volume and using the Gauss divergence theorem we arrive at:

$$\begin{aligned}\int_V \nabla(E \times H_\lambda) dV &= \int_V H_\lambda (\nabla \times E) dV - k_\lambda \sum e_\mu \int_V E_\mu E_\lambda dV \\ \int_S \mathbf{n}(E \times H_\lambda) dS &= \int_V H_\lambda (\nabla \times E) dV - k_\lambda e_\lambda V_c\end{aligned}\quad (1.17)$$

Since,

$$\begin{aligned}\frac{1}{V_c} \sum H_\lambda \int_V H_\lambda (\nabla \times E) dV &= \frac{1}{V_c} \sum H_\lambda \int_V H_\lambda \sum e_\mu \nabla \times E_\mu dV \\ &= \frac{1}{V_c} \sum H_\lambda \int_V H_\lambda \sum e_\mu k_\mu H_\mu dV \\ &= \frac{1}{V_c} \sum H_\lambda e_\lambda k_\lambda V_c \\ &= \sum e_\lambda k_\lambda H_\lambda \\ &= \sum e_\lambda (\nabla \times E_\lambda) \\ &= \nabla \times E\end{aligned}\quad (1.18)$$

we get:

$$\begin{aligned}
\nabla \times E &= \frac{1}{V_c} \sum H_\lambda \left[\int_S \mathbf{n}(E \times H_\lambda) dS + k_\lambda e_\lambda V_c \right] \\
&= \sum H_\lambda \left[k_\lambda e_\lambda + \frac{1}{V_c} \int_{S_1} (\mathbf{n} \times E) H_\lambda dS \right]
\end{aligned} \tag{1.19}$$

In similar way, it is easy to see the validity of:

$$\nabla \times H = \sum E_\lambda \left[k_\lambda h_\lambda + \frac{1}{V_c} \int_{S_2} (\mathbf{n} \times H) E_\lambda dS \right] \tag{1.20}$$

Introducing the expansions Eq. 1.11, into Eq. 1.1 we get:

$$\begin{aligned}
\nabla \times H &= \sigma E + \epsilon \frac{\partial E}{\partial t} + \frac{\partial P}{\partial t} \\
&= \sigma \sum e_\lambda E_\lambda + \epsilon \sum \frac{\partial e_\lambda}{\partial t} + \frac{\partial P}{\partial t}
\end{aligned} \tag{1.21}$$

From Eq. 1.20 and making use of the orthonormality relations Eq. 1.14 we have

$$\frac{de_\lambda}{dt} + \frac{\sigma}{\epsilon} e_\lambda - \frac{k_\lambda h_\lambda}{\epsilon} = \frac{1}{V_c} \int_{S_2} (\mathbf{n} \times H) E_\lambda dS + \int_{V_c} \frac{\partial P}{\partial t} E_\lambda dV \tag{1.22}$$

In the same way, from Eq. 1.19 we get

$$\frac{dh_\lambda}{dt} + \frac{k_\lambda \epsilon_\lambda}{\mu} = -\frac{1}{\mu V_c} \int_{S_1} (\mathbf{n} \times E) H_\lambda dS \tag{1.23}$$

Then, differentiating the first equation with respect to time we eliminate the function dh_λ/dt and arrive at:

$$\begin{aligned} \frac{d^2 e_\lambda}{dt^2} + \frac{\sigma}{\epsilon} \frac{de_\lambda}{dt} + k_\lambda^2 c^2 e_\lambda &= -\frac{k_\lambda c^2}{V_c} \int_{S_1} (\mathbf{n} \times \mathbf{E}) H_\lambda dS \\ &+ \frac{1}{V_c} \int_{S_2} (\mathbf{n} \times \mathbf{H}) E_\lambda dS + \int_{V_c} \frac{\partial^2 P}{\partial t^2} E_\lambda dV \end{aligned} \quad (1.24)$$

For an ideal cavity the surface integrals of the above equation are equal to zero. In a real cavity, the bulk losses can be given from [Khanin, 1995] into these forms,

$$\begin{aligned} \frac{k_\lambda c^2}{V_c} \int_{S_1} (\mathbf{n} \times \mathbf{E}) H_\lambda dS &= \frac{\omega_\lambda}{Q_s} \frac{de_\lambda}{dt} \\ -\frac{1}{V_c} \int_{S_2} (\mathbf{n} \times \mathbf{H}) E_\lambda dS &= \frac{\omega_\lambda}{Q_e} \frac{de_\lambda}{dt} \\ \frac{\omega \sigma}{\epsilon} &= Q_v \end{aligned} \quad (1.25)$$

where the quantity Q_s represents the cavity losses due to the absorption by the walls of the cavity, Q_e describes the cavity losses from emission through the holes in the cavity and finally Q_v represents the bulk losses in the medium within the cavity. Moreover, with the notion of a net Q-factor ($1/Q = 1/Q_s + 1/Q_e + 1/Q_v$), we can rewrite Eq. 1.24 in a more simple form:

$$\frac{d^2 e_\lambda}{dt^2} + \frac{\omega_\lambda}{Q} \frac{de_\lambda}{dt} + \omega_\lambda^2 e_\lambda = \int_{V_c} \frac{\partial^2 P}{\partial t^2} E_\lambda dV \quad (1.26)$$

For this equation, we consider solutions which are nearly harmonic oscillations with a slowly varying amplitude and phase [Andronov et al., 1949],

$$e_\lambda = \frac{1}{2} \left[F_\lambda(t) e^{-i\omega t} + F_\lambda^*(t) e^{i\omega t} \right] \quad (1.27)$$

where the complex amplitude of the polarization component can be introduced through the equality:

$$\int_V P E_\lambda dV = \frac{1}{2} \left[P_\lambda(t) e^{-i\omega t} + P_\lambda^*(t) e^{i\omega t} \right] \quad (1.28)$$

Substituting Eq. 1.28, Eq. 1.27 into Eq. 1.26 and with the approximations a) the field damping in a cavity to be small ($\omega \ll Q$) and b) the frequency of each mode to be very close to the main frequency ($\omega_\lambda \sim \omega$) we arrive at the abbreviated equations

$$\frac{dF_\lambda}{dt} + [\kappa + i(\omega_\lambda - \omega)] F_\lambda = i\omega P_\lambda \quad (1.29)$$

where $\kappa = \omega_\lambda/2Q$.

1.3 The quantum dynamics of the material

1.3.1 The atom energy absorption from the electric field

The interaction between the radiation of the electric field with bound electrons can be described from the electric dipole ($e\mathbf{r}$). The electric dipole is defined as a pair of opposite charges of magnitude (e) times the distance between them (\mathbf{r}) with a direction from the negative to the positive charge. With this operator, we can bring together the quantum mechanical description of a system with the polarization of the medium. The final one can be treated as a classical quantity from the Maxwell's equations. By definition from quantum mechanics the expectation value of $e\mathbf{r}$ takes the form,

$$\langle e\mathbf{r} \rangle = \int e\mathbf{r} |\psi(\mathbf{r}, t)|^2 d^2r \quad (1.30)$$

where $\psi(\mathbf{r}, t)$ is the well known wave function. From the Schrödinger equation,

$$i\hbar \frac{\partial}{\partial t} \psi(\mathbf{r}, t) = \mathbf{H}_0 \psi(\mathbf{r}, t) \quad (1.31)$$

the time and space dependencies of the wave equation can be written as,

$$\psi_n(\mathbf{r}, t) = u_n(\mathbf{r}) e^{-i\omega_n t} \quad (1.32)$$

where \hbar is the Planck constant divided by 2π and \mathbf{H}_0 is the Hamiltonian of an atom which is not interacting with the electric field. By the method of separation of variables, we can quantify $u_n(\mathbf{r})$ as the set of variables which satisfy the energy eigenvalue equation

$$\mathbf{H}_0 u_n(\mathbf{r}) - \hbar\omega_n u_n(\mathbf{r}) = 0 \quad (1.33)$$

The eigenfunctions $u_n(\mathbf{r})$ have the property to be orthonormal and complete that is,

$$\int u_n^*(\mathbf{r}) u_m(\mathbf{r}) d^3r = \delta_{nm} \quad (1.34)$$

$$\sum_n u_n^*(\mathbf{r}) u_n(\hat{\mathbf{r}}) = \delta(\mathbf{r} - \hat{\mathbf{r}}) \quad (1.35)$$

where δ_{nm} and $\delta(\mathbf{r} - \hat{\mathbf{r}})$ are the Kronecker and Dirac delta functions, respectively. Now, the wave function itself $\psi(\mathbf{r}, t)$, due to the fact that the Schrödinger equation is linear, can be written as the superposition of the $\psi_n(\mathbf{r}, t)$:

$$\psi(\mathbf{r}, t) = \sum_n C_n(t) u_n(\mathbf{r}) e^{-i\omega_n t} \quad (1.36)$$

This is a crucial step. The coefficients $C_n(t)$, when the atom is not interacting with the electric field, are in general time independent and the Hamiltonian of that system satisfies Eq. 1.33. In our case however, the time dependence plays the role of a small additional interaction to the initial Hamiltonian. Such a modified Hamiltonian wouldn't satisfy Eq. 1.33 and this is the reason for the coefficients time dependency. The square of the absolute value of those coefficients ($|C_n(t)|^2$) is nothing else but the probability that the system is in the n - th energy state.

To find the expectation value of Eq. 1.30 in terms of the $C_n(t)$, we simply insert Eq. 1.36 into Eq. 1.30. This gives:

$$\int (\mathbf{e}\mathbf{r})|\psi(\mathbf{r},t)|^2 = \sum_{n,m} C_m^*(t)C_n(t)e^{-i(\omega_m-\omega_n)t} \int u_m^*(\mathbf{r})(\mathbf{e}\mathbf{r})u_n(\mathbf{r})d^3r \quad (1.37)$$

The small additional interaction is the electromagnetic field. Suppose that this interaction is equal to V . Then the total Hamiltonian of the system will be $\mathbf{H} = \mathbf{H}_0 + \mathbf{V}$. Now, the other important step is to expand the wave function in terms of eigenfunctions of the initial Hamiltonian (\mathbf{H}_0), holding the probability amplitudes time dependent. This gives

$$\begin{aligned} i\hbar \frac{\partial}{\partial t} \psi(\mathbf{r},t) &= \mathbf{H}\psi(\mathbf{r},t) \\ i\hbar \frac{\partial}{\partial t} \sum_m C_m(t)u_m(\mathbf{r})e^{-i\omega_m t} &= (\mathbf{H}_0 + \mathbf{V}) \sum_m C_m(t)u_m(\mathbf{r})e^{-i\omega_m t} \\ i\hbar \sum_m (\dot{C}_m(t) - i\omega_m C_m(t))e^{-i\omega_m t} &= \sum_m C_m(t)\hbar\omega_m u_m(\mathbf{r})e^{-i\omega_m t} + \sum_m C_m(t)\mathbf{V}u_m(\mathbf{r})e^{-i\omega_m t} \\ i\hbar(\dot{C}_n(t) - i\omega_n C_n(t))e^{-i\omega_n t} &= C_n(t)\hbar\omega_n e^{-i\omega_n t} + \sum_m C_m(t) \int u_n^*(\mathbf{r})\mathbf{V}u_m(\mathbf{r})d^3r e^{-i\omega_m t} \\ \dot{C}_n(t) &= -\frac{i}{\hbar} \sum_m C_m(t)e^{i(\omega_n-\omega_m)t} \int u_n^*(\mathbf{r})\mathbf{V}u_m(\mathbf{r})d^3r \end{aligned} \quad (1.38)$$

This equation shows how the probability amplitudes for the wave function changes in time. In particular, the changes of C_n describe how an atom absorbs energy from an electric field. This is the well known time dependent perturbation theory. In a more strict form the proceed is by writing \mathbf{V} as a small interaction $\varepsilon\mathbf{V}$ and the wave function as an expansion over those small perturbations $\psi \sim \psi^0 + \varepsilon\psi^1 + \varepsilon^2\psi^2 + \dots$. First-order perturbation theory is obtained by equating terms proportional to ε , secondorder terms proportional to ε^2 , and so on. One can then set $\varepsilon = 1$ at the end of the calculation.

1.3.2 The rotating wave approximation

One very important question in a quantum system is the knowledge of the probability for an initially unexcited atom to be excited in an upper level. This can be done, in our case, by the interaction with an electromagnetic field. Starting with the time equal to zero, the wave function has the initial value,

$$\psi(\mathbf{r}, 0) = u_j(\mathbf{r}) \quad (1.39)$$

where $C_j(0) = 1$ and $C_{n \neq j}(0) = 0$. In that way, we can find the first-order correction of the C_n which is:

$$\dot{C}_n(t) \sim -\frac{i}{\hbar} \int u_n^*(\mathbf{r}) \mathbf{V} u_j(\mathbf{r}) d^3r e^{i(\omega_n - \omega_j)t} \quad (1.40)$$

This equation can be easily integrated for two important cases: one for constant \mathbf{V} and one for sinusoidal such that $\mathbf{V} = V_0 \cos(\Omega t)$. For the first case it can be prove that with the increasing of the frequency differences $\omega_n - \omega_j$ the probability for a transition to the first upper level becomes smaller rapidly. This means that transitions are much more likely if the energy is conserved between initial and final states. In this thesis, we will analyse the sinusoidal interaction, which is frequently used for the interaction between the atom with a monochromatic electromagnetic field. From Eq. 1.40 we have:

$$\dot{C}_n(t) \sim -\frac{i}{\hbar} \cos(\Omega t) e^{i(\omega_n - \omega_j)t} \int u_n^*(\mathbf{r}) V_0 u_j(\mathbf{r}) d^3r \quad (1.41)$$

If we rewrite $\cos(\Omega t) = 1/2(e^{i\Omega t} + e^{-i\Omega t})$ we can easily find the solution which is:

$$C_n(t) \sim -\frac{i}{2\hbar} \left[\frac{e^{i(\omega_n - \omega_j - \Omega)t} - 1}{i(\omega_n - \omega_j + \Omega)} + \frac{e^{i(\omega_n - \omega_j + \Omega)t} - 1}{i(\omega_n - \omega_j - \Omega)} \right] \int u_n^*(\mathbf{r}) V_0 u_j(\mathbf{r}) d^3r \quad (1.42)$$

This value is accurate so long as $C_n(t)$ doesn't change a lot from the initial

value $C_n(0) = 1$. Now, in the case of positive detuning ($\omega_n - \omega_j \geq 0$), the denominator ($\omega_n - \omega_j + \Omega$) is always larger than the detuning. In the opposite case, if $\omega_n - \omega_j \sim \Omega$, the other denominator ($\omega_n - \omega_j - \Omega$) vanishes. This observation occurs only if the previous resonant condition is satisfied. Then, the term with the small denominator is much larger than that with the large value, allowing us to neglect the latter. For the same reason, we can probably neglect transitions to levels with energies very different from $\hbar\Omega$ and this remark is used to justify the two-level atom approximation. Neglecting the term with the relatively large denominator is called the rotating wave approximation. With this approximation Eq. 1.42 takes the simplest form:

$$C_n(t) \sim -\frac{i}{2\hbar} \left[\frac{e^{i(\omega_n - \omega_j + \Omega)t} - 1}{i(\omega_n - \omega_j - \Omega)} \right] \int u_n^*(\mathbf{r}) V_0 u_j(\mathbf{r}) d^3r \quad (1.43)$$

With this calculation we can see that after some time the transitions to the upper level are unlikely to occur unless the detuning between the two energy levels is approximately equal to the applied field frequency. This result is totally different with the case of a constant electromagnetic field where, as we mentioned before, the probability for a transition is proportional to the increase of the detuning.

1.3.3 The electric dipole interaction

So far, we have assumed that the electromagnetic field has sinusoidal expression. Here, we will construct the Hamiltonian of the interaction between a light field and a bound atom proving that it is very close to the previous hypothesis. We will start by the principle of minimum coupling, which states that the canonical momentum \mathbf{p} of a particle of charge q is no longer its kinetic momentum $m\dot{\mathbf{r}}$, as is the case for a free particle, but rather $\mathbf{p} = m\dot{\mathbf{r}} + q\mathbf{A}(\mathbf{r})$, where $\mathbf{A}(\mathbf{r})$ is the vector potential of the magnetic field. With the introduction of potential we can write the electric and magnetic field in the form:

$$\begin{aligned} \mathbf{E} &= -\frac{\partial \mathbf{A}}{\partial t} - \nabla U \\ \mathbf{B} &= \nabla \times \mathbf{A} \end{aligned} \quad (1.44)$$

where $U(\mathbf{r})$ is the scalar potential.

The interaction between an optical field and a charge q which is bounded to an atomic nucleus by a potential $V(\mathbf{r})$ is then given in the non-relativistic limit by the Hamiltonian:

$$\mathbf{H} = -\frac{1}{2m} [\mathbf{p} - q\mathbf{A}(\mathbf{r}, t)]^2 + qU(\mathbf{r}, t) + V(\mathbf{r}) \quad (1.45)$$

We can work in the so-called radiation gauge, where $U(\mathbf{r}, t) = 0$ and $\nabla \cdot \mathbf{A}(\mathbf{r}, t) = 0$ [Pierre et al., 2007; Nagourney, 2014]. In addition, we exploit the fact that in most problems in quantum optics, the wavelength of the optical field is large compared to the size of an atom, so we can evaluate the vector potential at the location \mathbf{R} of the nucleus rather than at the location \mathbf{r} of the electron. This approximation allows us to treat the field as constant over the dimensions of the atom, and is called the electric dipole approximation.

From the quantum representation of the canonical momentum $p = -i\hbar\nabla$, the Schrödinger equation becomes then:

$$i\hbar \frac{\partial \psi(\mathbf{r}, t)}{\partial t} = \left[-\frac{\hbar^2}{2m} \left[\nabla - \frac{iq}{\hbar} \mathbf{A}(\mathbf{R}, t) \right]^2 + V(\mathbf{r}) \right] \psi(\mathbf{r}, t) \quad (1.46)$$

The statement of local gauge invariance, requires that the physical predictions of our theory must remain unchanged under the gauge transformation ($\psi(\mathbf{r}, t) \rightarrow \psi(\mathbf{r}, t)e^{i\varphi(\mathbf{r}, t)}$). Via the gauge transformation

$$\psi(\mathbf{r}, t) = e^{(-iq\mathbf{r}/\hbar)\mathbf{A}(\mathbf{R}, t)} \phi(\mathbf{r}, t) \quad (1.47)$$

where $\phi(\mathbf{r}, t)$ is a new wave function. If we replace in Eq. 1.45 the wave equation with the above equation, after some calculations and using the fact that $\mathbf{E}(\mathbf{R}, t) = -\partial\mathbf{A}(\mathbf{R}, t)/\partial t$, we find that,

$$\phi(\mathbf{r}, t) = [H_0 - q\mathbf{r}\mathbf{E}(\mathbf{R}, t)] \phi(\mathbf{r}, t) \quad (1.48)$$

where $H_0 = \frac{\mathbf{p}^2}{2m} + V(\mathbf{r})$ is the unperturbed Hamiltonian of the electron. This shows that the interaction between the electron and the electromagnetic

field is described by the interaction \mathcal{V} which is given by:

$$\mathcal{V} = -q\mathbf{r}\mathbf{E}(\mathbf{R}, t) \quad (1.49)$$

The matrix element of the dipole operator between different levels is:

$$e\mathbf{r}_{mn} = \int u_m^*(\mathbf{r})e\mathbf{r}u_n(\mathbf{r})d^3r \quad (1.50)$$

Matrix elements of \mathbf{r} between different states can also vanish, but we are interested in two levels a and b between which the matrix element does not vanish. We can then write the electric-dipole interaction matrix element in the form,

$$\begin{aligned} \mathcal{V}_{ab} &\equiv \int u_a^*(\mathbf{r})\mathcal{V}u_b(\mathbf{r})d^3r \\ &= -\mathbf{E}(\mathbf{R}, t) \int u_b^*(\mathbf{r})e\mathbf{r}u_b(\mathbf{r})d^3r \equiv \mathbf{E}(\mathbf{R}, t)\mathbf{d}_{ab} \end{aligned} \quad (1.51)$$

where \mathbf{d}_{ab} is the component of $e\mathbf{r}_{ab}$ along \mathbf{E} . For simplicity, we ignore the spatial dependence into this section, and use $\mathbf{E}(\mathbf{R}, t) \sim \mathbf{E}(t)$.

1.3.4 The rotating frame and the phenomenological decay terms

We will treat the atoms using the two-level approximation. We will ignore the fact that levels usually have a number of sublevels that all can contribute to a resonant transition. We emphasize the two-level atom because we can often describe its interaction with the electromagnetic field in detail and obtain analytic solutions. We indicate by a the upper level and by b the lower one (see Fig. 1.1). The corresponding wave function is then

$$\psi(\mathbf{r}, t) = C_a(t)e^{-i\omega_a t}u_a(\mathbf{r}) + C_b(t)e^{-i\omega_b t}u_b(\mathbf{r}) \quad (1.52)$$

We will assume that the field is given by a plane wave with frequency Ω approximately equal to the two-level transition frequency $\omega = \omega_a - \omega_b$.

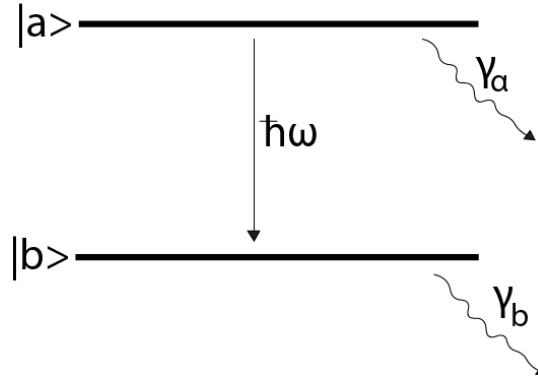


FIGURE 1.1: Energy level diagram for two-level atom, showing decay rates γ_a and γ_b for the probabilities $|C_a|^2$ and $|C_b|^2$.

Having in our mind the rotating-wave approximation we keep only the $\frac{1}{2}e^{-i\Omega t}$ term from $\cos(\Omega t)$ and always for $\omega > 0$. Hence, the electric-dipole interaction matrix element takes the form

$$\mathcal{V}_{ab} \sim -\frac{1}{2}E_0 e^{-i\Omega t} d_{ab} \quad (1.53)$$

Equation. 1.49 and Eq. 1.50 depend upon two very high optical frequencies (ω and Ω) and upon two slowly varying quantities (C_a and C_b). This disparate time dependences can be resolved if we place the wave function Eq. 1.49 into the rotating frame by the transformation [Nagourney, 2014; Landau et al., 1977]:

$$\begin{bmatrix} C_a \\ C_b \end{bmatrix} = \begin{bmatrix} e^{i\delta t/2} & 0 \\ 0 & e^{-i\delta t/2} \end{bmatrix} \begin{bmatrix} C_a \\ C_b \end{bmatrix} \quad (1.54)$$

Then, Eq. 1.49 takes the form,

$$\psi(\mathbf{r}, t) = C_a(t) e^{i(\frac{1}{2}\delta - \omega_a)t} u_a(\mathbf{r}) + C_b(t) e^{i(-\frac{1}{2}\delta - \omega_b)t} u_b(\mathbf{r}) \quad (1.55)$$

where $\delta = \omega - \Omega$.

Substituting this expansion into the Schrödinger equation and projecting onto the eigenfunctions u_a and u_b we find:

$$\begin{aligned}\dot{C}_a &= \frac{1}{2}i \left(-\delta C_a + \frac{E_0 d_{ab}}{\hbar} C_b \right) \\ \dot{C}_b &= \frac{1}{2}i \left(\delta C_b + \frac{E_0 d_{ba}}{\hbar} C_a \right)\end{aligned}\tag{1.56}$$

Moreover, the populations of excited atomic levels have the property to decay because of collisions and other phenomena. The lifetimes of these decays can be described quite well by adding phenomenological decay terms to the Eq. 1.53. For a more explicit description we need a quantum treat of the electromagnetic field which is beyond the semiclassical approach. Hence, into the frame of this approach we write

$$\begin{aligned}\dot{C}_a &= -\frac{1}{2}(\gamma_a + i\delta)C_a + i\frac{E_0 d_{ab}}{2\hbar}C_b \\ \dot{C}_b &= -\frac{1}{2}(\gamma_b - i\delta)C_b + i\frac{E_0 d_{ba}}{2\hbar}C_a\end{aligned}\tag{1.57}$$

where γ_a and γ_b are the decay constants of each state respectively.

1.3.5 The density matrix operator

The previous level decay causes the two-level probability amplitudes to decrease exponentially in time, thereby destroying the wave function's normalization. Moreover, we want to generalize our treatment of two-level systems to include various kinds of damping. Some of these can be put directly into the equations of motion for the probability amplitudes. However, two important kinds cannot: upper to lower level decay, and more rapid decay of the electric dipole than the average level decay rate. For these two damping mechanisms, we need a more general description than can be provided by the state vector. Specifically, we need to consider systems for which we do not possess the maximum knowledge allowed by quantum mechanics. In other words, we do not know the state vector of the system, but rather the classical probabilities for having various possible state vectors. We consider the system that is part of a larger closed system and the last one is in some state described by a wave function with coordinates those of the closed and

the open system. In such situations we introduce the density matrix operator ρ see [Pierre et al., 2007; Landau et al., 1977].

Hence for the two-level system we write the wave function with the Schrödinger picture amplitudes C_a and C_b in the form

$$\psi(\mathbf{r}, t) = C_a(t)u_a(\mathbf{r}) + C_b(t)u_b(\mathbf{r}) \quad (1.58)$$

or equivalently by the state vector

$$|\psi(t)\rangle = C_a(t)|a\rangle + C_b(t)|b\rangle \quad (1.59)$$

where the representation of the wave function for a state vector has the form $\psi(\mathbf{r}, t) = \langle \mathbf{r} | \psi \rangle$ and for any n base $u_n(\mathbf{r}) = \langle \mathbf{r} | n \rangle$. The corresponding density operator is defined as the projector $\rho = \langle \psi | \psi \rangle$ onto this state, and the density matrix elements $\rho_{ab} = \langle a | \psi \rangle \langle \psi | b \rangle$ are given by the bilinear products $\rho_{aa} = \langle a | \psi \rangle \langle \psi | a \rangle = C_a C_a^* = |C_a|^2$ which is the probability of being in the upper level, $\rho_{ab} = \langle a | \psi \rangle \langle \psi | b \rangle = C_a C_b^*$ which is the dimensionless complex dipole, $\rho_{ba} = \langle b | \psi \rangle \langle \psi | a \rangle = C_b C_a^* = \rho_{ab}^*$ and $\rho_{bb} = \langle b | \psi \rangle \langle \psi | b \rangle = C_b C_b^* = |C_b|^2$ which is the probability of being in lower level.

Now, for more simplicity, instead of the form Eq. 1.36, we can also expand the wave function as $\psi(\mathbf{r}, t) = \sum_n c_n(t)u_n(\mathbf{r})$ for which the $\hbar\omega_n$ time dependence in Eq. 1.36 doesn't cancel out. Then, the coefficients $c_a(t)$ and $c_b(t)$, including phenomenological decays out of the rotative frame, obeys the equations of motion,

$$\begin{aligned} \dot{c}_a &= -(i\omega_a + \gamma_a/2)c_a - i\hbar^{-1}V_{ab}c_b \\ \dot{c}_b &= -(i\omega_b + \gamma_b/2)c_b - i\hbar^{-1}V_{ba}c_a \end{aligned} \quad (1.60)$$

where $V_{nm} = \langle n | V | m \rangle = \mathcal{V}_{nm}$ as in Eq. 1.51, is the whole interaction between the atom and the optical field. Proceeding one element at a time, we have:

$$\begin{aligned}
\dot{\rho}_{aa} &= \dot{c}_a c_a^* + c_a \dot{c}_a^* \\
&= -(i\omega_a + \gamma_a/2)|c_a|^2 - i\hbar^{-1}V_{ab}c_b c_a^* - (-i\omega_a + \gamma_a/2)|c_a|^2 + i\hbar^{-1}V_{ba}c_a c_b^* \\
&= -\gamma_a \rho_{aa} - i\hbar^{-1}(V_{ab}\rho_{ba} - V_{ba}\rho_{ab})
\end{aligned} \tag{1.61}$$

Similarly, we find,

$$\dot{\rho}_{bb} = -\gamma_b \rho_{bb} + i\hbar^{-1}(V_{ab}\rho_{ba} - V_{ba}\rho_{ab}) \tag{1.62}$$

and for the off-diagonal element,

$$\begin{aligned}
\dot{\rho}_{ab} &= \dot{c}_a c_b^* + c_a \dot{c}_b^* \\
&= -(i\omega_a + \gamma_a/2)c_a c_b^* - i\hbar^{-1}V_{ab}c_b c_b^* - (-i\omega_b + \gamma_b/2)c_a c_b^* + i\hbar^{-1}V_{ab}c_a c_a^* \\
&= -(i\omega + \gamma_{ab})\rho_{ab} + i\hbar^{-1}V_{ab}(\rho_{aa} - \rho_{bb})
\end{aligned} \tag{1.63}$$

where $\omega = \omega_a - \omega_b$ and $\gamma_{ab} = \frac{1}{2}(\gamma_a + \gamma_b)$. Elastic collisions between atoms in a gas or between phonons and atoms in a solid can cause ρ_{ab} to decay separately from the diagonal elements. To include this phenomena we take the classical average over all collisions and we add this correction to the gamma parameter ($\gamma_{ab} + \gamma_{ph}$). For typographical simplicity, we drop the average notation, but we should always remember that ρ includes such classical averages. For a brief discussion of this phenomena see [Pierre et al., 2007].

1.4 Rate equations

1.4.1 Equations for quadratic quantities

Let us represent the field as a sum of quasi-monochromatic components, the frequencies of which are ω^{mn} where $\omega^a - \omega^b = \Omega$

$$\mathbf{E}(\mathbf{r}, t) = \frac{1}{2} \left(F_{aa}(\mathbf{r}, t) + F_{ab}(\mathbf{r}, t)e^{-i\Omega t} + F_{ba}(\mathbf{r}, t)e^{i\Omega t} + F_{bb} \right) \quad (1.64)$$

The elements of the density matrix in this field can be presented then as:

$$\rho_{mn}(t) = \sigma_{mn}(t)e^{-i\omega^{mn}t} \quad (1.65)$$

Then, from Eq. 1.51 and from Eq. 1.61, 1.62, 1.63 we have

$$\begin{aligned} \dot{\sigma}_{aa} &= -\gamma_a \sigma_{aa} - \frac{i}{2\hbar} (d_{ab} F_{ab} \sigma_{ba} - d_{ba} F_{ba} \sigma_{ab}) \\ \dot{\sigma}_{bb} &= -\gamma_b \sigma_{bb} + \frac{i}{2\hbar} (d_{ab} F_{ab} \sigma_{ba} - d_{ba} F_{ba} \sigma_{ab}) \\ \dot{\sigma}_{ab} &= -[\gamma_{ab} - i(\Omega - \omega)] \sigma_{ab} - \frac{i}{2\hbar} d_{ab} F_{ab} (\sigma_{bb} - \sigma_{aa}) \end{aligned} \quad (1.66)$$

Slightly changing the notation: $D = \sigma_{bb} - \sigma_{aa}$, $\gamma_{ab} = \gamma_{\perp}$, $\sigma_{ba} = \sigma^*$ and $\sigma_{ab} = \sigma$ we obtain a set of two equations:

$$\begin{aligned} \dot{\sigma} + [\gamma_{\perp} - i(\Omega - \omega)] \sigma &= -\frac{i}{2\hbar} d F D \\ \dot{D} + \gamma_{\parallel} (D - D_0) &= \frac{i}{\hbar} (d F \sigma^* - d^* F^* \sigma) \end{aligned} \quad (1.67)$$

where $\gamma_{\parallel} (D - D_0) = (\gamma_b \sigma_{bb} - \gamma_a \sigma_{aa})$ and D_0 is unsaturated value of D which corresponds to $F = 0$.

Now, in terms of the density matrix, the expectation value $\langle e\mathbf{r} \rangle$ is given by,

$$\langle e\mathbf{r} \rangle = \rho_{aa}d_{aa} + \rho_{ab}d_{ba} + \rho_{ba}d_{ab} + \rho_{bb}d_{bb} = \text{tr}(\rho\mathbf{d}) \quad (1.68)$$

for a single atom. The polarization for the whole material is $\mathbf{P} = N_{tot}\text{tr}(\rho\mathbf{d})$ where with N_{tot} we denote the number of molecules in a unit volume.

Combining Eq. 1.68, Eq. 1.64 and Eq. 1.65 with Eq. 1.10 and assuming $\mathbf{d} \parallel \mathbf{F}$, and that the dipole moment matrix is real ($d_{ab} = d_{ba} = d$), we arrive at a scalar model of a traveling wave laser:

$$\begin{aligned} \frac{\partial F}{\partial z} + \frac{1}{c} \frac{\partial F}{\partial t} + \left(\frac{\xi}{2c\epsilon} - i\Omega \right) &= -\frac{k}{\epsilon} N_{tot} \sigma d \\ \frac{\partial \sigma}{\partial t} + [\gamma_{\perp} - i(\Omega - \omega)] \sigma &= -\frac{i}{2\hbar} d F D \\ \frac{\partial D}{\partial t} + \gamma_{\parallel} (D - D_0) &= \frac{i}{\hbar} d (F \sigma^* - F^* \sigma) \end{aligned} \quad (1.69)$$

while combining Eq. 1.68, Eq. 1.64 and Eq. 1.65 with Eq. 1.29 we arrive a set of equations for the modal amplitudes:

$$\begin{aligned} \frac{\partial F_{\lambda}}{\partial t} + [\kappa + i(\omega_{\lambda} - \Omega)] F_{\lambda} &= i\omega d N_{tot} \frac{1}{V_c} \int \sigma E_{\lambda}(\mathbf{r}) dV \\ \frac{\partial \sigma}{\partial t} + [\gamma_{\perp} - i(\Omega - \omega)] \sigma &= -\frac{i}{2\hbar} d D \sum E_{\lambda} F_{\lambda} \\ \frac{\partial D}{\partial t} + \gamma_{\parallel} (D - D_0) &= -\frac{id}{2\hbar} (F_{\lambda}^* \sigma - F_{\lambda} \sigma^*) E_{\lambda} \end{aligned} \quad (1.70)$$

We now turn to a laser model expressed by Eq. 1.69 . If the losses for the separate cavity elements (mirrors) are small then we can assume $\partial F/\partial z = 0$. Without fixing the normalization factor t we will introduce the dimensionless variables and coefficients

$$\begin{aligned}
\tau &= \frac{t}{\hat{t}} & f &= \frac{\partial F}{\hbar} (2\gamma_{\perp}\gamma_{\parallel})^{-\frac{1}{2}} & n &= \frac{2d^2\omega_0 c\epsilon}{\hbar\gamma_{\perp}\zeta} N_{tot} D \\
p &= \frac{2dc\epsilon\omega_0}{\hbar\zeta} (2\gamma_{\perp}\gamma_{\parallel})^{-\frac{1}{2}} N_{tot} \sigma & A &= \frac{2d^2c\epsilon\omega_0}{\hbar\gamma_{\perp}\zeta} N_{tot} D^0 & \hat{\kappa} &= \frac{\zeta\hat{t}}{2c\epsilon} \\
\hat{\gamma}_j &= \gamma_j \hat{t} & \Delta_0 &= \frac{\Omega - \omega}{\gamma_{\perp}} & \Delta_c &= -\frac{2(\Omega)c\epsilon}{\zeta}
\end{aligned} \tag{1.71}$$

where $\omega_0 = ck$. It is most convenient to choose a normalization factor t comparable with a characteristic time scale of the time-dependent laser action. The wide variety of options requires to take an individual approach in each particular case. If the notation of Eq. 1.71 is used, then the equations become:

$$\begin{aligned}
\frac{df}{d\tau} &= i\hat{\kappa}\Delta_c f \hat{\kappa}(p - f) \\
\frac{dp}{d\tau} &= i\hat{\gamma}_{\perp}\Delta_0 p \hat{\gamma}_{\perp}(nf - p) \\
\frac{dn}{d\tau} &= \hat{\gamma}_{\parallel} \left[A - n - \frac{1}{2}(f^*p + fp^*) \right]
\end{aligned} \tag{1.72}$$

1.4.2 Adiabatic elimination of the polarization

The complex form of the Eq. 1.72 is most compact but not always convenient. It is often necessary to return to the real variables by using the real and imaginary parts of f and p . As real variables we can also use the quadratic quantities:

$$m = |f|^2 \quad r = |p|^2 \quad s = \frac{1}{2}(fp^* + f^*p) \quad q = \frac{i}{2}(fp^* - f^*p) \tag{1.73}$$

These variables are related to each other and to n by five equations:

$$\begin{aligned}
\frac{dm}{d\tau} &= 2\hat{k}(s - m) \\
\frac{dn}{d\tau} &= \hat{\gamma}_{\parallel}(A - n - s) \\
\frac{dr}{d\tau} &= 2\hat{\gamma}_{\perp}(ns - r) \\
\frac{ds}{d\tau} &= -(\hat{\gamma}_{\perp} + \hat{k})s + \hat{\gamma}_{\perp}\Delta_{0c}q + \hat{\gamma}_{\perp}mn + \hat{k}r \\
\frac{dq}{d\tau} &= -(\hat{\gamma}_{\perp} + \hat{k})q - \hat{\gamma}_{\perp}\Delta_{0c}s
\end{aligned} \tag{1.74}$$

where $\Delta_{0c} = 2\Omega - \omega$.

In general, it becomes possible to reduce the number of differential equations by adiabatic elimination of part of the variables when a subspace with a smaller number of dimensions, in which fast motions are absent, is distinguished in the phase space of the system. Starting from arbitrary initial conditions, the representative point rapidly passes into this subspace and then it moves along the phase space trajectories localized in it. Mathematically the motion in the system described by,

$$\mu\dot{x}_i = F_i(x, y) \qquad \dot{y}_j = G_j(x, y) \tag{1.75}$$

where μ is a small parameter, differs little from the motion in a limiting system:

$$F_i(x, y) = 0 \qquad \dot{y}_j = G_j(x, y) \tag{1.76}$$

In our system the parameters looks like $\hat{\gamma}_{\perp} \gg \hat{\gamma}_{\parallel}$ and $\hat{\gamma}_{\perp} \gg \hat{k}$. Hence, we perform the standard procedure of adiabatic elimination of r , s and q putting $dr/d\tau = ds/d\tau = dq/d\tau = 0$. Then, substituting these relations into the first two equations of Eq. 1.74, we find:

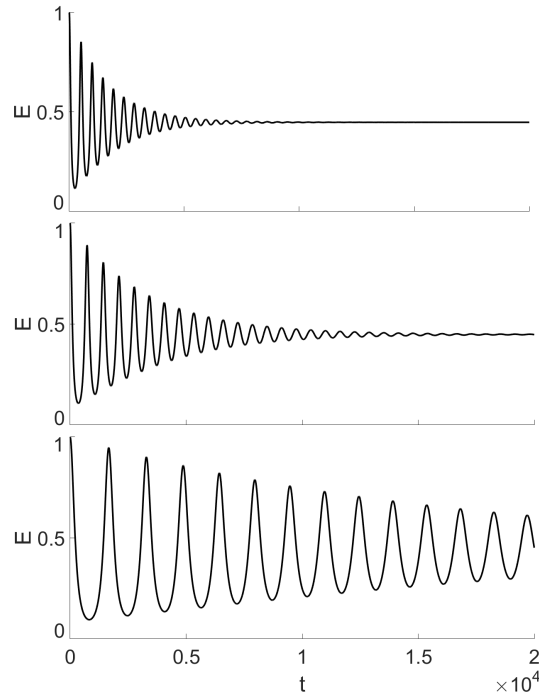


FIGURE 1.2: Relaxation oscillations of the laser electric field. From top to bottom $\gamma = 0.001$, $\gamma = 0.0005$ and $\gamma = 0.0001$ where $P = 1.2$.

$$\begin{aligned}\frac{dm}{d\tau} &= 2\hat{k}m \left(\frac{n}{1 + \Delta_{0c}^2} - 1 \right) \\ \frac{dn}{d\tau} &= \hat{\gamma}_{\parallel} \left[A - n \left(\frac{m}{1 + \Delta_{0c}^2} + 1 \right) \right]\end{aligned}\quad (1.77)$$

But $\Delta_{0c} = 2\Omega - \omega$ where $(2\Omega - \omega)^2 \sim 0$ (the rotating wave approximation). Moreover, by introducing the number of laser photons as the whole electric $m = E^2$ and by slightly changing the notation: $t = 2\hat{k}\tau$, $\gamma = \frac{\hat{\gamma}_{\parallel}}{2\hat{k}}$ and $n = N$, after the derivation we get:

$$\frac{dE}{dt} = \frac{1}{2}E(N - 1) \quad (1.78)$$

$$\frac{dN}{dt} = \gamma(P - N(1 + E^2)) \quad (1.79)$$

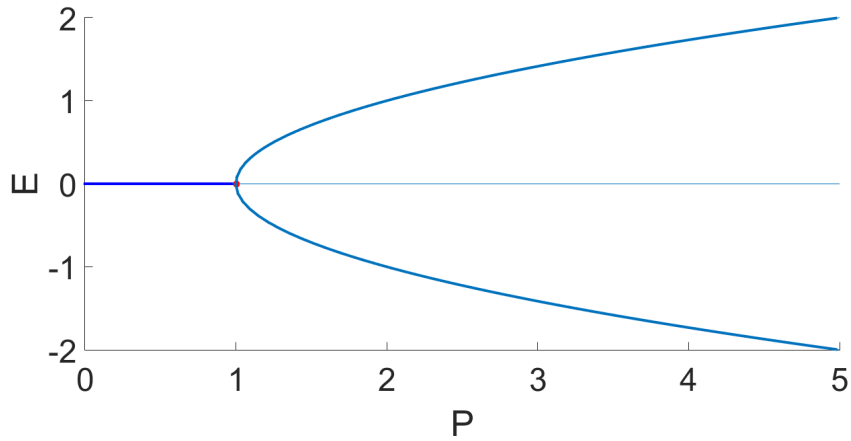


FIGURE 1.3: Pitchfork bifurcation for the laser electric field for $\gamma = 0.001$.

1.4.3 Linear stability

The steady state solutions of Eq. 1.78 and Eq. 1.79 satisfy the conditions

$$E(N - 1) = 0 \quad P - N(1 + E^2) = 0 \quad (1.80)$$

where the possible solutions are the zero electric field solution $(E, N) = (0, P)$ and the non-zero intensity solution $(E, N) = (\pm\sqrt{P-1}, 1)$. It is clear that lasing we have only for $P > 1$. In order to analyse the stability of the steady states, we calculate the Jacobian of the differential equation system Eq. 1.78 and Eq. 1.79 for the above fix points.

$$Jac = \begin{bmatrix} \frac{1}{2}(N-1) & \frac{1}{2}E \\ -2\gamma NE & -\gamma(1+E^2) \end{bmatrix} \quad (1.81)$$

A nontrivial solution is possible only if the growth rate λ satisfies the characteristic equation given by

$$\left(\lambda - \frac{1}{2}(N-1)\right)(\gamma(1+E^2) + \lambda) + \gamma NE^2 = 0 \quad (1.82)$$

In the case of the zero intensity steady state the above equation takes the form $(\frac{1}{2}(P-1) - \lambda)(\gamma + \lambda) = 0$ and admits the simple solutions $\lambda_1 = -\gamma$ and $\lambda_2 = \frac{1}{2}(P-1)$. If $Re(\lambda_j) < 0$ for $(j = 1, 2)$ then the fix point is stable. So,

we conclude that the zero intensity steady state is stable if $P < 1$ and unstable if $P > 1$. For both the non-zero intensity steady states Eq. 1.82 reduces to the following quadratic equation

$$\lambda^2 + \gamma P \lambda + \gamma(P - 1) = 0 \quad (1.83)$$

Solving this equation we obtain

$$\lambda_{1,2} = -\gamma \frac{P}{2} \pm i \sqrt{\gamma(P - 1) - \gamma^2 \frac{P^2}{4}} \quad (1.84)$$

The real part for both λ_1 and λ_2 is negative. Thus, the non-zero intensity fix points are always stable. These solutions are represented as a function of the pump parameter P in Fig. 1.1. The diagram is called a bifurcation diagram because it represents the amplitude of the possible solutions in terms of a control or bifurcation parameter. The bifurcation at $P = 1$ is a pitchfork bifurcation which exists only if $P \geq 1$. Below $P = 1$, only the zero intensity solution is possible. Beyond $P = 1$, two new solutions corresponding to the non-zero intensity state are available. The bifurcation is supercritical in our case (the new solutions overlap with the unstable basic solution) but it can be subcritical for other nonlinear problems (the new solution overlaps the stable basic solution).

In Eq. 1.84, expanding the two roots for small γ we obtain a more simple form:

$$\lambda_{1,2} = -\gamma \frac{P}{2} \pm i \sqrt{\gamma(P - 1)} \quad (1.85)$$

The above expression implies that the intensity oscillates with a frequency proportional to $\sqrt{\gamma}$ and slowly decays with a rate proportional to γ . The frequency here is defined by $\omega_R \equiv \sqrt{\gamma(P - 1)}$, is called the laser relaxation oscillation frequency and is a reference frequency for all lasers experiencing intensity oscillations. The quantity $\gamma(P/2)$ is called the damping rate of the laser relaxation oscillations.

In summary, the linearized theory reveals that the non-zero intensity steady

state is weakly stable for all lasers exhibiting a small γ and that slowly decaying oscillations of the laser intensity are possible (see Fig. 1.2).

1.4.4 Semiconductor lasers

So far we have infinitely sharp energy levels. In semiconductor lasers this is not realistic because there may be a continuum of levels such as in the energy bands in solid-state semiconductor media. For these situations, we can make a summation by an integral with a proper density of state factor (for more details see [Pierre et al., 2007]). Here we use just a more sophisticated description of the active medium [Erneux et al., 2010]. Their formulation is slightly different from the rate equations that were derived for gas or solid state lasers. In general, the proper rate equations, refer to complex amplitude E of the optical field ($E_{opt} = E(T)e^{i\omega_0 T}$) and the carrier number N_c . They have the form:

$$\frac{dE}{dT} = \frac{1}{2}(\Gamma G(N_c) - \frac{1}{T_p})E + i(\omega(N_c) - \omega_0)E \quad (1.86)$$

$$\frac{dN_c}{dT} = \frac{J}{e} - \frac{N_c}{T_s} - G(N_c)|E|^2 \quad (1.87)$$

The coefficient $\Gamma G(N_c)$ is defined as the power gain, T_p is the photon lifetime, and $\omega(N_c) - \omega_0$ is the detuning between the cavity resonance frequency and the optical frequency ω_0 of the field. The parameter Γ is called the confinement factor and takes into account the fact that only a part of the mode intensity contributes to the gain. J is the pump current, e is the elementary charge, T_s is the carrier lifetime, and the term $-G(N_c)|E|^2$ accounts for the stimulated loss of the carriers.

For low field intensity the optical gains vary almost linearly with N and is approximated as $\Gamma G(N_c) = \frac{1}{T_p} + \Gamma G_{N_c}(N_c - N_{th})$ where G_{N_c} and N_{th} are called the gain coefficient and the threshold carrier number, respectively. Similarly, the cavity resonance frequency is linearized around its value at threshold $\omega(N_c) = \omega_{th} + \omega_{N_c}(N_c - N_{th})$. But $\omega(N_c)$ is not independent from the gain coefficient G_{N_c} and the relation between the two coefficients is given in terms of the linewidth enhancement factor a . The so-called a parameter is

defined as,

$$a = \frac{2\omega_{N_c}}{\Gamma G_{N_c}} \quad (1.88)$$

and takes values from 1.3 to 7. Assuming $\omega_0 = \omega_{th}$ and introducing the new form of $\Gamma G(N_c)$ and $\omega(N_c)$ we obtain

$$\frac{dE}{dT} = \frac{1}{2}(\Gamma G(N_c))(1 + ia)nE \quad (1.89)$$

$$\frac{dn}{dT} = \frac{J - J_{th}}{e} - \frac{N}{T_s} - \left(\frac{1}{\Gamma T_p} + nG(N) \right) |E|^2 \quad (1.90)$$

where $n \equiv N_c - N_{th}$ and $J_{th} \equiv (N_{th}e)/T_s$ are called the inversion and the threshold current, respectively. By introducing new variables,

$$t \equiv T/T_p \quad \mathcal{E} \equiv \sqrt{\frac{T_s G_{N_c}}{2}} E \quad N \equiv \frac{\Gamma G_{N_c} T_p}{2} n \quad (1.91)$$

we obtain from Eq. 1.89 and Eq. 1.90,

$$\frac{d\mathcal{E}}{dt} = (1 + ia)N\mathcal{E} \quad (1.92)$$

$$T_r \frac{dN}{dt} = P - N - (1 + 2N)|\mathcal{E}|^2 \quad (1.93)$$

where the new parameters T_r and P are defined by:

$$T_r \equiv \frac{T_s}{T_p} \quad P \equiv \frac{T_s T_p G_{N_c} \Gamma}{2} \left(\frac{J - J_{th}}{e} \right) \quad (1.94)$$

The fixed parameter T_r takes large values between $10^2 - 10^3$ and represents the ratio of the carrier and photon lifetimes. P is the pump parameter above threshold and takes values between 10^{-2} and 1.

1.5 Coupled Lasers

1.5.1 Spacial Overlap

The simplest coupling scheme between the two lasers can be achieved through spacial overlap of the electric fields. By assuming that each laser field has a Gaussian intensity profile and a constant phase front, the transverse field can be written as

$$E'_k(x, y, t) = \frac{E_k(t)}{2\pi\sigma^2} \exp\left[-\frac{x^2 + y^2}{2\sigma^2}\right] \quad (1.95)$$

where $\sigma = w/\sqrt{2}$ and $k = 1, 2$. The overlap integral of the two beams separated by a distance D is given by

$$\int_{-\infty}^{\infty} \int_{-\infty}^{\infty} dx dy E'_1(x + D, y, t) E'_2{}^*(x, y, t) = \frac{E_1(t)E_2^*(t)}{2\pi\sigma^2} \exp\left[-\frac{D^2}{4\sigma^2}\right] \quad (1.96)$$

The coupling coefficient k is obtained from the overlap integral with the normalisation $|\kappa| = 1$ when $D = 0$. Then,

$$\kappa = \pm \exp\left[-\frac{D^2}{4\sigma^2}\right] \quad (1.97)$$

In the case of two lasers, for the total field, we usually try solutions in the form

$$E'(x, y, t) = [E_1(t)B_1(x, y) + E_2(t)B_2(x, y)] e^{-i\omega t} \quad (1.98)$$

where ω is chosen as the reference frequency. Then, with a Gaussian intensity profile for each laser, we obtain

$$\kappa = \pm \exp\left[-\frac{D^2}{4\sigma^2}\right] e^{-i\omega\tau_{in}} \quad (1.99)$$

where τ_{in} is approaching as the roundtrip time in the laser cavity. A strictly imaginary coupling coefficient corresponds to conservative coupling, while a strictly real coefficient corresponds to dissipative coupling.

An example of this case of coupling has been used for the simplest model [Fabiny et al., 1993] of two solid-states coupled lasers consists of equations for the complex fields E and the gains G of the lasers,

$$\begin{aligned}\frac{dE_1}{dt} &= (G_1 - 1)E_1 + \kappa E_2 + i\omega_1 E_1 \\ \frac{dG_1}{dt} &= \gamma(p - G_1 - G_1|E_1|^2) \\ \frac{dE_2}{dt} &= (G_2 - 1)E_2 + \kappa E_1 + i\omega_2 E_2 \\ \frac{dG_2}{dt} &= \gamma(p - G_2 - G_2|E_2|^2)\end{aligned}\tag{1.100}$$

where the dimensionless time t and the population inversion decay time γ^{-1} are measured in units of the field decay time rescaling by the cavity loss coefficients. p is the pump coefficient. κ is the normalized coupling rate between neighboring lasers. The normalized angular frequency $\omega_{1,2}$ measures the detuning of laser 1, 2 from a common reference.

Here, κ has been chosen real with positive sign to correspond to the experimentally observed results. The same model with this coupling scheme has been demonstrated in many other papers [Kuske et al., 1997; Rogister et al., 2007; Thornburg et al., 1997].

1.5.2 Optical feedback

A very important work in the research on laser dynamics is the paper by Lang and Kobayashi [Lang et al., 1980], who reported on some aspects of the dynamics of a semiconductor laser in the presence of the optical feedback. They showed that a diode laser subject to external optical feedback can show multistability as well as hysteresis phenomena, analogous to the nonlinear Fabry-Perot resonator. These phenomena are caused by the fact that the distant mirror creates an external cavity which has its own resonance frequencies.

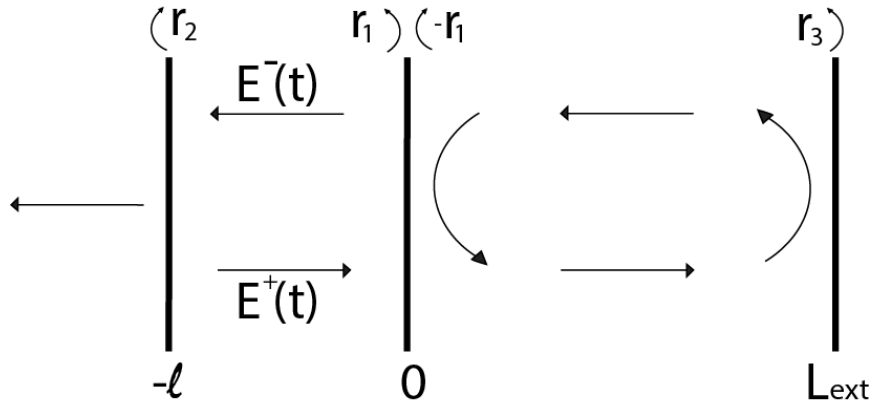


FIGURE 1.4: The Fabry-Perot cavity model with an external cavity to use in deriving the rate equations in the case of optical feedback.

Here we will present the proper extensions needed to deal with external optical feedback. As long as the polarization of the field is not rotated the carrier equation needs no modification, and only the field equations must be adapted to the optical perturbations. It is convenient to distinguish inside the diode cavity between waves travelling in the positive, $E^+(t)$, and negative, $E^-(t)$ (see Fig. 1.4). The difference equation describing the field amplitude after one internal roundtrip time τ_{in} .

The amplitude $E^-(t)$ of the wave travelling in the negative z -direction at $z = 0$ is the result of both the reflection of $E^+(t)$ and the amplitude of the wave inside the external cavity,

$$\begin{aligned}
 E^-(t) &= rE^+(t) \\
 &+ (1 - r^2)r_3E^+(t - \tau)e^{-i\omega\tau} \\
 &+ (1 - r^2)r_3(-rr_3)E^+(t - 2\tau)e^{-2i\omega\tau} \\
 &+ (1 - r^2)r_3(-rr_3)^2E^+(t - 3\tau)e^{-3i\omega\tau} \\
 &+ \dots
 \end{aligned} \tag{1.101}$$

where r_3 is the external mirror reflectivity and r the reflectivity of the laser cavity. The external signal $E_{ext}^-(t)$ can thus be written as:

$$E_{ext}^-(t) = \frac{r^2 - 1}{r^2} \sum_{n=1}^{n=\infty} (-rr_3)^n e^{-in\omega\tau} E^+(t - n\tau) \tag{1.102}$$

When the feedback is weak can be approximated by taking into account just one external round-trip. Moreover, if we have just the electric field before the entry in the laser cavity then can be shown [Tartwijk et al., 1995] that the feed is equal to $\frac{1}{\tau_{in}}(\frac{1}{r} - r)$ and the resulting equation can be written as:

$$\frac{dE}{dt} = (1 + ia)EG + ke^{-i\omega\tau}E(t - \tau) \quad (1.103)$$

where the first term is the well know semiconductor laser without feedback and k is the feedback-rate and is defined as:

$$k = \frac{1 - r^2}{\tau_{in}} \frac{r_3}{r} \quad (1.104)$$

1.5.3 Eigenmodes of a single waveguide

Using Eq. 1.1, 1.2, 1.3 we obtain the fundamental electromagnetic wave equation that describes the propagation of optical fields inside the medium:

$$\nabla^2 \mathcal{E} - \frac{\sigma}{\epsilon_0 c_0^2} \frac{\partial \mathcal{E}}{\partial t} - \frac{1}{c_0^2} \frac{\partial^2 \mathcal{E}}{\partial t^2} = \frac{1}{\epsilon_0 c_0^2} \frac{\partial^2 \mathcal{P}}{\partial t^2} + \nabla(\nabla \cdot \mathcal{E}) \quad (1.105)$$

The term $\nabla \cdot \mathcal{E}$ is often neglected, which can be justified by assuming the absence of free charge [Agrawal et al., 1986]. Moreover, we often drop the term which is related with the current density ($-\frac{\sigma}{\epsilon_0 c_0^2} \frac{\partial \mathcal{E}}{\partial t}$), using it only to simulate losses in a Fabry-Perot resonator [Pierre et al., 2007].

Now, of particular interest are the optical field with harmonic time variation. Therefore using the paraxial approximation Eq. 1.7, the wave equation Eq. 1.105 reduces to:

$$\nabla^2 E(\mathbf{r}) + \frac{\omega^2}{c_0^2} E(\mathbf{r}) = -\frac{\omega^2}{c_0^2 \epsilon_0} \mathcal{P}(\mathbf{r}) \quad (1.106)$$

Under steady-state conditions the response of the medium to the electric field is governed by the susceptibility χ :

$$\mathcal{P} = \epsilon_0 \chi E \quad (1.107)$$

In general χ is a second-rank tensor, but here we restrict ourselves to isotropic media for which χ is a scalar and position independent. We rewrite the time-independent wave equation Eq. 1.106 using Eq. 1.107) yielding,

$$c_0^2 \nabla^2 E + n^2 \omega^2 E = 0 \quad (1.108)$$

where $n = \sqrt{\chi + 1}$.

Let us introduce the index of the guide,

$$n(x, y) = \bar{n} [1 + \delta n(x, y)] \quad (1.109)$$

where we note by x and y the transverse coordinates with respect to the direction of propagation z and suppose that this index it is independent of z variable. Here, \bar{n} is the index of the crystal and $\delta n(x, y)$ is the thermally induced index. For instance,

$$\delta n(x, y) = a e^{-r^2/h_n^2} \quad (1.110)$$

where $r = \sqrt{x^2 + y^2}$ is the transverse radial coordinate. This formula describes a Gaussian index profile of characteristic width h_n and amplitude a and the whole index can be approximated, in the transverse region where $r \ll h_n$, by,

$$n(x, y) = \bar{n}(1 + a) \left(1 - \frac{r^2}{2\mathcal{H}^2} \right) \quad (1.111)$$

where $\mathcal{H} = h_n \sqrt{(1 + a)/2a}$.

If the index is independent of the variable z , solving Eq. 1.108 with the method of separation of variables (also known as the Fourier method) which

satisfy boundary conditions where $z = 0$ and $z = L \rightarrow E = 0$ (where L is the length of the crystal) one gets the field as,

$$E(x, y, z, t) = \bar{E}(x, y) \sin(\beta z) e^{i\omega t} \quad (1.112)$$

where the transverse envelop $\bar{E}(x, y)$, characterizes the transverse profile of the field. Inserting Eq. 1.112 and Eq. 1.111 into Maxwell Eq. 1.108 leads to

$$\nabla_{\perp}^2 \bar{E}(x, y) = \left[\beta^2 - \left(\bar{n}(1+a) \left(1 - \frac{r^2}{2\mathcal{H}^2} \right) \right)^2 \frac{\omega^2}{c_0^2} \right] \bar{E}(x, y) \quad (1.113)$$

This mathematical expression leads to a Schrödinger-like equation for a harmonic oscillator [Yariv, 1989]. Retaining the solution with cylindrical symmetry, we get in the paraxial approximation ($r \ll \mathcal{H}$) the eigenmode:

$$\bar{E}(x, y) = \exp \left[-\frac{x^2 + y^2}{w^2} \right] \quad (1.114)$$

where:

$$w = \sqrt{\frac{2\mathcal{H}c_0}{\omega \bar{n}(1+a)}} \quad \beta = \frac{\omega \bar{n}(1+a)}{c_0} \left(1 - \frac{2c_0}{\mathcal{H}\omega \bar{n}(1+a)} \right) \quad (1.115)$$

The dispersion relation reads

$$\omega = \frac{c_0}{n} \left(\beta(1-a) + \frac{\sqrt{2a}}{h_n} \right) \quad (1.116)$$

Boundary conditions at crystal ends lead to the quantization of wave vectors ($\beta_n = n\pi c_0/L$). The related frequencies, given implicitly by Eq. 1.116, are the cavity eigenfrequencies and depend on β_n and on index parameters a or h_n . In other words, for a given wave-vector β (fixed by boundary conditions), one can play on the eigenfrequencies by changing the index parameters a or h_n . They act on the effective length of the cavity.

1.5.4 Evanescent waves coupling

We consider the case where the crystal is active and irradiated by two parallel pump beams. Two lasers are generated interacting by evanescent waves coupling. The refractive index profile is a generalization of Eq. 1.109,

$$n(x, y) = \bar{n} [1 + \delta n_1(x, y) + \delta n_2(x, y)] \quad (1.117)$$

where $\delta n_j(x, y)$ are the waveguide index profile ($j = 1, 2$). As in Eq. 1.110,

$$\delta n_j(x, y) = a_j \exp\left(\frac{-(x - x_j)^2 - y^2}{h_{nj}^2}\right) \quad (1.118)$$

where h_{nj} and a_j are the width and amplitude of the j th index profile. With the term $(x - x_j)$ we indicate the position of each beam in the x axes. We take as reference solution the Eq. 1.112 and Eq. 1.112 with their respectively eigenfrequencies. We note by $E(x, y, z, t)$ the total laser field.

From Eq. 1.105, multiplying by the speed of light in the active medium of the laser and after the previous neglecting terms in subsection 5.3, one has,

$$c^2 \nabla^2 E + n^2(x, y) \frac{\partial^2 E}{\partial t^2} = \mu_0 c^2 \frac{\partial^2 P}{\partial t^2} \quad (1.119)$$

where $P(x, y, z, t)$ is now the polarization of the laser active medium which acts as a source term and is not proportional to the electric field. The coupling between the two lasers is controlled by the distance ($D = x_1 - x_2$) between guides. For weak coupled lasers, we try the solution,

$$\begin{aligned} E(x, y, z, t) &= \mathcal{E}(x, y, z, t) e^{-i\omega_1 t} \\ &= [c_1(t) B_1(x, y, z) + c_2(t) B_2(x, y, z)] e^{-i\omega_1 t} \end{aligned} \quad (1.120)$$

where c_j are complex amplitudes. ω_1 is chosen arbitrary as the reference frequency. Each guide with index n_j has an eigenmode defined by Eq. 1.108

for each B_j . Inserting Eq.1.120 in Eq.1.119 we obtain,

$$\begin{aligned} & c^2 \left[c_1(t) \nabla^2 B_1 + c_2(t) \nabla^2 B_2 \right] \\ &= n^2(x, y) \left\{ \left[\ddot{c}_1(t) - 2i\omega_1 \dot{c}_1(t) - \omega_1^2 c_1 \right] B_1 + \left[\ddot{c}_2(t) - 2i\omega_1 \dot{c}_2(t) - \omega_1^2 c_2 \right] B_1 \right\} \\ & - \mu_0 \omega_1^2 c_2 \mathcal{P} \end{aligned} \quad (1.121)$$

where \mathcal{P} is the slowly varying envelope of the polarization:

$$P(x, y, z, t) = \mathcal{P}(x, y, z) e^{-i\omega_1 t} \quad (1.122)$$

In the weak-coupling limit, the complex amplitudes $c_1(t)$ and $c_2(t)$ vary slowly in time compared to the fast oscillations at frequency ω_1 and this leads to the slowly-varying approximation $|\ddot{c}_1| \ll \omega_1 |\dot{c}_1|$. Using Eq. 1.108, we obtain:

$$\begin{aligned} & n^2 (\dot{c}_1 B_1 + \dot{c}_2 B_2) \\ &= i \frac{c_1 \omega_1}{2} \left[n^2 - n_1^2 \right] B_1 + i \frac{c_2}{2\omega_1} \left[n^2 \omega_1^2 - n_1^2 \omega_2^2 \right] B_2 + i \frac{\omega_1}{2\epsilon_0} \mathcal{P} \end{aligned} \quad (1.123)$$

In the semiclassical approach, as we have seen in subsection 1.3, the material variables obey the Bloch equations for a two-level atomic medium

$$\begin{aligned} \dot{\mathcal{P}} &= -\gamma_{\perp} \mathcal{P} - i(\omega_a - \omega_1) \mathcal{P} - \frac{i\mu}{2\hbar} D \mathcal{E} \\ \dot{D} &= -\gamma_{\parallel} (D - \hat{D}) - \frac{i\mu}{\hbar} (\mathcal{P} \mathcal{E}^* - \mathcal{E} \mathcal{P}^*) \end{aligned} \quad (1.124)$$

where μ is the dipole moment matrix (the same variable with the symbol d in subsection 1.3), \hat{D} is the pump parameter, D is the population inversion and ω_a is the resonance frequency of the laser active medium. The polarization has been adiabatically eliminated and the detuning effect has been

neglected in the limit $(\omega_a - \omega_1) \ll \gamma_\perp$. We thus have:

$$\dot{D} = -\gamma_\parallel \left(D - \hat{D} + \frac{\mu^2}{\hbar^2 \gamma_\perp \gamma_\parallel} D |\mathcal{E}|^2 \right) \quad (1.125)$$

With the proper rescaling:

$$(\bar{\mathcal{E}}, \bar{c}_j) = \sqrt{\frac{\mu^2}{\hbar^2 \gamma_\parallel \gamma_\perp}} (\mathcal{E}, c_j) \quad (d, \hat{d}) = \frac{\omega_1}{2\epsilon_0} \frac{\mu^2}{\hbar^2 \gamma_\perp k n^2} (D, \hat{D}) \quad (1.126)$$

where k is relative to the field relaxation, one has:

$$\begin{aligned} (\dot{c}_1 B_1 + \dot{c}_2 B_2) &= i \frac{c_1 \omega_1}{2} \left[1 - \frac{n_1^2}{n^2} \right] B_1 + i \frac{c_2}{2\omega_1} \left[\omega_1^2 - \frac{n_2^2 \omega_2^2}{n^2} \right] B_2 + kd\bar{\mathcal{E}} - k\bar{\mathcal{E}} \\ \dot{d} &= \gamma_\parallel \left(\hat{d} - d - d|\bar{\mathcal{E}}|^2 \right) \end{aligned} \quad (1.127)$$

Detuning is noted $\Delta\omega = \omega_2 - \omega_1$. Assuming $\Delta\omega \ll \omega_2, \omega_1$ we have $\omega_2 \sim \omega_1$ and $(\omega_2/\omega_1)^2 \sim 2\Delta\omega/\omega_1 + 1$. With this approximation we get,

$$\begin{aligned} \dot{c}_1 B_1 + \dot{c}_2 B_2 &= i \frac{c_1 \omega_1}{2} \left[1 - \frac{n_1^2}{n^2} \right] B_1 + i \frac{c_2 \omega_1}{2k} \left[1 - \frac{n_2^2}{n^2} \right] B_2 \\ &\quad - ic_2 \delta \frac{n_2^2}{n^2} B_2 + d\bar{\mathcal{E}} - \bar{\mathcal{E}} \\ \dot{d} &= \gamma \left(\hat{d} - d - d|\bar{\mathcal{E}}|^2 \right) \end{aligned} \quad (1.128)$$

where time is now in k units $\delta = \Delta\omega/k$ and $\gamma = \gamma_\parallel/k$. The detuning is related to the effective lengths of each lasers. One can make index amplitudes $a_1 \neq a_2$ or widths $h_{n1} \neq h_{n2}$ by slightly different pump profiles.

In order to describe the temporal evolution of the amplitudes c_1 and c_2 , one should perform the projections of Eq. 1.128 on the nonorthonormal eigenmodes B_1 and B_2 . This procedure has been done by [Zehnlé, 2000] and

here we present the results under four simplifications.

(I) For class A lasers the inversion can be adiabatically eliminated and near threshold where $\mathcal{E} \rightarrow 0$ we can write:

$$d(x, y, z, t) = \widehat{d}(x, y) [1 - c_i c_j B_i B_j] \quad (1.129)$$

We implied summation over the whole set of indexed terms (Einstein summation convention). For class B lasers, this expression can be generalize in this form,

$$d(x, y, z, t) = \widehat{d}(x, y) [1 - d_{ij} B_i B_j] \quad (1.130)$$

where d_{ij} are real moments of inversion $d(x, y, z, t)$ depending only on time. The inversion of Eq.1.128 is then replaced by ODEs for moments d_{ij} ,

$$\begin{aligned} \dot{d}_1 &= -\gamma(d_1 - |c_1|^2) \\ \dot{d}_2 &= -\gamma(d_2 - |c_2|^2) \end{aligned} \quad (1.131)$$

(II) Pump beams in each channel are assumed to be Gaussian and equal.

$$\widehat{d}(x, y) = \widehat{d} \left(e^{-r_1^2/h_p^2} + e^{-r_2^2/h_p^2} \right) \quad (1.132)$$

(III) The only asymmetry between the lasers is the detuning term, which is sensitive to very slight waveguide differences ($\omega_1 - \omega_2 \sim c\beta(a_2 - a_1)$).

(IV) In the weak coupling case, D is the largest. Due to thermal diffusion h_n is much larger than h_p and also than w ($D \geq h_n > h_p \sim w$).

Under those approximations one finally gets the final form:

$$\begin{aligned} \dot{c}_1 &= \left[P - 1 - \frac{3}{5}Pd_1 \right] c_1 + gc_2 \\ \dot{c}_2 &= \left[P - 1 - \frac{3}{5}Pd_2 \right] c_2 - i\delta c_2 + gc_1 \end{aligned} \quad (1.133)$$

where P is the usual gain term. With g we denote the coupling term which can be written in terms of its real and imaginary parts in the form $g = g_r + ig_{im}$ where:

$$g_r = \frac{2\hat{d}}{2 + w^2/h_p^2} \left[2 \exp\left(-D^2 \frac{h_p^2 + w^2}{w^2(h_p^2 + 2W^2)}\right) - \exp\left(-D^2/2w^2\right) \right] \quad (1.134)$$

$$g_{im} = \left(\frac{a_1\omega_1}{k}\right) \left[\exp\left(-D^2/2w^2\right) \right] \left[1 - \exp\left(-D^2/h_n^2\right) \right] \quad (1.135)$$

Parameter g_{im} , which is related to the refractive index, remains always positive. The real part g_r takes positive or negative values and vanishes for $D \sim 2w$ if $h_p \sim w$.

Chapter 2

Synchronization and Chimera states

2.1 Introduction

The term synchronous comes from the Greek words "*χρονος*", meaning time and "*συν*", meaning in common, occurring at the same time. Synchronization refers to a variety of phenomena in almost all fields of natural sciences that is observed when a large part of a system of oscillators spontaneously locks to a common frequency, forgetting the differences in the natural frequencies of the individual oscillators. Synchronization manifests itself in different scenarios, from complete synchronization, where all oscillators have the same frequency, to partial synchronization where the system split into synchronized and unsynchronized domains.

In this chapter we start by describing a self-sustained oscillator which is interacting with a periodic external force. This interaction may lead to a complete locking of the oscillation phase to that of the force. We consider the case of small forcing to use a perturbation technique based on the phase dynamics approximation. This approach leads to a simple phase equation that can be treated analytically. Then we develop a phase dynamics approach for two coupled oscillators that is valid if the coupling again is small. The problem here reduces to coupled equations for the phases difference between the two sites.

For a discrete medium we assume that each element is a self-sustained oscillator. We begin by considering a one-dimensional chain of oscillators

assuming that nearest neighbors interact. This approach is a natural generalization of the system of two coupled systems. Starting with a description of the phase dynamics in lattices where different sites can oscillate with different periods and phases we extract a phase equation which after a numerical investigation provides clusters formations.

The synchronization in a discrete lattice can be generalized to systems where the oscillators can interact not only with neighbours but also with many other oscillators. More precisely, the interaction can be global or non-local. Here we consider a model of N mutually coupled oscillators having different or similar natural frequencies in the presence of a phase-lag term. The nature of the collective dynamics depends on the structure, the system size, the coupling and the initial conditions. We emphasize on phenomena where the system splits into coexisting regions of coherent and incoherent oscillations, the so called chimeras states.

For a proper description of those states, we introduce the Kuramoto model which describes a large population of all-to-all coupled phase oscillators. If the coupling strength exceeds a certain threshold, the system exhibits a phase transition and all oscillators synchronize. Finally, beyond the splitting of the system into a coherent and incoherent domain, we present additional features like breathing chimera states, an irregular motion of the position of the coherent and incoherent regions and also multichimera states with many coherent and incoherent domains in the same system.

2.2 The synchronization from individual oscillators to a discrete lattice

In this section we describe synchronization of periodic oscillators in the presence of a periodic external force. If this force is small, a complete locking of the oscillation phase to that of the force can be achieved where the oscillation frequency matches the frequency of the forcing. Then we analyse the effect of synchronization for the interaction of two oscillating systems. The case of periodic forcing can be considered here as a special case of two interacting oscillators when the coupling is unidirectional. After this, we illustrate an example in optics with two coupled lasers and finally we move to many

interacting oscillators in a discrete lattice where the system goes to full synchronization through the formation of many clusters.

2.2.1 Synchronization by external action

Consider a general M -dimensional ($M \geq 2$) system of ordinary differential equations

$$\frac{d\mathbf{x}}{dt} = f(\mathbf{x}) \quad \mathbf{x} = (x_1, \dots, x_M) \quad (2.1)$$

and suppose that this system has a stable periodic (with period T_0) solution $x_0(t) = x_0(t + T_0)$. In the phase space this solution is an isolated closed attractive trajectory, the so called limit cycle (see Fig. 2.1). The point in the phase space moving along the cycle represents the self-sustained oscillations. By self-sustained oscillatory system [Arkady et al., 2001] we mean an active system which contains an internal source of energy that is transformed into oscillatory movement where the form of oscillations is stable to small perturbations and the system itself is operating out of, and often far from, the equilibrium with the environment with which it exchanges energy (dissipative system). Moreover, this form of oscillation is determined by the parameters of the system and does not depend on the transient to steady oscillation. Mathematically, it is described by an autonomous (without explicit time dependence) dynamical system.

For this system we introduce the phase ϕ as a coordinate along the limit cycle and we demand that the phase grows uniformly in time so that it obeys the equation $d\phi/dt = \omega_0$ where $\omega_0 = 2\pi/T_0$ is the frequency of self-sustained oscillations, the so called natural frequency. This equation has a very important property. Consider two close trajectories in the phase space, i.e., the unperturbed and the perturbed ones. After a time interval we will see that, in the radial direction of the limit cycle they converge with time, while in the direction of the phase they neither converge nor diverge. In terms of nonlinear dynamics, the convergence/divergence properties of nearby trajectories are characterized by the Lyapunov exponents. Convergence of trajectories along some direction in the phase space corresponds to a negative Lyapunov exponent. Similarly, the divergence of trajectories is characterized

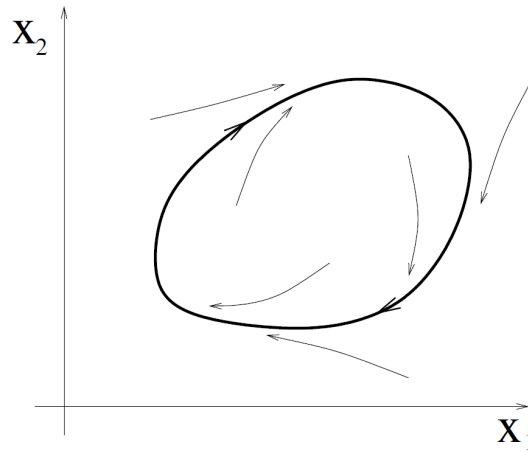


FIGURE 2.1: A limit cycle for a two-dimensional dynamical system. The form of it can be any closed curve. The neighboring trajectories are attracted to the cycle. (redrawn from Figure 7.1 of [Arkady et al., 2001])

by a positive exponent. Finally, the neutral direction (no divergence and no convergence) corresponds to a zero Lyapunov exponent and this is the most important conclusion: the phase of a self-sustained oscillator can be considered as a variable that corresponds to the zero Lyapunov exponent.

We now consider the effect of a small external periodic force on the self-sustained oscillations. We describe the forced system by the equations,

$$\frac{d\mathbf{x}}{dt} = \mathbf{f}(\mathbf{x}) + \varepsilon \mathbf{p}(\mathbf{x}, t) \quad (2.2)$$

where the force $\varepsilon \mathbf{p}(\mathbf{x}, t) = \varepsilon \mathbf{p}(\mathbf{x}, t + T)$ has a period T , which is in general different from T_0 . The force is proportional to a small parameter ε , and below we consider only first-order effects in ε . This external force is small to drive the radial direction of the limit cycle out of equilibrium but can easily drive the phase point along the cycle.

Returning to the phase, as this variable is a smooth function of the coordinates \mathbf{x} , we can represent its time derivative as,

$$\frac{d\phi(\mathbf{x})}{dt} = \sum_k \frac{\partial \phi}{\partial x_k} \frac{dx_k}{dt} \quad (2.3)$$

which gives in association with Eq. 2.2, the relation,

$$\sum_k \frac{\partial \phi}{\partial x_k} f_k(\mathbf{x}) = \omega_0 \quad (2.4)$$

and from Eq. 2.2 we get:

$$\frac{d\phi(\mathbf{x})}{dt} = \sum_k \frac{\partial \phi}{\partial x_k} (f_k(\mathbf{x}) + \varepsilon p_k(\mathbf{x}, t)) = \omega_0 + \varepsilon \sum_k \frac{\partial \phi}{\partial x_k} p_k(\mathbf{x}, t) \quad (2.5)$$

The second term on the right-hand side is small (proportional to ε), and the deviations of \mathbf{x} from the limit cycle \mathbf{x}_0 are small too. Thus, consider only first order in ε we can neglect these deviations obeying the relation,

$$\frac{d\phi(\mathbf{x})}{dt} = \omega_0 + \varepsilon Q(\phi, t) \quad (2.6)$$

where:

$$Q(\phi, t) = \sum_k \frac{\partial \phi(\mathbf{x}_0)}{\partial x_k} p_k(\mathbf{x}_0, t) \quad (2.7)$$

The function Q is 2π -periodic in ϕ and T -periodic in t therefore we can represent it as a double Fourier series,

$$Q(\phi, t) = \sum_{l,k} a_{l,k} e^{ik\phi + il\omega t} \quad (2.8)$$

where $\omega = 2\pi/T$ is the frequency of the external force. Moreover, from Eq. 2.6, if we neglect the second term on the right-hand side we get the solution,

$$\phi = \omega_0 t + \phi_0 \quad (2.9)$$

where ϕ_0 is a constant which can be determined from the initial condition. This approximation gives, together with Eq. 2.8, the relation:

$$Q(\phi, t) = \sum_{l,k} a_{l,k} e^{ik\phi_0} e^{i(k\omega_0 + l\omega)t} \quad (2.10)$$

Substitution of Eq. 2.10 in Eq. 2.6 and by solving the differential equation we get to the denominator terms in the form $(k\omega_0 + l\omega)$. This shows that only the resonant terms ($k\omega_0 \sim l\omega$) can lead to large variation and are mostly important for the dynamics. In that case, only the terms with $k = -l$ are resonant. Summation of these terms gives:

$$Q(\phi, t) = \sum_{l,k} a_{l,k} e^{ik\phi + il\omega t} = \sum_k a_{-k,k} e^{ik(\phi - \omega t)} = q(\phi - \omega t) \quad (2.11)$$

Substituting this relation in Eq. 2.6 we get:

$$\frac{d\phi}{dt} = \omega_0 + \varepsilon q(\phi - \omega t) \quad (2.12)$$

Defining new variables like $\psi = \phi - \omega t$ and $v = \omega - \omega_0$ we finally obtain:

$$\frac{d\psi}{dt} = -v + \varepsilon q(\psi) \quad (2.13)$$

The simplest periodic function of q is the sinusoidal function which gives the simplest form of the averaged phase equation:

$$\frac{d\psi}{dt} = -v + \varepsilon \sin(\psi) \quad (2.14)$$

and this is often called the Adler equation.

The function $q(\psi)$ is a periodic function of ψ and thus has a maximum q_{max} and a minimum q_{min} . If the frequency detuning v lies in the interval $\varepsilon q_{min} < v < \varepsilon q_{max}$, then there is at least one stable fixed point of Eq. 2.13. For that we first set $-v + \varepsilon q(\psi^*) = 0$ and solve for the fixed point ψ^* . To determine the stability we plot the $\dot{\psi}$ in function of ψ and then sketch the

vector field. The flow is to the right where $-v + \varepsilon q(\psi) > 0$ and to the left where $-v + \varepsilon q(\psi) < 0$. Therefore, if $\varepsilon(q - q_{min}) < \dot{\psi} < \varepsilon(q - q_{max})$ is fulfilled, the system evolves to one of the stable fixed points and stays there, so that $\psi = \psi_c$ is a constant. This fact for the phase ϕ means a constant rotation with the frequency of the external force $\phi = \omega t + \psi_c$. This is the regime of synchronization (see Fig. 2.2 (a)) and exists inside the domain on the parameter plane (v, ε) . One often says that the phase is locked by the phase of the external force and this regime is called phase locking.

If v is outside of the range $\varepsilon q_{min} < v < \varepsilon q_{max}$ then the oscillation frequency differs from the frequency of the external force. We can write then the solution of Eq. 2.13 for one period T_ψ in the form:

$$T_\psi = \left| \int_0^{2\pi} \frac{dt}{d\psi} d\psi \right| = \left| \int_0^{2\pi} \frac{d\psi}{\varepsilon q_\psi - v} \right| \quad (2.15)$$

where the phase now has the relation $\phi = \omega t + \psi(t)$. The frequency Ω_ψ of this period, the so called observed frequency or the beat frequency, can be defined by the equation,

$$\Omega_\psi = 2\pi \left(\left| \int_0^{2\pi} \frac{d\psi}{\varepsilon q_\psi - v} \right| \right)^{-1} \quad (2.16)$$

where the observed frequency Ω of the original phase ϕ is $\Omega = \omega + \Omega_\psi$.

The beat frequency Ω_ψ depends on the detuning v and in the limit of the synchronization region we can estimate this dependence analytically. The synchronization transition happens when $-v + \varepsilon q(\psi) = 0$ and $q(\psi) = q_{max,min}$. There, the stable and the unstable fixed points collide and disappear through a saddle-node bifurcation. The expression $|\varepsilon q(\psi) - v|$ is very small in the vicinity of the point ψ_{max} , so we can expand the function $q(\psi)$ in a Taylor series at ψ_{max} and setting the integration limits to infinity. This procedure gives $\varepsilon q_\psi - v \sim \varepsilon q(\psi_{max}) - v + \varepsilon q'(\psi_{max})(\psi - \psi_{max}) + \varepsilon/2 q''(\psi_{max})(\psi - \psi_{max})^2 \sim v_{max} - v + \varepsilon/2 q''(\psi_{max})\psi^2$ where $v_{max} = \varepsilon q_{max}$, $q'(\psi_{max}) = 0$ (the derivation where the function gets the max value) and $(\psi - \psi_{max})^2 \sim \psi^2$. Substitution this expansion in Eq. 2.16 gives:

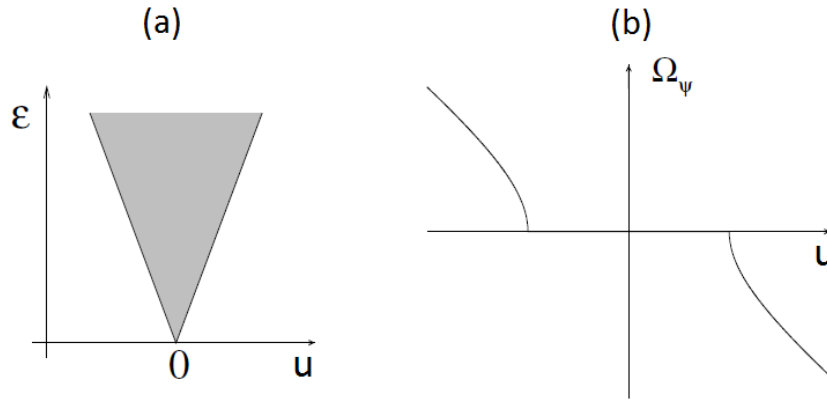


FIGURE 2.2: (a) The synchronization region on the plane of parameters v, ε , where the borders of the synchronization region are straight lines. (b) The observed frequency dependence on frequency detuning. (redrawn from Figure 7.4 of [Arkady et al., 2001])

$$\begin{aligned} \Omega_\psi &\sim 2\pi \left| \int_{-\infty}^{\infty} \frac{d\psi}{\frac{\varepsilon}{2} q''_{\psi_{max}} \psi^2 - (v - v_{max})} \right|^{-1} \\ &= \sqrt{\varepsilon |q''_{\psi_{max}}| \cdot (v - v_{max})} \sim \sqrt{v - v_{max}} \end{aligned} \quad (2.17)$$

This dependence has been shown in Fig. 2.2 (b).

Until now, we have used only weak external force. For a moderate amplitudes of the force two main features are slightly different with the previous analysis. The boundaries of the synchronization region are no longer straight lines but, generally, curved lines and the most important, the non resonant terms can not be neglected any more. This causes the difference between the phase of the oscillations and that of the external force to not be constant but a periodic function of time. Finally, for large forcing amplitudes we have even transition to synchronization through other bifurcations and for more complex regimes, transition to chaos, may be observed.

2.2.2 Synchronization of two interacting periodic oscillators

In this subsection we consider the effects of synchronization due to the interaction of two oscillating systems. The case of periodic forcing can be considered as a special case of two interacting oscillators when the coupling is

unidirectional. The approach here is essentially the same as in the case of the previous subsection. Our basic model is a system of two interacting oscillators:

$$\begin{aligned}\frac{d\mathbf{x}^{(1)}}{dt} &= \mathbf{f}^{(1)}(\mathbf{x}^{(1)}) + \varepsilon \mathbf{p}^{(1)}(\mathbf{x}^{(1)}, \mathbf{x}^{(2)}) \\ \frac{d\mathbf{x}^{(2)}}{dt} &= \mathbf{f}^{(2)}(\mathbf{x}^{(2)}) + \varepsilon \mathbf{p}^{(2)}(\mathbf{x}^{(2)}, \mathbf{x}^{(1)})\end{aligned}\quad (2.18)$$

The two interacting systems can be of different nature and have different dimensions. Also, the coupling can be asymmetric. Moreover, the autonomous dynamics (given by the functions $\mathbf{f}^{(1)}, \mathbf{f}^{(2)}$) can be separated from the interaction (described by generally different terms $\mathbf{p}^{(1)}, \mathbf{p}^{(2)}$), proportional to the coupling constant ε and this is the proper description for two independent oscillators that can operate separately, but which may also interact. We thus exclude a situation when two oscillating modes are observed in a complex system that cannot be decomposed into two parts.

When the coupling constant is zero, each system has a stable limit cycle with frequencies $\omega_{1,2}$. Thus, we can introduce two phases $d\phi_1/dt = \omega_1$ and $d\phi_2/dt = \omega_2$. After that, we can write the equations for the phases in the coupled system, in the first approximation, as:

$$\begin{aligned}\frac{d\phi_1(\mathbf{x}^{(1)})}{dt} &= \omega_1 + \varepsilon \sum_k \frac{\partial \phi_1}{\partial x_k^{(1)}} p_k^{(1)}(\mathbf{x}^{(1)}, \mathbf{x}^{(2)}) \\ \frac{d\phi_2(\mathbf{x}^{(2)})}{dt} &= \omega_2 + \varepsilon \sum_k \frac{\partial \phi_2}{\partial x_k^{(2)}} p_k^{(2)}(\mathbf{x}^{(2)}, \mathbf{x}^{(1)})\end{aligned}\quad (2.19)$$

The perturbations of the amplitudes are small, so we can substitute the values of the variables $(\mathbf{x}^{(1)}, \mathbf{x}^{(2)})$ on the cycles, and there these variables are functions of the phase only. We thus obtain:

$$\begin{aligned}\frac{d\phi_1}{dt} &= \omega_1 + \varepsilon Q_1(\phi_1, \phi_2) \\ \frac{d\phi_2}{dt} &= \omega_2 + \varepsilon Q_2(\phi_2, \phi_1)\end{aligned}\quad (2.20)$$

These periodic functions $Q_{1,2}$ can be represented as double Fourier series:

$$\begin{aligned}Q_1(\phi_1, \phi_2) &= \sum_{k,l} a_1^{k,l} e^{ik\phi_1 + il\phi_2} \\ Q_2(\phi_2, \phi_1) &= \sum_{k,l} a_2^{l,k} e^{ik\phi_1 + il\phi_2}\end{aligned}\quad (2.21)$$

If we assume that the two natural frequencies $\omega_{1,2}$ are nearly in resonance ($\omega_1/\omega_2 \sim m/n$) then all the terms in the Fourier series with $k = nj, l = -mj$ are resonant and are not contributed. As a result we obtain,

$$\begin{aligned}\frac{d\phi_1}{dt} &= \omega_1 + \varepsilon q_1(n\phi_1 - m\phi_2) \\ \frac{d\phi_2}{dt} &= \omega_2 + \varepsilon q_2(m\phi_2 - n\phi_1)\end{aligned}\quad (2.22)$$

where:

$$\begin{aligned}q_1(n\phi_1 - m\phi_2) &= \sum_j a_1^{nj, -mj} e^{ij(n\phi_1 - m\phi_2)} \\ q_2(m\phi_2 - n\phi_1) &= \sum_j a_2^{mj, -nj} e^{ij(m\phi_2 - n\phi_1)}\end{aligned}\quad (2.23)$$

By introducing new variables for the difference between the phases of two oscillators $\psi = n\phi_1 - m\phi_2$, for the detuning $v = m\omega_2 - n\omega_1$ and for the whole interaction $q(\psi) = nq_1(\psi) - mq_2(-\psi)$ we obtain again the equation:

$$\frac{d\psi}{dt} = -v + \varepsilon q(\psi)\quad (2.24)$$

In the case of synchronization, Eq. 2.24 has a stable fixed point ψ_0 and the observed frequencies of the oscillators are:

$$\begin{aligned}\Omega_1 &= \omega_1 + \varepsilon q_1(\psi_0) \\ \Omega_2 &= \omega_2 + \varepsilon q_2(-\psi_0)\end{aligned}\tag{2.25}$$

In the simplest case of the resonance ($\omega_1 \sim \omega_2$), we should put $m = n = 1$. Moreover, we assume that the coupling is symmetric ($q_1(\psi) = q_2(\psi)$), so $q(\psi) = nq_1(\psi) - mq_2(-\psi) = mq_2(\psi) - nq_1(\psi) = -q(-\psi)$ and we get an antisymmetric coupling function. The simplest and the most natural antisymmetric and periodic function is sinusoidal, and the corresponding model for the interaction of two oscillators is again the Adler equation:

$$\frac{d\psi}{dt} = -v + \varepsilon \sin \psi\tag{2.26}$$

For this equation, if $\varepsilon < 0$, then the stable value of the phase difference ψ lies in the region $-\pi/2 < \psi < \pi/2$, and, in particular, for zero frequency detuning v the stable phase difference is zero. If $\varepsilon > 0$, the stable phase difference is in the interval $\pi/2 < \psi < 3\pi/2$, and for natural frequencies in resonance regime it is equal to π . The two types of synchronous motion are called "in-phase" and "anti-phase" (or "out-of phase").

2.2.3 Two coupled lasers

In Chapter 1, Subsection 5.1, we introduced an example of the simplest coupling scheme between two solid state lasers. Here we refer to the phase dynamic of this system. By using polar coordinates $E_j = \varepsilon_j e^{i\phi_j}$ in Eq. 1.98 and separating real from imaginary part, we get:

$$\begin{aligned}
\frac{d\epsilon_1}{dt} &= (G_1 - 1)\epsilon_1 + k\epsilon_2 \cos(\phi_2 - \phi_1) \\
\frac{d\epsilon_2}{dt} &= (G_2 - 1)\epsilon_2 + k\epsilon_1 \cos(\phi_2 - \phi_1) \\
\frac{d\phi_1}{dt} &= \omega_1 + k\epsilon_2 \sin(\phi_2 - \phi_1) \\
\frac{d\phi_2}{dt} &= \omega_2 - k\epsilon_1 \sin(\phi_2 - \phi_1) \\
\frac{dG_1}{dt} &= \gamma \left(P - G_1 - G_1 |\epsilon_1|^2 \right) \\
\frac{dG_2}{dt} &= \gamma \left(P - G_2 - G_2 |\epsilon_2|^2 \right)
\end{aligned} \tag{2.27}$$

The lasers are coupled to each other with a small coupling strength k , and the sign of the coupling terms is chosen to account for the observed stable phase-locked state in which the lasers have a phase difference of π . By introducing new variables like the frequency detuning of the lasers ($v = \omega_1 - \omega_2$) and the phase difference ($\psi = \phi_2 - \phi_1$) and by considering the particular solution where $\epsilon_1 = \epsilon_2 = \epsilon$ and $G_1 = G_2 = G$, Eq.2.27 reduce [Erneux et al., 2010; Thornburg et al., 1997] to the following three equations:

$$\begin{aligned}
\frac{d\epsilon}{dt} &= \epsilon(G - 1 - k \cos(\psi)) \\
\frac{dG}{dt} &= \gamma \left(P - G - G |\epsilon|^2 \right) \\
\frac{d\psi}{dt} &= -v + 2k \sin(\psi)
\end{aligned} \tag{2.28}$$

The last equation is exactly the Eq. 2.26 for the phase difference ψ . Since both ϵ and G do not appear in this equation, the variations of ψ are autonomous, and ϵ and G are slaved to ψ . A phase-locking occurs if $|v| < 2k$. The situation is however completely different outside the locking region. If the condition of phase locking is violated, $\cos(\psi)$ is a pulsating function of time that is driving the field ϵ .

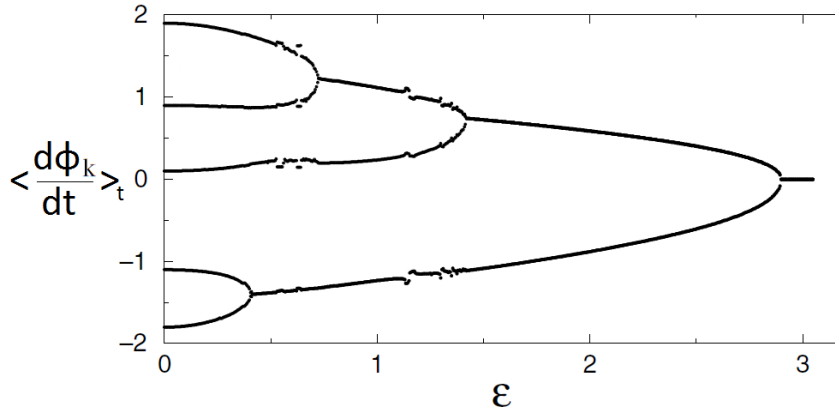


FIGURE 2.3: The observed frequencies versus the coupling constant ϵ of five coupled oscillators. The coupling function is $q(x) = \sin x$. Increasing the coupling strength the oscillators starts to form clusters moving gradually to the full synchronization. (redrawn from Figure 11.1 of [Arkady et al., 2001])

2.2.4 Synchronization in a discrete lattice

A discrete medium is a system, where each element can be assumed as a self-sustained oscillator. We will start with a description of the phase dynamics in lattices where different sites can oscillate with different periods and phases. This is a natural generalization of the system of two coupled systems as we described in Subsection.2.2.1. We begin by considering a one-dimensional chain of oscillators assuming that nearest neighbors interact. If the coupling is weak and identical for all pairs, the approximation of phase dynamics can be used and the equations can be written in the form:

$$\frac{d\phi_k}{dt} = \omega_k + \epsilon q(\phi_{k-1} - \phi_k) + \epsilon q(\phi_{k+1} - \phi_k) \quad (2.29)$$

The index $k = 1, \dots, N$ denotes the serial order of each oscillator and ω_k the corresponding natural frequency. We used periodical boundary conditions where $\phi_1 = \phi_N$. There are two limit cases. If the coupling is zero the phase of each oscillator rotates with its own natural frequency. In the other limiting case, when the coupling is very large $\epsilon \gg |\omega_k|$, the differences in the natural frequencies are negligible, and hence all oscillators eventually synchronize. In between these situations we expect to find regimes with partial synchronization, where several different frequencies are present. As the coupling tends to synchronize nearest neighbors, clusters of synchronized oscillators are observed. This has been illustrated numerically for a lattice of

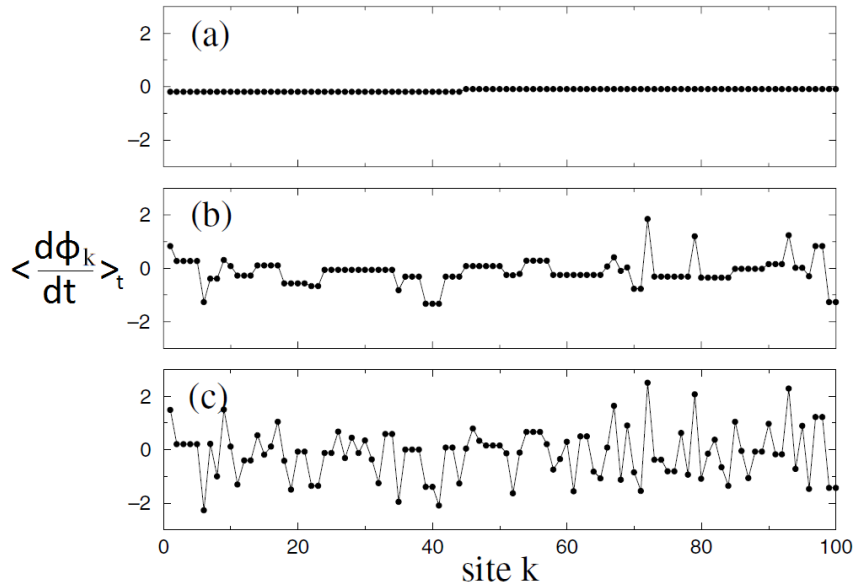


FIGURE 2.4: The mean frequency in time of the individual oscillators in an array of 100 phase oscillators with random natural frequencies. The coupling function is $q(x) = \sin x$. (a) $\epsilon = 4$. (b) $\epsilon = 1$ and (c) $\epsilon = 0.2$. (redrawn from Figure 11.2 of [Arkady et al., 2001])

five oscillators (see Fig. 2.3). The transition between the two limiting cases depends on the distribution of frequencies ω_k . The most popular that have been considered in many manuscripts are the random distribution of natural frequencies and the linear distribution. The transition from complete synchronization to the state with two clusters can be treated analytically. As the first step we substitute the phase difference between the neighboring sites, $\psi_k = \phi_{k+1} - \phi_k$, into Eq. 2.29 and obtain:

$$\frac{d\psi_k}{dt} = v_k + \epsilon [q(\psi_{k-1}) + q(\psi_{k+1}) - 2q(\psi_k)] \quad (2.30)$$

Here $v_k = \omega_{k+1} - \omega_k$ are the frequency differences where $k = 1, \dots, N - 1$. For the steady state where $\psi_k = 0$ we get a system of $N - 1$ equations with $u_k = q(\psi_k)$ unknown possible solutions. The problem is in inverting this relation and finding $\psi_k = q_{u_k}^{-1}$. It is known [Ermentrout et al., 1984] that Eq. 2.30, in the case where $v_k = 0$ and $q(\phi) = \sin \phi$, has $2N - 1$ attractors, but only one stable solution which depends on the sign of k . For $k < 0$ only the completely in-phase solution is stable, while for $k > 0$ only the completely anti-phase solution is stable. In the general case the coupling function $q(\psi)$ is periodic and has been proved that many inverse solutions can exist in the

interval (q_{min}, q_{max}) . In particular, in the same work it has been shown that, if the coupling function has one minimum and one maximum, from all possible $2N - 1$ roots only one solution is stable, whereas other fixed points are saddles and unstable nodes. At some critical coupling we can have $u_l = q_{min}$ or $u_l = q_{max}$ where the stable fixed point disappears through a saddle-node bifurcation and a periodic orbit appears. The phase space of the above system is an $N - 1$ -dimensional torus, and the appearing periodic trajectory rotates in the direction of the variable ψ_l where $\psi_k = 0$ for all k except for $k = l$, where $\psi_l \neq 0$. Therefore, all oscillators from 1 to l have the same frequency, whereas from $l + 1$ to N has a different value. Thus, two clusters of synchronized oscillators appear. Further, by decreasing the coupling strength we obtain bifurcations at which clusters split again into two parts. For a large lattice and random natural frequencies a typical picture is as in Fig. 2.4.

2.3 Chimera states

A chimera state is a spatio-temporal pattern in which a system of oscillators with identical natural frequencies or frequencies that are drawn from some known distribution splits into coexisting regions of coherent (phase locked) and incoherent (phase unlocked) oscillations. We showed that both incoherence and coherence were well demonstrated in arrays of non-identical coupled oscillators, but complete incoherence and partial coherence were usually stable at different coupling strengths. Here, we introduce the Kuramoto model in which a population of oscillators splits into two parts, one synchronized and one desynchronized. This finding is a striking manifestation of symmetry breaking, since oscillators break synchrony even when they are identical and symmetrically coupled. Before we start to present in more details the idea and the relating results, it is worth noting that the name comes from the Greek mythology. There, the chimera was a fierce fire-breathing hybrid of a lion, a goat and a snake and in physics has the meaning of a surprising mathematical hybrid like a state of mixed synchronous and asynchronous behaviour in a network of coupled oscillators.

2.3.1 Globally coupled oscillators

The synchronization between two coupled oscillators as we described previously can be generalized to systems where the oscillators can interact not only with neighbours but also with many other oscillators. Here we consider a model of N mutually coupled oscillators having different natural frequencies ω_k . The dynamics for this case are governed by the equation [Kuramoto, 1984]:

$$\frac{d\phi_k}{dt} = \omega_k + \frac{\epsilon}{N} \sum_{j=1}^N \sin(\phi_j - \phi_k) \quad (2.31)$$

The parameter ϵ determines the coupling strength which is rescaled with the population of the oscillators N to avoid the growth of force acting on each oscillator with the size of the population. Then, we introduce the complex mean field of the population according to:

$$Ke^{i\Theta} = \frac{1}{N} \sum_{k=1}^N e^{i\phi_k} \quad (2.32)$$

With this formula we can reconstruct Eq. 2.31 as a system of oscillators forced by the mean field, by obtaining the imaginary part of Eq. 2.32,

$$\frac{d\phi_k}{dt} = \omega_k + \epsilon K \sin(\Theta - \phi_k) \quad (2.33)$$

where the parameter K has a special role. From Eq. 2.32 we see that if all the frequencies are different, then the phases ϕ_k are uniformly distributed in the complex unit circle, and the amplitude of the mean field K vanishes. In this case $d\phi_k/dt = \omega_k$, so each element oscillates with its own natural frequency. Conversely, if some oscillators in the population lock to the same frequency, then their fields sum coherently and $K \neq 0$ and this state is less trivial. A nonzero K means that at least some oscillators are synchronized. Numerical simulations of Eq. 2.33 are in Fig. 2.5.

Now, if we take a symmetric distribution of the ω_k , it is natural to suppose that the coherent oscillators will be those who have ω_k near to the central frequency $\bar{\omega}$ of this distribution. So, we set $\Theta = \bar{\omega}t$ and $\psi_k = \phi_k - \bar{\omega}t$ to

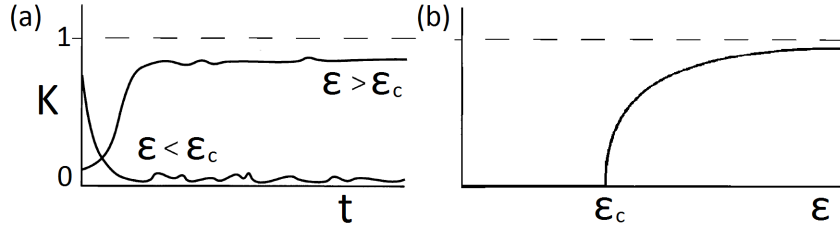


FIGURE 2.5: (a) Numerical simulations for a typical evolution of K for the Kuramoto model. (b) Dependence of the parameter K on the coupling strength ϵ (redrawn from Figure 2 and 3 of [Strogatz, 2000])

obtain:

$$\frac{d\psi_k}{dt} = (\omega_k - \bar{\omega} - \epsilon K \sin(\psi_k)) \quad (2.34)$$

This relation is an Adler equation where the synchronous solution exist when $|\omega_k - \bar{\omega}| \leq \epsilon K$ and the asynchronous solution when $|\omega_k - \bar{\omega}| > \epsilon K$.

The next step is to find the contributions of the sub-populations of synchronous and asynchronous oscillators to the amplitude of the mean field. To do that we take the limit $N \rightarrow \infty$ where now the distribution of ω_k is a continuous function $g(\omega)$. Can be proved [Arkady et al., 2001] that the relation between the parameter K and the phase differences ψ (where ψ now is a continuous function of k) comes through the distribution of all natural frequencies $g(\omega)$ with those two relations:

$$\int_{-\frac{\pi}{2}}^{\frac{\pi}{2}} \cos(\psi) \sin(\psi) g(\bar{\omega} + \epsilon K \sin(\psi)) d\psi = 0 \quad (2.35)$$

$$\int_{-\frac{\pi}{2}}^{\frac{\pi}{2}} \cos^2(\psi) g(\bar{\omega} + \epsilon K \sin(\psi)) d\psi = 1/\epsilon \quad (2.36)$$

The first equation determines the amplitude of the mean field K and the second determines the frequency. For a closed analytical solution we have to choose a special distributions $g(\omega)$. Consider for example the Lorentzian distribution,

$$g(\omega) = \frac{\gamma}{\pi [(\omega - \bar{\omega})^2 + \gamma^2]} \quad (2.37)$$

we ones get for the coupling:

$$K = \sqrt{1 - \frac{2\gamma}{\epsilon}} \quad (2.38)$$

This relation is valid if $\epsilon > 2\gamma$. Nevertheless, the transition to synchronization (see Fig. 2.5 (b)) can be characterized by $K \sim (\epsilon - \epsilon_c)^{1/2}$ where $\epsilon_c = 2\gamma$ and this is true for general distributions $g(\omega)$. Indeed, for small K only the oscillators with the frequency near the synchronization threshold $\omega = \bar{\omega}$ are synchronized. Thus, for small K we can expand $g(\bar{\omega} + \epsilon K \sin \psi)$ in a Taylor series,

$$g(\bar{\omega} + \epsilon K \sin \psi) \sim g(\bar{\omega}) + \frac{g''}{2} \epsilon^2 K^2 \sin^2 \psi \quad (2.39)$$

where, after substitution in Eq. 2.35 we have:

$$\epsilon_c = \frac{2}{\pi g(\bar{\omega})} \quad K \sim \pm \sqrt{\frac{8g(\bar{\omega})}{|g''|\epsilon^2}} \sqrt{\epsilon - \epsilon_c} \quad (2.40)$$

2.3.2 Identical coupled oscillators

In the previous subsection the all to all coupled scheme of oscillators allows the splitting of the population into the two groups where the oscillators near the center of the frequency distribution lock together at the mean frequency $\bar{\omega}$ while those in the tails of the distribution run near their natural frequencies. This coexistence is not only possible due to heterogeneities in the natural frequencies ω_k . Kuramoto and Battogtokh observed this behaviour even when all of the oscillators were identical. They considered the system:

$$\frac{\partial \phi}{\partial t} = \omega - \epsilon \int G(x - x') \sin(\phi(x, t) - \phi(x', t) + a) dx' \quad (2.41)$$

and they observed that only non-local/non-global coupling and non-zero phase lag a were required to observe coexistence of coherent and incoherent oscillators.

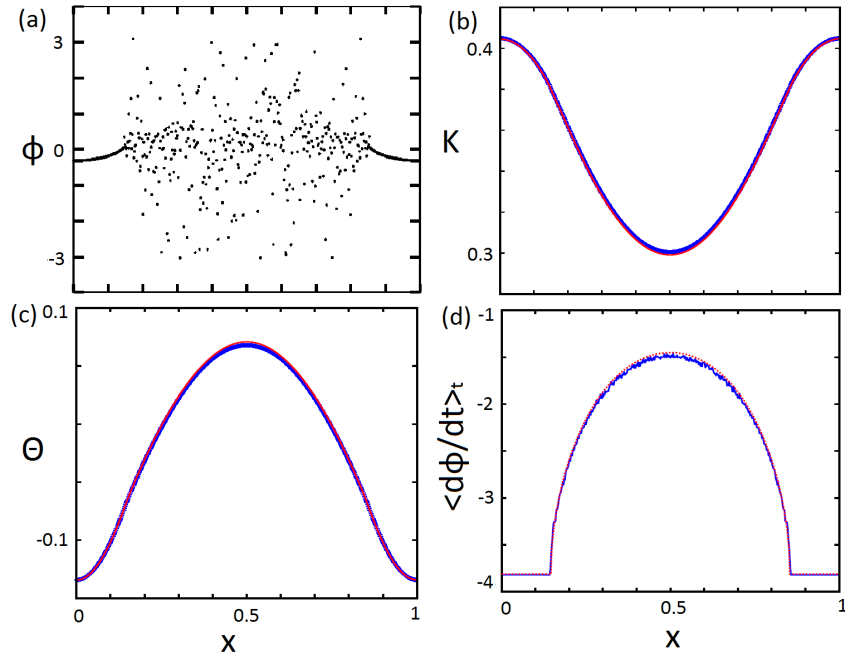


FIGURE 2.6: (a) Numerical results of the spatial distribution of the phases obtained for an array of 512 oscillators with periodic boundary conditions. Parameter: $a = 1.457$ and $\epsilon = 4$. (b) Spatial profiles of the long-time average of the order parameter amplitude K . (c) The same for the phase order parameter Θ , (d) and for the actual frequencies. With the blue color we present the numerical results while the red color indicates the theoretical curves. (redrawn from Figure 1 and 2 of [Kuramoto et al., 2002])

To achieve this observation we introduce again, the relative phase deviation $\psi = \phi - \bar{\omega}t$ from an arbitrary central frequency $\bar{\omega}$ and we obtain:

$$\frac{\partial \psi}{\partial t} = \omega - \bar{\omega} - \epsilon \int G(x - x') \sin(\psi(x, t) - \psi(x', t) + a) dx' \quad (2.42)$$

As in the theory of synchronization for globally coupled oscillators with frequency distribution, we introduce a complex order parameter with amplitude K and phase Θ through:

$$\epsilon \int G(x - x') e^{i\psi(x', t)} dx' = K(x, t) e^{i\Theta(x, t)} \quad (2.43)$$

The above quantity is space dependent but still very useful. Here, we are practically working with an assembly of independent oscillators under the

control of a common forcing field represented by K and Θ . This allows us to rewrite Eq. 2.42 in terms of this common forcing field:

$$\frac{\partial \psi(x, t)}{\partial t} = \omega - \bar{\omega} - K(x, t) \sin(\psi(x, t) + \Theta(x, t) + a) \quad (2.44)$$

The numerical and theoretical time average of spatial profiles of $K(x)$ and $\Theta(x)$ are showed in Fig. 2.6 (b) and (c), respectively. Here we present only the results of Kuramoto and Battogtokh (see [Kuramoto et al., 2002]). We see that the forcing mean-field amplitude is stronger near the boundaries and weaker near the center of the system. Figure. 2.6 (d) shows the time average of $d\phi/dt$. In the coherent domain, the oscillation frequencies have an identical value while in the incoherent domain they are distributed to a well-defined continuous curve. From those figures it has been clear that the system is divided into two subgroups of oscillators (Fig. 2.6 (a)). In the first group, the forcing amplitude is large enough so that they oscillate with an identical frequency $\bar{\omega}$. In the second group, in contrast, the forcing amplitude is too weak, so that the frequencies of the individual oscillators differ from $\bar{\omega}$.

For an investigation of the role of phase lag a we move to a more familiar formulation where by discretizing the domain and defining $K_{ij} = G(x_i - x_j)$ we obtain:

$$\frac{\partial \phi_i}{\partial t} = \omega - \frac{\epsilon}{N} \sum_{j=1}^N K_{ij} \sin(\phi_i - \phi_j + a) \quad (2.45)$$

There are two interpretations for this parameter. First, the phase lag can be interpreted as an approximation for a time-delayed coupling when the delay τ is small. To see this, consider the system:

$$\frac{\partial \phi_i}{\partial t} = \omega - \frac{\epsilon}{N} \sum_{j=1}^N K_{ij} \sin(\phi_i(t) - \phi_j(t - \tau)) \quad (2.46)$$

When $\tau \ll 2\pi/\omega$ and ϵ sufficiently small, we can approximate the phase through the Taylor expansion,

$$\phi_j(t - \tau) \sim \phi_j(t) - \tau \frac{d\phi_j(t)}{dt} \sim \phi_j(t) - \tau\omega \sim \phi_j(t) - a \quad (2.47)$$

where $a = \tau\omega$. Thus phase lag can be thought of as a proxy for time delay that allows us to replace a system of an effectively infinite-dimensional delay differential equations with a system of ordinary differential equations [Crook et al., 1997]. A second interpretation can be seen by rewriting the coupling term in the form

$$\sum_{j=1}^N K_{ij} \sin(\phi_i - \phi_j + a) = \cos(a) \sum_{j=1}^N K_{ij} \sin(\phi_i - \phi_j) + \sin(a) \sum_{j=1}^N K_{ij} \cos(\phi_i - \phi_j) \quad (2.48)$$

When $a = 0$, only the sine coupling remains. In this case, complete synchronization is the norm. When $a = \pi/2$, pure cosine coupling results in an integrable Hamiltonian system [Watanabe et al., 1993]. This causes disordered initial states to remain disordered. Thus a determines a balance between the complete synchronization and complete disorder.

2.3.3 General coupling function and additional features

So far, only the simplest attractive coupling proportional to the sinusoidal of phase difference has been considered. Here we will demonstrate that more complex coupling functions can lead to a further complication of the collective dynamics. Okuda [Okuda, 1993] has shown that a general coupling function $q(\phi)$ between identical oscillators can result in the formation of several clusters. All oscillators in a cluster have the same phase, and there is a constant phase shift between different clusters. The model reads:

$$\frac{d\phi_k}{dt} = \omega + \frac{\epsilon}{N} \sum_{j=1}^N q(\phi_j - \phi_k) \quad (2.49)$$

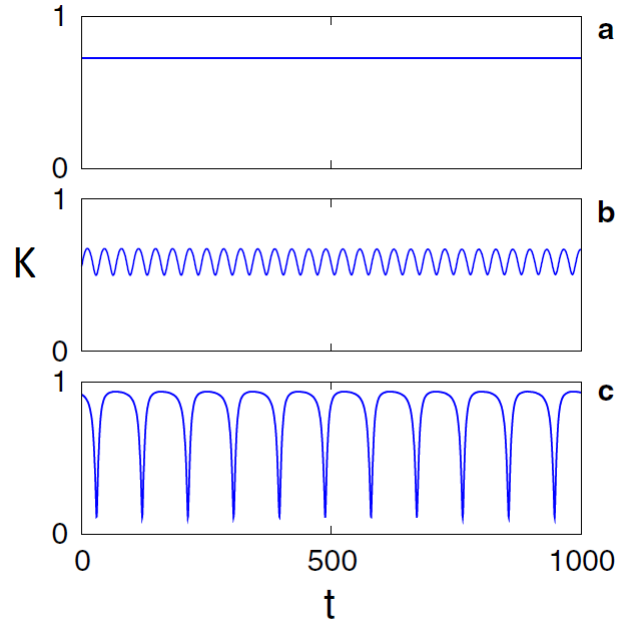


FIGURE 2.7: The order parameter K over time for 128 coupled oscillators in each population. (a) Stable chimeras, (b) breathing chimeras and (c) long-period breather (redrawn from Figure 2 of [Abrams et al., 2008])

If the periodic ($q(\phi) = q(\phi + 2\pi)$) coupling function q contains higher harmonics, formation of clusters may be observed for some initial conditions.

A general coupling function $q(\phi)$ between oscillators with a distribution of natural frequencies has been investigated by Daido who introduced the concept of "order function". The formulation of the equation has the form:

$$\frac{d\phi_k}{dt} = \omega_k + \frac{\epsilon}{N} \sum_{j=1}^N q(\phi_j - \phi_k) \quad (2.50)$$

The coupling function q can be, in general, represented as a Fourier series:

$$q(\phi) = \sum_l q_l e^{i2\pi l \phi} \quad (2.51)$$

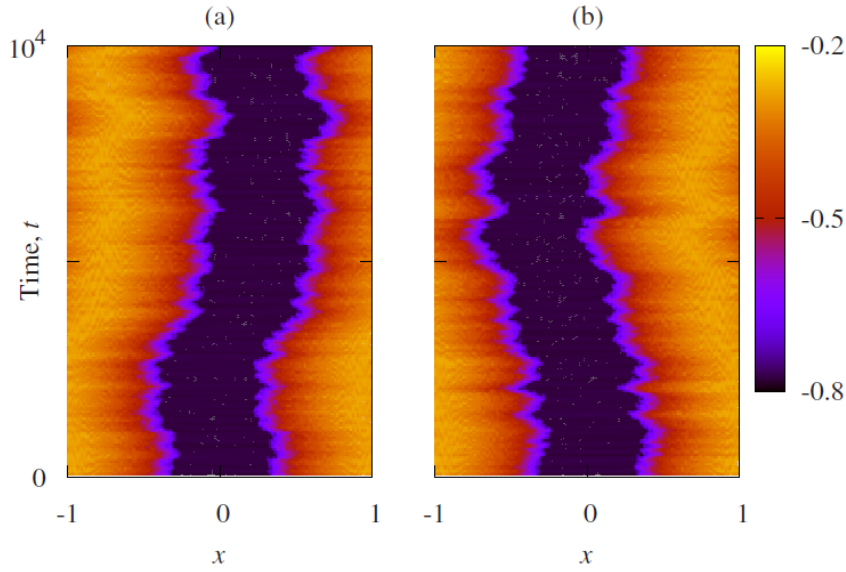


FIGURE 2.8: Two chimera trajectories with different initial conditions for 200 oscillators. This difference is very small (10^{-3}) showing the sensitivity in initial conditions. The color coded the time average of the frequency for each oscillator. (redrawn from Figure 2 of [Omel'Chenko et al., 2010])

Supposing that the phases of all synchronous oscillators rotate with a frequency $\bar{\omega}$, we can introduce generalized order parameters as,

$$Z_l = \frac{1}{N} \sum_{k=1}^N e^{i2\pi l(\phi_k - \bar{\omega}t)} \quad (2.52)$$

and rewrite the equations of motion as,

$$\frac{d\phi_k}{dt} = \omega_k - \epsilon H(\phi_k - \bar{\omega}t) \quad (2.53)$$

where:

$$H(\psi) = - \sum_{k=1}^N q_l Z_l e^{-i2\pi l\psi} \quad (2.54)$$

The function H is the mean force that acts on each oscillator, and it is called the order function. It is a generalization of the mean field used by Kuramoto in his analysis. A nonzero order function is an indication of synchronization in the population. Daido [Daido, 1992; Daido, 1993] has shown

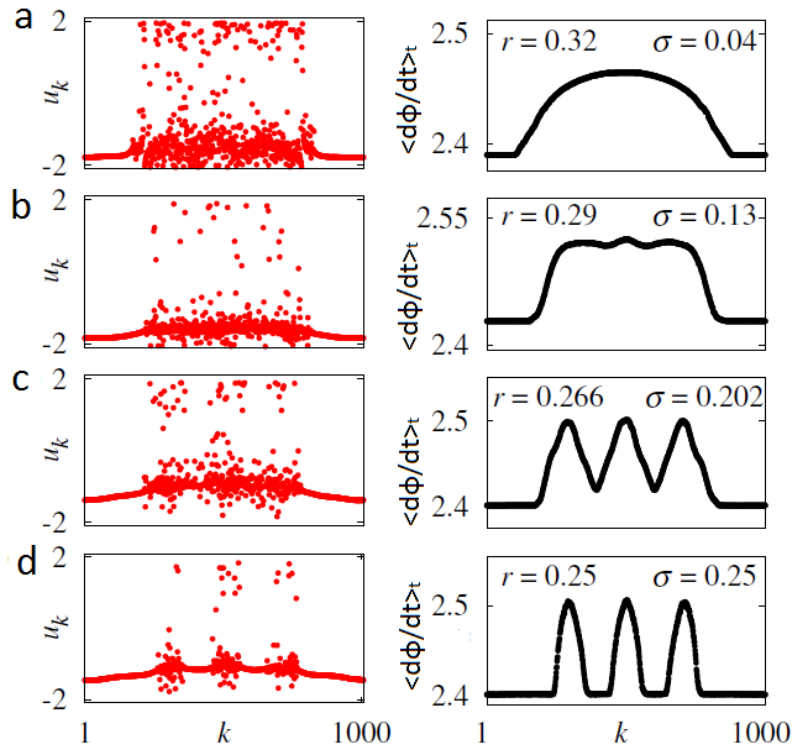


FIGURE 2.9: Transition from a classical chimera state with one incoherent domain to multichimera states with two (a)-(d), and three (c)-(d) incoherent domains. The left column shows snapshot of the amplitude of the FitzHugh-Nagumo oscillator and the right column shows the corresponding time average of each oscillator frequency. From the top to the bottom the range of coupling between the oscillators is decreasing. (redrawn from Figure 4 of [Omelchenko et al., 2013])

analytically that near the synchronization threshold, the norm of the order function is proportional to the bifurcation parameter $\|H\| \sim \epsilon - \epsilon_c$. This result demonstrates that the square-root derived by Kuramoto for is not valid for a general coupling function.

Beyond the splitting of the system into a coherent and incoherent domain, by changing the parameters or the topological setting of the coupling, additional features can be observed. A different type of partial synchronization, the so called breathing chimeras has been discovered by Abrams [Abrams et al., 2008]. In that work they obtain some results about the stability of chimera states by analyzing a minimal model consisting of two interacting populations of oscillators. A pair of oscillator populations in which each oscillator is coupled equally to all the others in its group, and less strongly to those

in the other group. In Fig. 2.7 the order parameter of the dynamical system has been plotted. Figure 2.7 (a) illustrates numerical results for chimera states since the order parameter is constant and greater than zero while in Fig. 2.7 (b) and (c) for different parameters the order parameter pulsates, and the chimera starts to breathe. Similar works with two interacting populations have been done by Laing [Laing, 2009] where heterogeneity in frequency distribution has been found to destroy the chimera states, to destroy all states except chimeras, or destabilize chimeras, depending on the form of the heterogeneity. Moreover, they systematically have investigated the effects of gradually removing connections within the network [Laing et al., 2012] and found that oscillations of chimera states can be either created or suppressed, depending on exactly how the connections are gradually removed.

The spatiotemporal behavior of chimera states in arrays of nonlocally coupled phase oscillators has been investigated also by [Omel'Chenko et al., 2010]. An irregular motion of the position of the coherent and incoherent regions with a regular macroscopic pattern in space, and an irregular motion in time has been found. This motion was a finite-size effect that was not observed in the limit of the system size ($N \rightarrow \infty$). These structures were very sensitive to initial conditions (see Fig. 2.8) exhibiting in time, chaotic fluctuations to their position. Moreover, the same group has reported another novel form of chimeras states [Omelchenko et al., 2013]. More specifically, in a model with a ring of N nonlocally coupled FitzHugh-Nagumo oscillators (a typical model for excitable systems) they have found that, depending on the coupling strength and range, different multi-chimera states (see Fig. 2.9) arise in a transition from classical chimera states.

2.3.4 Experiments and applications

For a long time the experimental observation of chimera states was a difficult task. Many numerical simulations have shown chimera behaviour by a carefully chosen set of initial conditions. This sensitivity to the initial state was the main problem for experimental proofs.

However, after 2012 a lot of research groups overcame this obstacle. Kenneth Showalter and his group used for the first time the Belousov-Zhabotinsky reaction to create a realization of a two-cluster chimera states [Tinsley et al.,

2012]. They used a population of photosensitive chemical oscillators and after dividing it into two groups and using light to provide feedback for each reaction, they observed a variety of dynamical patterns including complete synchronization, synchronized clusters and chimera states. Oscillators of the same group were strongly coupled to the mean intensity and weakly coupled to the mean intensity of the opposite group. They also induced a fixed time delay between the interaction of the separations groups. Similar experiment, this time on a non-locally coupled one-dimensional ring of oscillators has shown again chimera-like patterns [Nkomo et al., 2016].

In optics, Rajarshi Roy and his group designed a coupled map lattice using a liquid-crystal spatial light modulator to achieve optical nonlinearity controlled by a computer with feedback from a camera. They reported chimeras on both one-dimensional rings and two-dimensional lattices with periodic boundaries [Hagerstrom et al., 2012]. In those discrete-time system the phase was not a continuous variable, so chimeras states were more generalized chimeras.

In mechanical systems, Erik Martens and his colleagues used metronomes, placed them on swings coupled by springs. The vibrations of the swings provided strong coupling between oscillators on the same swing, and the springs weakly coupled metronomes on opposite swings. By varying the spring constant they were able to observe chimera states along with the expected in-phase and anti-phase synchronous states [Martens et al., 2013].

From the viewpoint of applications many natural phenomena may relate with chimera states. In biology, many species become involved in unihemispheric slow wave sleep. This means that one brain hemisphere appears to be inactive while the other remains active. The neural activity during this state reveals high amplitude and low frequency electrical activity in the sleeping hemisphere, while the other hemisphere is more unstable. Ma, Wang and Liu [Ma et al., 2010] reproduced this splitting of the synchronization by a model like the Kuramoto one and found that for different reactions to environmental forcing and for appropriate choice of coupling strengths, periods of coherence and incoherence alternated in each hemisphere.

In engineering, many generators produce power at the same frequency. Adilson E. Motter et al used a Kuramoto-like model to study the synchronization of a power grid [Motter et al., 2013]. By the assumption that the network structure of generators is fixed and the power demand is constant, they

founded that perturbations to the network can cause full or partial desynchronization, leading some times to blackouts. By managing the possibility of chimera states in power distribution networks the possibility, as they emphasize, for a stable and robust synchrony in a power grid is high.

Finally, in social systems chimera states may also be possible. Gonz'alez-Avella et al [González-Avella et al., 2014] used a model for cultural trends. They observed that coupled populations can exhibit chimera-like patterns in which a part from the population is synchronized while the second population remains disordered.

Chapter 3

Turbulent chimeras in large semiconductor laser arrays

3.1 Introduction

Semiconductor lasers are enabling components in multiple platform applications spanning optical communication networks to laser surgery and sensing. Recent works include impressive advances in high-speed lasers with low power consumption, high-power vertical external cavity surface emitting lasers and high-speed beam steering with phased vertical cavity laser arrays. Significant advances have been made in nitride based lasers, record-high temperature operation quantum dot lasers, and the field of nanolasers with ultralow volume and threshold is coming to technological maturity [Johnson et al., 2013].

Of special importance for next generation applications such as laser radars, is the design of photonic integrated semiconductor laser arrays that consist of a very large number of properly coupled photonic emitters [Heck, 2013]. It is well known that phase locking of an array of diode lasers is a highly effective method in beam shaping because it increases the output power and reduces the overall needed lasing threshold. Recent work on phase-locked laser arrays through global antenna mutual coupling has employed custom made nano-lasers [Kao et al., 2016]. Moreover, reconfigurable semiconductor laser networks based on diffractive coupling using Talbot geometry have been studied on commercially available vertical cavity diode lasers [Brunner et al., 2015].

In this Chapter, we are interested in the collective behavior of a large array

of semiconductor lasers with nearest-neighbor coupling. The crucial parameters for the observed dynamics are the coupling strength and the relative optical frequency detuning between the lasers, which introduces realistic inhomogeneities into the system. Our focus, in particular, is to identify the parameter regions where chimera states emerge and subsequently characterize these states using suitable classification measures [Kemeth et al., 2016]. introduced in Chapter 3. For over a decade now, a number of works has been dedicated to this phenomenon of coexisting synchronous and asynchronous oscillatory behavior. The latest developments in this field involve their study in physical, higher-dimensional systems beyond phase oscillators.

Coupled lasers have been extensively studied in terms of nonlinear dynamics [Kozyreff et al., 2000; Oliva et al., 2001; Uchida et al., 2001; Dahms et al., 2012] and [Soriano et al., 2013] (with references therein) and synchronization phenomena [Lythe et al., 1997; Pecora et al., 2014; Alsing et al., 1996], but works on chimera states in laser networks have appeared only recently. In [Larger et al., 2013] chimera states were reported both theoretically and experimentally in a virtual space-time representation of a single laser system subject to long delayed feedback. Furthermore, so-called "small chimeras" were numerically observed in a network of four globally delay-coupled lasers in [Böhm et al., 2015; Röhm et al., 2016], for both small and large delays. Such chimeras exist for very small network sizes and do not require nonlocal coupling in order to emerge. In our study we use neither nonlocal, nor global coupling but simple nearest-neighbor interactions which is physically plausible for lasers, e. g., grown on a single chip. This coupling realization is less expensive computationally. Moreover, it revises the general belief that nonlocal coupling is essential for the existence of chimeras [Hizanidis et al., 2016].

We will show that the crucial parameter for the collective behavior in our system is the frequency detuning between the coupled lasers. The effect of detuning has been examined before in [Blackbeard et al., 2014] but with respect to in- and anti-phase synchronization. Moreover, transitions from complete to partial synchronization (optical turbulence) were explained, for a small array of three lasers. Here, we address the emergence of the hybrid phenomenon of chimera states in a *large* laser array and provide a quantification of these patterns using newly developed classification measures [Kemeth et al., 2016].

This Chapter is organized as follows: First, we present the model equations and the bifurcation diagrams for two coupled lasers with the coupling strength and the detuning as control parameters. Next, the collective behavior for a laser array with and without detuning is discussed, whereas various patterns including chimera states are presented and classified. Moreover, the effect of noise, the system size and the initial conditions on the observed dynamics is addressed. In the concluding section we summarize our results and discuss open problems.

3.2 Coupled semiconductor lasers

The dynamic description of semiconductor laser arrays with evanescent coupling, in polar coordinates, is illustrated by the equations,

$$\begin{aligned}
\frac{dX_j}{dt} &= \frac{g'}{2}(G_j - G_{th})X_j - \frac{k_c}{n} [X_{j+1} \sin(\phi_{j+1} - \phi_j) + X_{j-1} \sin(\phi_{j-1} - \phi_j)] \\
\frac{d\phi_j}{dt} &= -\frac{ag'}{2}(G_j - G_{th}) + \frac{k_c}{n} \left[\frac{X_{j+1}}{X_j} \cos(\phi_{j+1} - \phi_j) + \frac{X_{j-1}}{X_j} \cos(\phi_{j-1} - \phi_j) \right] \\
\frac{dG_j}{dt} &= P - \frac{G_j}{\tau_s} - \left(\frac{1}{\tau_p} + g'(G_j - G_{th}) \right)
\end{aligned} \tag{3.1}$$

where G_j is the carrier density, X_j is the amplitude, and ϕ_j is the phase of the electric field in the j th channel. The other parameters are the differential gain g' , the coupling constant k_c , the threshold carrier density G_{th} , the linewidth enhancement factor a , the pump rate P , the photon lifetime τ_p and the spontaneous carrier lifetime τ_s .

A closed form expression can be obtained by the next proper rescaling in the variables and the parameters:

$$\begin{aligned}
\mathcal{E}_j &= \sqrt{\frac{g'\tau_s}{2}} X_j & N_j &= \frac{1}{2} g' G_{th} \tau_p \left(\frac{G_j}{G_{th}} - 1 \right) \\
p &= \frac{1}{2} g' G_{th} \tau_p \left(\frac{P}{P_{th}} - 1 \right) & \eta &= \frac{k_c}{n} \tau_p & T &= \frac{\tau_s}{\tau_p}
\end{aligned} \tag{3.2}$$

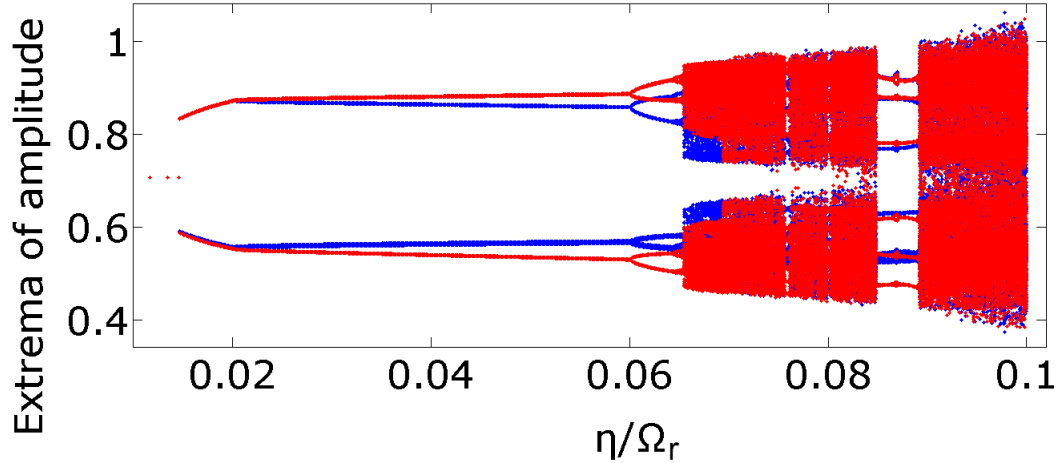


FIGURE 3.1: Amplitude maxima and minima of the electric field. The coupling strength η has been rescaled to the relaxation oscillation frequency Ω_r . Blue color refers to the first laser and red to the second one. Other parameters are: $T\Omega_r = 20$, $p = 0.5$, $\frac{1}{\Omega_r} = 20$, $a = 5$.

Then, the evolution of the slowly varying complex amplitudes \mathcal{E}_j of the electric fields and the corresponding population inversions N_j of the active medium are given by [Arecchi et al., 1984; Wicczorek et al., 2005]:

$$\begin{aligned} \frac{d\mathcal{E}_j}{dt} &= (1 - ia)\mathcal{E}_j N_j - i\eta(\mathcal{E}_{j+1} + \mathcal{E}_{j-1}) \\ T \frac{dN_j}{dt} &= (p - N_j - (1 + 2N_j)|\mathcal{E}_j|^2), \quad j = 1 \dots M \end{aligned} \quad (3.3)$$

Our system consists of an array of M locally coupled semiconductor lasers. The amplitude-phase coupling is modeled by the linewidth enhancement factor $a = 5$ and $T = 400$ is the ratio of the lifetime of the electrons in the upper level and that of the phonons in the laser cavity. The lasers are pumped electrically with the excess pump rate $p = 0.5$ which is 50% above laser threshold. The coupling strength η is a control parameter used to tune the dynamics of the system.

For the special case of two lasers in polar coordinates where $\mathcal{E}_j = E_j e^{i\phi_j}$ we get,

$$\begin{aligned}
\dot{E}_1 &= N_1 E_1 - \eta E_2 \sin \theta \\
\dot{E}_2 &= N_2 E_2 + \eta E_1 \sin \theta \\
T\dot{N}_1 &= p - N_1 - (1 + 2N_1)E_1^2 \\
T\dot{N}_2 &= p - N_2 - (1 + 2N_2)E_2^2 \\
\dot{\theta} &= -a(N_2 - N_1) + \eta(E_1/E_2 - E_2/E_1) \cos \theta
\end{aligned} \tag{3.4}$$

where $\theta = \phi_2 - \phi_1$. This system of differential equations has the following fixed points:

$$E_1 = E_2 = \sqrt{p}, N_1 = N_2 = 0, \phi_2 - \phi_1 = 0 \tag{3.5}$$

$$E_1 = E_2 = \sqrt{p}, N_1 = N_2 = 0, \phi_2 - \phi_1 = \pi \tag{3.6}$$

To investigate the stability of these steady states we introduce small perturbations and linearize Eqs. 3.4 about their steady-state values [Winful et al., 1988]. The linear system of differential equations is:

$$\begin{aligned}
\dot{E}_1 &= \sqrt{p}(N_1 - \eta\theta) \\
\dot{E}_2 &= \sqrt{p}(N_2 + \eta\theta) \\
T\dot{N}_1 &= 2\sqrt{p}E_1 - (1 + 2p)N_1 \\
T\dot{N}_2 &= 2\sqrt{p}E_2 - (1 + 2p)N_2 \\
\dot{\theta} &= - \left[a(N_2 - N_1) + \frac{2\eta}{\sqrt{p}}(E_2 - E_1) \right]
\end{aligned} \tag{3.7}$$

This system has a fifth order characteristic polynomial. We use the Routh-Hurwitz criterion to determine the parameter value regions in which the steady-state solutions are stable. After some calculations we find that the fixed point of Eq. 3.5 is stable under the condition,

$$\eta < \frac{1 + 2p}{2aT} \tag{3.8}$$

and the fixed point of Eq. 3.6 is stable for:

$$\eta > \frac{ap}{1+2p} \quad (3.9)$$

In the absence of coupling the phase variable does not influence the dynamics. In this case the intensity of the laser exhibits damped relaxation oscillations with a decay rate $\gamma = (1+2p)/2T$. To prove that we take the fix points ($E_j = \sqrt{p}, N_j = 0$) and we linearize about this steady state. The Jacobian on this critical point is,

$$J = \begin{bmatrix} 0 & \sqrt{p} \\ -\frac{2\sqrt{p}}{T} & -\frac{1+2p}{T} \end{bmatrix} \quad (3.10)$$

with:

$$\lambda_{12} = -\frac{1+2p}{2T} \pm \sqrt{\frac{2p}{T}} \quad (3.11)$$

The quantity $\Omega_r = \sqrt{2p/T}$ is the so called the relaxation oscillation frequency. Figure 3.1 depicts a numerically obtained bifurcation diagram of the maxima and minima of the amplitude of the oscillating electric field. The control parameter is the coupling strength normalized to the relaxation oscillation frequency [Kuske et al., 1997]. A Hopf bifurcation occurs at $\eta/\Omega_r = 0.01$. As the coupling is increased the limit cycle exists until $\eta/\Omega_r = 0.06$. After that, a period-doubling cascade takes place, leading to chaos. The system remains chaotic until the approximate vale of 0.084 and then enters a new limit cycle which is stable up to $\eta/\Omega_r = 0.089$, which is followed by a new period doubling cascade into a second chaotic region.

The situation is much more complicated when we consider larger arrays. If we set the saturated gain equal to the loss for all the lasers ($N_j = 0$) we obtain the steady state, in function of the cavity supermodes of M coupled waveguides with:

$$E_j^{(m)} = A \sin \left[\frac{jm\pi}{M+1} \right] \quad \Omega^{(m)} = 2\eta \cos \left[\frac{m\pi}{M+1} \right] \quad m = 1, 2, \dots, M \quad (3.12)$$

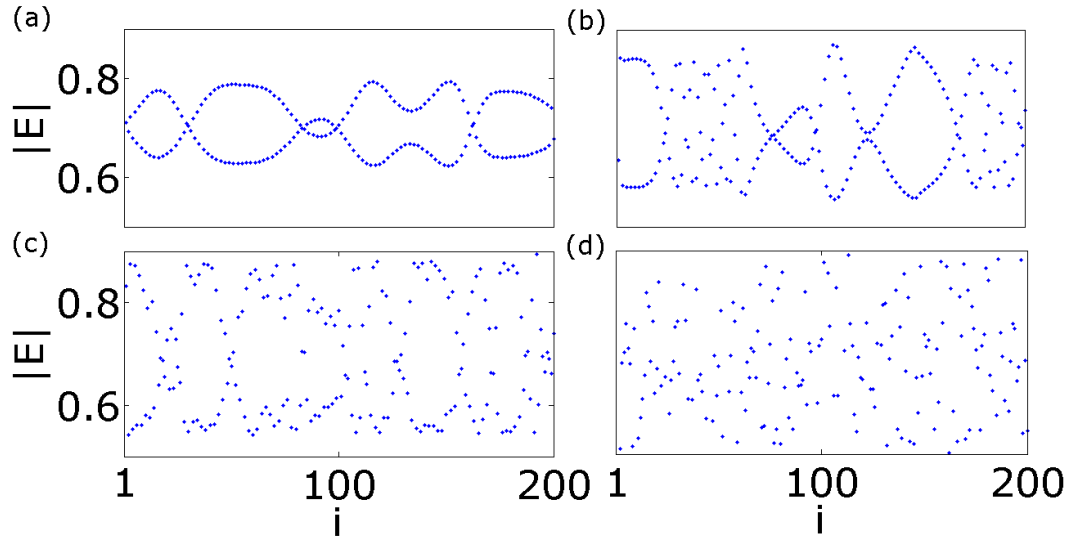


FIGURE 3.2: Snapshots of the amplitude of the electric field in an array of $M = 200$ lasers for different coupling strengths without detuning: (a) $\frac{\eta}{\Omega_r} = 0.006$, (b) $\frac{\eta}{\Omega_r} = 0.01$, (c) $\frac{\eta}{\Omega_r} = 0.02$, (d) $\frac{\eta}{\Omega_r} = 0.07$. Other parameters: $T\Omega_r = 20$, $p = 0.5$, $\frac{1}{\Omega_r} = 20$ and $a = 5$.

The frequency Ω is a possible frequency shift which play a central role in stability of the system, according to [Winful, 1992]. The maximum supermode frequency shift of M passive coupled waveguides is $\Omega^M = 2\eta \cos(m\pi/(M+1))$. In the presence of the gain medium, amplitude-phase coupling through a creates a peak frequency of $a\Omega^M$. Then, the instability will occur if $a\Omega^M > 1/T$. For the special case of the anti-phase region we have:

$$\eta < \frac{1 + 2p}{4aT \cos\left(\frac{\pi}{M+1}\right)} \quad (3.13)$$

As M increases, the critical coupling decreases roughly as $\frac{M}{M-1}$ and reaches a limiting value at large $M > 10$ which is half of that corresponding to $M = 2$. Throughout this work, we will consider an array of 200 lasers. The numerical integration has been done by using the fourth order Runge-Kutta algorithm. For faster numerical calculations we can rescale Eq. 3.3 with the laser relaxation oscillations frequency.

In Fig. 3.2 snapshots of the amplitude of the electric field are shown at $100T$, where $T_r = 2\pi/\Omega_r$ is the period of the relaxation oscillation of the free running diode laser. According to Eq. 3.13, the Hopf bifurcation for our laser

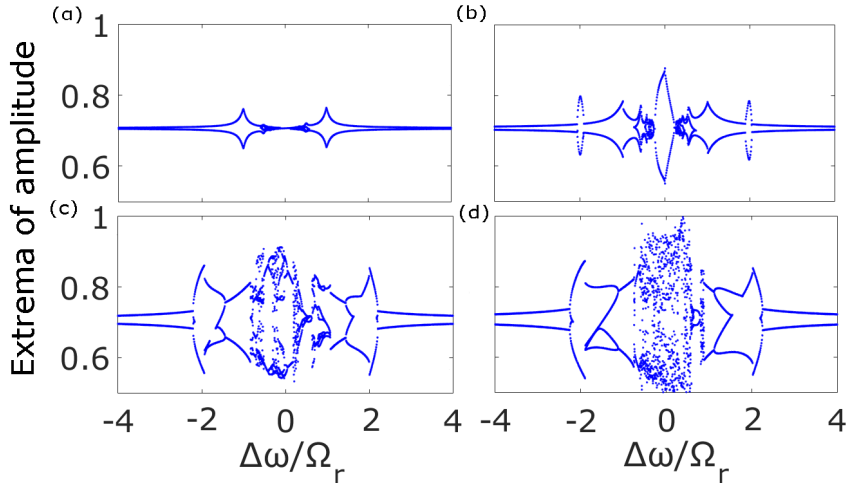


FIGURE 3.3: Extrema of the amplitude of the electric field in dependence of the detuning, for different values of the coupling strength. (a) $\frac{\eta}{\Omega_r} = 0.01$, (b) $\frac{\eta}{\Omega_r} = 0.025$, (c) $\frac{\eta}{\Omega_r} = 0.0635$, (d) $\frac{\eta}{\Omega_r} = 0.08$. The difference in the detuning $\Delta\omega_r$ has been rescaled by the relaxation oscillation frequency Ω_r . Other parameters: $T\Omega_r = 20$, $p = 0.5$, $M = 2$, $\frac{1}{\Omega_r} = 20$ and $a = 5$.

array occurs at the value $\eta/\Omega_r = 0.005$. Slightly above this value, the system demonstrates a self-organized pattern (see Fig. 3.2, (a)): The laser array splits into two sub-systems with each laser having a phase difference equal to π with its nearest neighbors (anti-phase synchronization [Blackbeard et al., 2014]). This pattern gradually vanishes with increasing coupling strength and the system becomes fully incoherent (Figs. 3.2 (c-d)).

3.3 Effect of optical frequency detuning

Apart from the coupling strength, another crucial parameter is the optical frequency detuning and its correlation with the amplitude instability and mutual coherence of the light emitted by the laser. For both solid state [Thornburg et al., 1997; Rogister et al., 2007] and semiconductor lasers [Blackbeard et al., 2014], the complexity of the system increases immensely by introducing detuning. In the presence of detuning our system consists of an array of M locally coupled semiconductor lasers in the form,

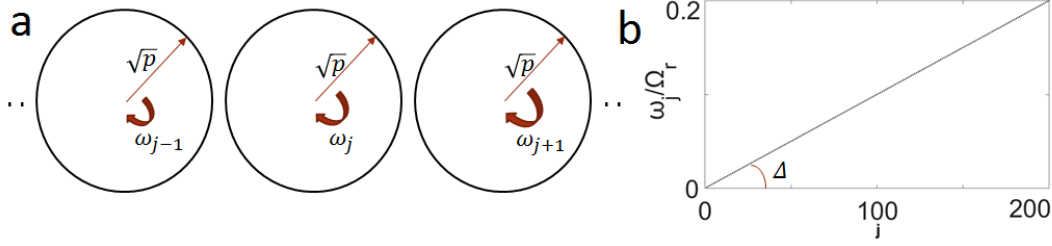


FIGURE 3.4: a) In the absence of coupling ($\eta = 0$) each laser is a limit cycle with stable amplitude equal to \sqrt{p} and a neutral rotating phase with different frequency ω_j . b) The linear distribution of detunings in space interval.

$$\begin{aligned} \frac{d\mathcal{E}_j}{dt} &= (1 - ia)\mathcal{E}_j N_j - i\eta(\mathcal{E}_{j+1} + \mathcal{E}_{j-1}) + i\omega_j \mathcal{E}_j \\ T \frac{dN_j}{dt} &= (p - N_j - (1 + 2N_j)|\mathcal{E}_j|^2), \quad j = 1 \dots M \end{aligned} \quad (3.14)$$

where the normalized angular frequency ω_j measures the optical frequency detuning of laser j from a common reference.

The bifurcation diagram of Fig. 3.3 shows the maxima and minima of the electric field amplitude in dependence of $\Delta\omega = \omega_2 - \omega_1$, rescaled by the free relaxation frequency Ω_r . This has been repeated for various values of the coupling strength (Figs. 3.3 (a-d)). We observe that in a certain range of $\Delta\omega/\Omega_r$ values the amplitude of the laser oscillations increases significantly. Moreover, for large coupling strengths (Figs. 3.3 (c,d)) the behavior of the system is rich and complex in dynamical responses. It is also noticeable that although some η values render the system chaotic in the case without detuning (see Fig. 3.1), for the same coupling strengths the dynamics is regular in the presence of detuning (Figs. 3.3 (d)).

To understand this phenomena let us calculate the stability of the system in the case where the coupling strength is zero. In polar coordinates the system has the form:

$$\begin{aligned}
\frac{dE_j}{dt} &= E_j N_j \\
\frac{d\phi_j}{dt} &= -aN_j + \omega_j \\
\frac{dN_j}{dt} &= p - N_j - (1 + 2N_j)E_j^2
\end{aligned} \tag{3.15}$$

Again, the phase variable does not influence the dynamics. By taking the fixed points ($E_j = \sqrt{p}, N_j = 0$), from Eq. 3.10 has been proven that this point is stable. However, the phase derivation is not anymore equal to zero (for that point). The phase for each individual laser is equal with the corresponding detuning parameter $d\phi_j/dt = \omega_j$. Thus, each laser is a limit cycle with stable amplitude and a neutral rotating phase with a different frequency (see Fig. 3.4 (a)). Moreover, from Fig. 3.1 we can see that in the absence of detuning and after a critical coupling strength (the Hopf bifurcation), the system has a limit cycle, in general with different frequency than ω_j . In the full system, these two limit cycles for each individual laser are interacting, delivering more complexity in the system.

For the case of an array of lasers, we incorporate detuning in the following way,

$$\frac{\omega_i}{\Omega_r} = \Delta i \tag{3.16}$$

where Δ is a constant (see Fig. 3.4 (b)).

With this distribution, the differences of the detuning have a simple form: $|\Delta\omega_{j+1}/\Omega_r| = |\Delta\omega_{j-1}/\Omega_r| = \Delta$ [Oliva et al., 2001]. Additionally, we redefine $\frac{\eta}{\Omega_r}$ as H . It is possible to realize different forms of synchronization depending on the coupling strength. One case is full synchronization, where $E_j = E_k$ holds for all lasers $j, k = 1 \dots M$ (see Fig. 3.5 (a), bottom). The behavior is therefore similar to that of the uncoupled system since the whole array ends up in the steady state (each laser is lasing with constant intensity equal to $\sqrt{p} \sim 0.7$). In a partially synchronized state the amplitudes are different in one or more lasers (see Fig. 3.5 (b), bottom) and in the unsynchronized state there is no fixed amplitude relation between the oscillators (see Fig. 3.5 (c), bottom). In Fig. 3.5 (a-c) (top) we can see all of these states depicted in the complex unit circle. The red circle denotes the steady state

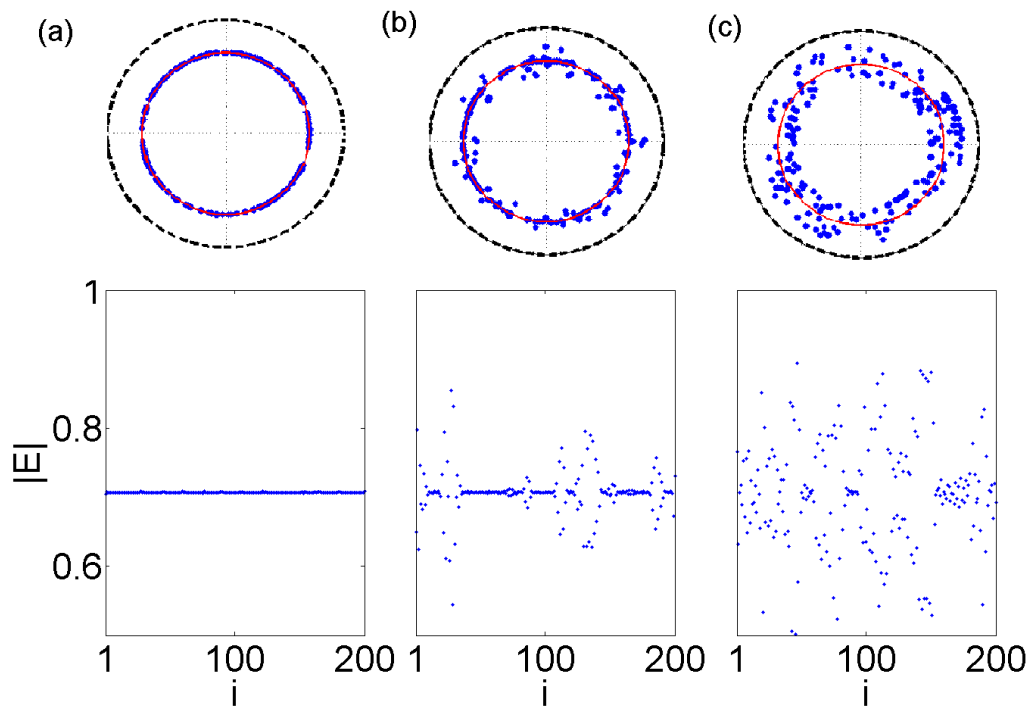


FIGURE 3.5: Top: The electric field in the complex unit circle. Bottom: Snapshots of the amplitude of the electric field for different coupling strengths and constant detuning. (a) $H = 0.008$, (b) $H = 0.014$, (c) $H = 0.026$. The red circle denotes the steady state solution of the amplitude of the electric field. Other parameters: $\Delta = 0.01$, $T\Omega_r = 20$, $p = 0.5$, $\frac{1}{\Omega_r} = 20$ and $a = 5$.

solution where the amplitude of the oscillations is constant. In Fig. 3.5 (a) the amplitudes are locked to this value, while the phases of the individual lasers are randomly distributed over the steady state solution circle. This case corresponds to amplitude (intensity) synchronization. The opposite situation is full asynchrony, displayed by Fig. 3.5 (c) where both amplitude and phase exhibit incoherent behavior. The intermediate case is shown in Fig. 3.5 (b) where an amplitude-chimera [Zakharova et al., 2014] is illustrated through the coexistence of partial amplitude locking and incoherence.

3.4 The influence of noise

In the previous section, the frequencies were chosen in the way where each laser is equal with the mean value of the two neighbourhoods ($\Delta j = (\Delta(j + 1) + \Delta(j - 1))/2$) and the distribution is linear. In this section we investigate the influence of random detunings between the lasers. The equation for the detuning distribution now reads:

$$\frac{\omega_j}{\Omega_r} = \Delta j + noise \quad (3.17)$$

The noise has been chosen from a normal random distribution with zero mean and standard deviation compared to ω_j/Ω_r . The distribution is generated by the `randn` MATLAB function for a given state of the generator.

For a total random detuning between the lasers we have found a full unsynchronised intensity on the array of lasers in time. However, in the case where the standard deviation is lower than $\omega_j/2\Omega_r$ the behavior of the system remains similar with the case of zero noise. In Fig. 3.6 we illustrate the system in the presence of noise with the same parameters as in Fig. 3.5 (bottom). The similarity is clear even for standard deviation equal to $\omega_j/2\Omega_r$.

3.5 Suitable measures

Our next step is to characterize the observed states by using suitable measures. Recently, has been presented a very usefull classification scheme for

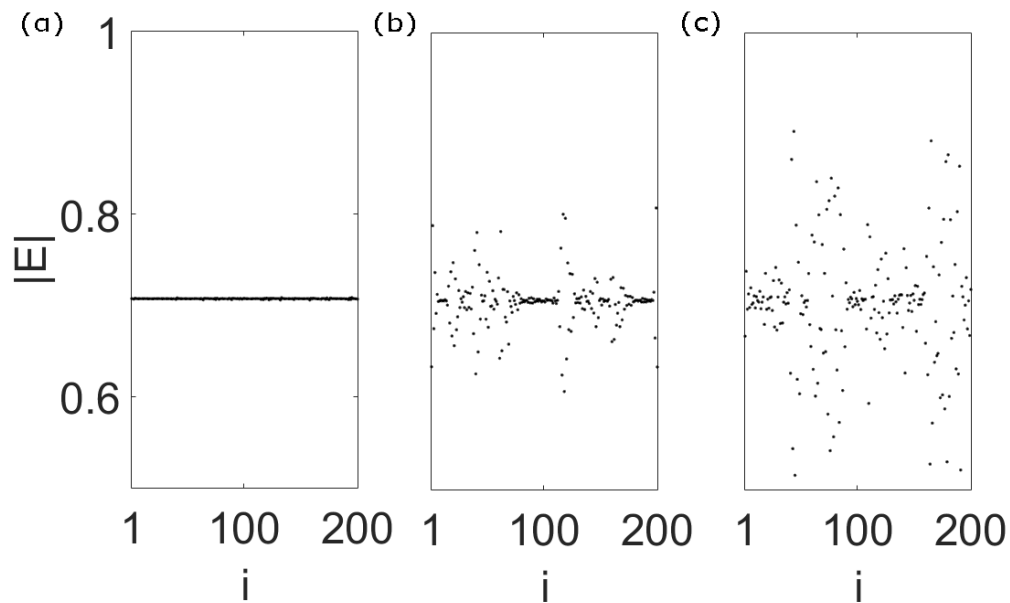


FIGURE 3.6: Snapshots of the amplitude of the electric field for different coupling strengths as in Fig.3.5 (b) with random distribution of detunings and standard deviation equal to $\omega_j/2\Omega_r$.

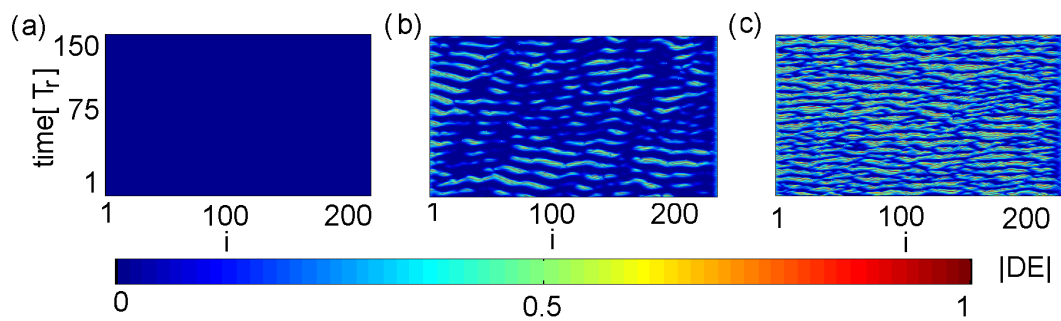


FIGURE 3.7: Spatio-temporal evolution of the local curvature for different values of the coupling strength: (a) $H = 0.008$, (b) $H = 0.014$, (c) $H = 0.026$. Other parameters as in Fig. 3.5.

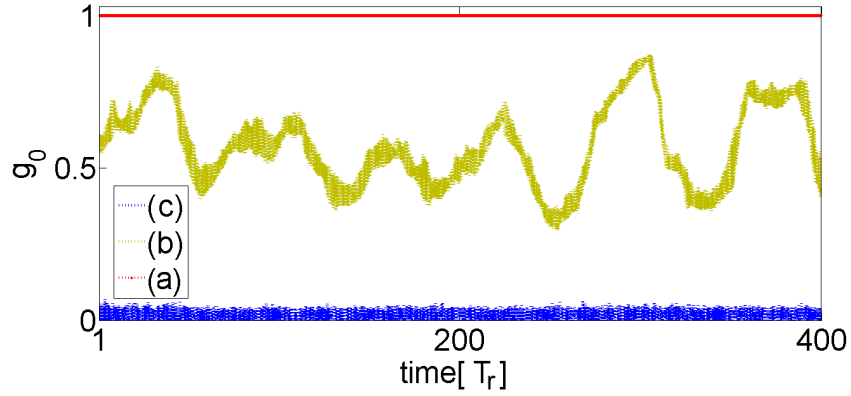


FIGURE 3.8: $g_0(t)$ over time. (a) $H = 0.008$, (b) $H = 0.014$, (c) $H = 0.026$. Other parameters as in Fig. 3.5.

chimera states [Kemeth et al., 2016]. For measuring spatial coherence, in particular, they introduced a quantity called local curvature which may be calculated at each time instance. This is done by applying the discrete Laplacian DE on the spatial data of the amplitude of the electric field:

$$DE_j(t) = |E|_{j+1}(t) - 2|E|_j(t) + |E|_{j-1}(t), \quad j = 1 \dots M. \quad (3.18)$$

In the synchronization regime the local curvature is close to zero while in the asynchronous regime it is finite and fluctuating. Therefore, if g is the normalized probability density function of $|DE|$, $g(|DE| = 0)$ measures the relative size of spatially coherent regions in each temporal realization. For a fully synchronized system $g(|DE| = 0) = 1$, while for a totally incoherent system it holds that $g(|DE| = 0) = 0$. A value between 0 and 1 of $g(|DE| = 0)$ indicates coexistence of synchronous and asynchronous lasers.

The quantity g is time-dependent. The definition of spatial synchronous and asynchronous has to be compared to the maximal curvature in each system. Thus, the characterization of coherence and incoherence depends on the individual system. Hence, in order to characterize a system as coherent or incoherent, we have to peak a threshold value. This value does not change the qualitative outcome. We have found out that if the absolute local curvature is less than five percent of the maximum curvature then the system can be characterized as coherent, and above that value as incoherent.

Complementary to the local curvature we also calculate the spatial extent occupied by the coherent lasers which is given by the following integral:

$$g_0(t) = \int_0^\delta g(t, |DE|) d|DE|, \quad (3.19)$$

where δ is a threshold value distinguishing between coherence and incoherence which is related to the maximum curvature and for our system is equal to $\delta = 0.05$. We will apply these measures in order to classify the observed patterns and we will discuss their dependence on the coupling strength H and the detuning parameter Δ .

3.6 Optical frequency detuning and chimera states

By the previous measures we are now in position to characterise the behavior of the system. Moreover, with the previous distribution, the differences of the detuning have a simple form: $|\Delta\omega_{j+1}/\Omega_r| = |\Delta\omega_{j-1}/\Omega_r| = \Delta$ [Oliva et al., 2001]. Additionally, we redefine $\frac{\eta}{\Omega_r}$ as H .

We start by Fig. 3.7 which shows the spatio-temporal evolution of the local curvature corresponding to the states of Fig. 3.5. In the fully synchronized case the local curvature is equal to zero (Fig. 3.7 (a)). In Fig. 3.7 (b) we have the case of an amplitude-chimera state. We see that this is not a stationary pattern since the local curvature oscillates in time. The fully incoherent states is shown in Fig. 3.7 (c), where the local curvature attains higher values.

In Fig. 3.8, the time evolution $g_0(t)$ for all three cases of Fig. 3.7 is plotted. We see that for the case of Fig. 3.7 (b) g_0 oscillates in an irregular manner, and therefore the corresponding amplitude chimera states are turbulent according to the classification of [Kemeth et al., 2016]. The other two curves (a) and (c) refer to full synchronization and full incoherence, respectively.

Apart from the detuning, the coupling strength has also an effect on the synchronization patterns observed in our system. In Fig. 3.9 the temporal mean of $g_0(t)$ (averaged over $400T_r$) is plotted in the (H, Δ) parameter space. The initial conditions of the phases are randomly distributed between $-\pi$ and π , while for the electric field amplitudes and the population inversions they are chosen identical for all lasers: $E_j = \sqrt{0.5}$, $N_j = 0$. The labels

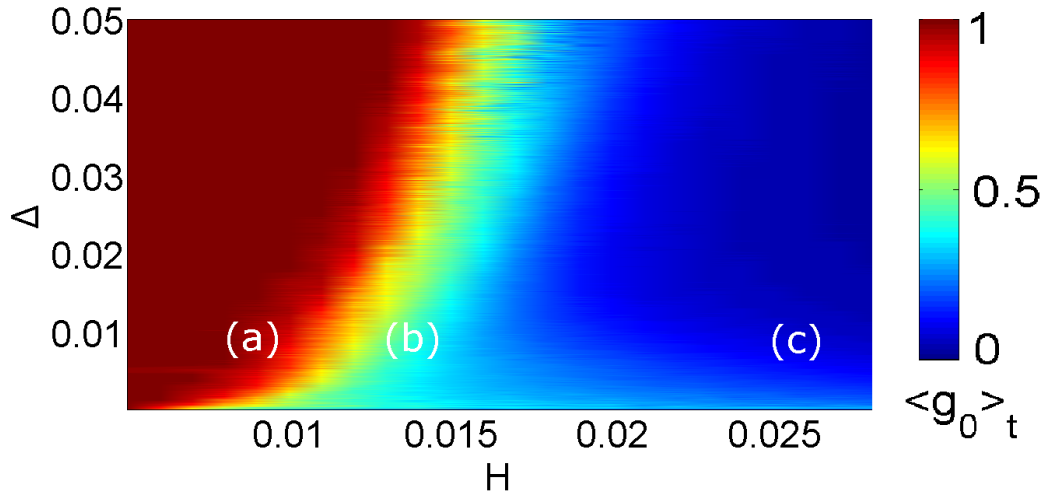


FIGURE 3.9: Dependence of the temporal mean $\langle g_0 \rangle_t$ on parameters H and Δ . Points (a) ($H = 0.008, \Delta = 0.01$), (b) ($H = 0.014, \Delta = 0.01$), and (c) ($H = 0.026, \Delta = 0.01$), correspond to Figs. 3.7(a-c). The boundary between full synchronization (red) and full desynchronization (blue) marks the regions where turbulent chimeras emerge. Other parameters as in Fig. 3.5.

(a), (b) and (c) mark the coordinates corresponding to Figs. 3.7 (a), 3.7 (b) and 3.7 (c), respectively. It is clear, that the parameter space is separated in two main domains, one of $\langle g_0 \rangle_t$ values close to unity which corresponds to full coherence and contains point (a), and one of $\langle g_0 \rangle_t$ values tending to zero which corresponds to full incoherence and contains point (c). On the boundary between these two areas, lies a small region where the amplitude chimeras arise. Note that, due to multistability, the mapping of the dynamical patterns may slightly change with different choice of initial conditions. The qualitative result, however, will be the same. For example, in Fig. 3.10 (a), we plot $\langle g_0 \rangle_t$ for a system with all initial phases randomly distributed but fixed, except those of laser 50 and 150, which we vary from 0 to 2π . Clearly, the exact values of $\langle g_0 \rangle_t$ change but remain within the range allowing for chimera states.

Finally, the question of system size is addressed. In our simulations we observe that the behavior of the system does not change significantly when increasing M from 200 to 1000. This is illustrated in Fig. 3.10 (b). After $M > 200$ the temporal mean $\langle g_0 \rangle_t$ remains constant in time. From this fact we can conclude that, for an appropriately large system, the formation of chimera states is size-independent.

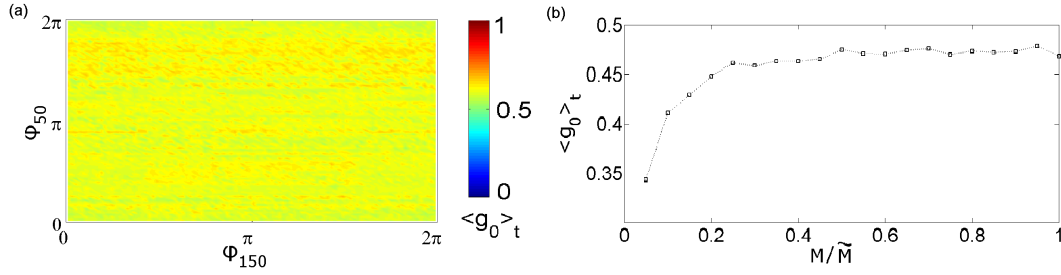


FIGURE 3.10: (a) The temporal mean $\langle g_0 \rangle_t$ as a function of the system size normalized to $\tilde{M} = 1000$. (b) (ϕ_{50}, ϕ_{150}) -projection. Initial phases for all lasers are random and fixed while ϕ_{50} and ϕ_{150} are varied. The color bar shows the value of the temporal mean $\langle g_0 \rangle_t$. Parameters: $H = 0.014$, $\Delta = 0.01$, $T\Omega_r = 20$, $p = 0.5$, $\frac{1}{\Omega_r} = 20$ and $a = 5$. Other parameters as in Fig. 3.5.

3.7 Conclusions

In conclusion, we have found amplitude chimera states in a large network of semiconductor lasers by properly modifying the optical frequency detuning. Local coupling is sufficient to generate these states even for large noise in detunings distribution compared to detuning itself. By using suitable classification measures we have quantified the observed dynamics. Due to the system's multistability, even a slight change in the initial conditions may produce different values for these measures. However, the range of the obtained values ensures the existence of chimeras, the nature of which is turbulent. The system size also has an effect on the calculated values, which saturate for arrays with more than 200 emitters. A systematic study in the optical frequency detuning and coupling strength parameter space, shows that the region of chimera states lies between full synchronization and desynchronization. For future studies it would be worthwhile to explore the effects introduced by noise as well as the laser pump power which is the most conveniently accessible control parameter in chip scale diode systems. Such investigations may have multiple technological applications regarding next generation photonic emitters that provide on demand diverse states like turbulent chimeras.

Chapter 4

Multi-clustered chimeras in large semiconductor laser arrays with nonlocal interactions

4.1 Introduction

Most of studies in Coupled lasers have been concerned with semiconductor laser arrays. They have been demonstrated as sources that can produce high output power in a spatially coherent beam. Coupling between lasers may arise due to the overlap of the electric fields from each laser waveguide or due to the presence of an external cavity [Kozyreff et al., 2001; Böhm et al., 2015]. In the latter case, a time delay is required for the mathematical modelling of the system.

In this Chapter we will deal with the Lang-Kobayashi model [Lang et al., 1980], which describes a semiconductor laser in the presence of a self-feedback interaction as we introduced it in the first Chapter. This model has become very popular and is based on the well known from the previous chapters, rate equation model. By including variables like the carrier inversion n and the complex electric field X , we have the description of the slowly varying envelope of the field in the form,

$$\frac{dX}{dt} = (1 + ia)(G - \gamma)X + ke^{-i\omega_0\tau_{ec}}X(t - \tau_{ec}) \quad (4.1)$$

$$\frac{dG}{dt} = \frac{I}{q} - \gamma_e G - G|X|^2 \quad (4.2)$$

where I is the pump current, q the electron charge, γ the photon decay rate, γ_e the carrier decay rate, k the feedback rate, τ_{ec} the round trip in the external cavity, a denotes the linewidth enhancement factor and ω_0 is the frequency of the laser without feedback.

In the case where $\omega_0 \gg \tau_{ec}$ and τ_{ec} very small, we can neglect the denominator of τ_{ec} by replacing $\omega_0\tau_{ec} = 2C_p$ where C_p is now a constant parameter. This means that, since ω_0 is very large, slight changes in the delay time change only the phase without changing the delayed term of the slowly varying envelope X . The gain G is a function of n and X and for this function different forms can be used to model the laser. A common form is a gain which is linear in n and saturates for large X ,

$$G(X, n) = g \frac{n - n_T}{1 + \epsilon|X|^2} \quad (4.3)$$

where g is the differential gain, n_T the carrier number at transparency and ϵ the gain saturation coefficient. For a dimensionless form we introduce a dimensionless time $s = t/t_c$ and dimensionless variables $X = X_c\mathcal{E}(t/t_c)$ and $n(t) = 2n_cN(t/t_c) + n_c^0$. The values of the characteristic factors t_c , X_c and n_c will be determined. The including of a constant shift n_0 has been done so that N becomes zero at the laser threshold where N is the excess carrier density or inversion. This allows sometimes for further simplifications. With this transformation we get:

$$\begin{aligned} \frac{d\mathcal{E}(s)}{ds} &= \frac{1}{2}(1 + ia) \left[t_c g 2n_c \frac{N_c + (n_c^0 - n_T)/2n_c}{1 + |X_c|^2 |\mathcal{E}|^2} - \gamma t_c \right] + k t_c e^{-i2C_p} \mathcal{E}(s - \tau_{ec}/t_c) \\ \frac{1}{\gamma_e t_c} \frac{dN(s)}{ds} &= \frac{I}{2qn_c\gamma_e} - \frac{n_c^0}{2n_c} - N(s) - \frac{g}{\gamma_e} |X|^2 \frac{2N_c + (n_c^0 - n_T)/2n_c}{1 + |X|^2 |\mathcal{E}(s)|^2} |\mathcal{E}(s)|^2 \end{aligned} \quad (4.4)$$

Then, we require that $t_c g 2n_c = (n_c^0 - n_T)/2n_c = \gamma t_c = g|X|^2/\gamma_e = 1$. This gives the final dimensionless equations,

$$\frac{d\mathcal{E}}{dt} = (1 + ia)\mathcal{E}N + ke^{-i2C_p}\mathcal{E}(t - \tau) \quad (4.5)$$

$$\frac{dN}{dt} = \frac{1}{T} \left(p - N - (1 + 2N)|\mathcal{E}|^2 \right) \quad (4.6)$$

where T is the time-scale ratio of the carrier lifetime and the photon lifetime and p is the reduced excess injection current.

Time delay comes due to the fact that the process is not instantaneous, but take place in a finite time. Many physical processes like production, conduction, transmission and diffusion can be described with a constant time delay parameter. Moreover, in medicine, the control of physiological systems (heart rate, blood pressure, motor activity) is performed by negative feedback loops that are in general delayed.

Apart from the good agreement with several experimental results, the Lang-Kobayashi model has some limitations. First of all the external cavity length, needs to be longer than the laser resonator driving to experimental limitations. Secondly, the laser beam needs to operate close to a single-mode frequency, something far from reality. Moreover, the slowly varying envelope of the electric field has to change almost adiabatically during the traveling time in the external cavity and this can be achieved only for small feedback strength. Finally, the gain part in the laser must come only from the active medium and not by the feedback. This means that the gain saturation ϵ is zero. This limit is valid when the laser is working close to threshold and the output intensity is not too large. For a strong feedback or, in the case of many lasers for strong coupling, the model fails.

The dynamical expression of a semiconductor laser with optical feedback has a large variety in output. If we assume that a laser emits a continuous-wave (cw), the possibilities in the presence of the external cavity are three: (a) For small feedback strength the behavior will not change giving again a continuous-wave. The situation will be different by increasing the coupling strength and achieving the regime of external cavity modes (ECM). There, the laser intensity will still be constant, emitting continuously but the phase of the complex electric field will now start to rotate. (b) By increasing further the feedback strength the laser eventually undergoes a Hopf bifurcation where a stable limit cycle is born. This behavior corresponds to intensity

pulsations. (c) Finally, after the Hopf bifurcation, through a series of period doubling bifurcations, the system enters a chaotic regime where the prediction is hopeless.

In general, delay-differential equations (DDEs) like the Lang-Kobayashi model, with constant time delay are being used to model various phenomena in the physical sciences. For such equations the value of the derivative at any time depends on the solution at a previous τ time. Although the techniques for solving are in general similar with those for ordinary differential equations, they differ in some significant ways. A first important difference is that for DDEs we must specify the initial condition values not just at the initial point $t = 0$ but also for the whole interval $[-\tau, 0]$. Another important difference is that the solution of DDEs normally present a discontinuity in the first derivative at the initial point and this discontinuity causes trouble even for numerical methods. These discontinuities propagate: If the first derivative is discontinuous at $t = 0$, then the second derivative will be discontinuous at $t = \tau$, the third derivative at $t = 2\tau$, and so on. But the most important property is that a single delay-differential equation is capable of producing periodic motion, in contrast to a single ordinary differential equation. This is because the single DDE is not 1-dimensional, but is actually infinite dimensional.

Returning to our model, most works on laser arrays consider either global coupling, where each laser interacts with the whole system [Silber et al., 1993], or local coupling, where each laser interacts with its nearest neighbors [Blackbeard et al., 2014; Winful et al., 1990]. The main property of those systems is that although the emission from the individual elements is often unstable and even chaotic [Wang et al., 1988], the total light output from the semiconductor array can be stable.

In recent years however, as we have mentioned, semiconductor laser networks have been studied in terms of a peculiar form of synchronization called chimera states. Since the first discovery of chimeras for symmetrically coupled Kuramoto oscillators [Kuramoto et al., 2002], this counter-intuitive symmetry breaking phenomenon of partially coherent and partially incoherent behavior, in laser systems were first reported both theoretically and experimentally in a virtual space-time representation of a single laser system subject to long delayed feedback [Larger et al., 2015].

Small networks of globally delay-coupled lasers class B have also been

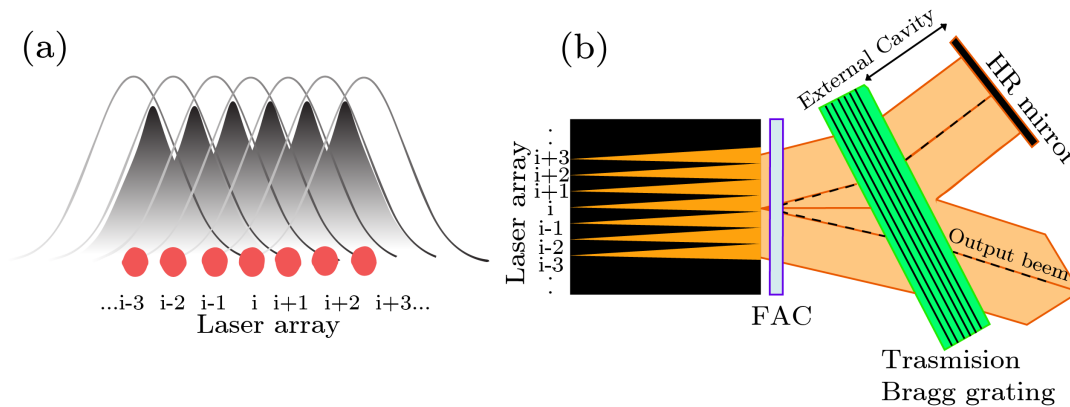


FIGURE 4.1: Conceptual model of (a) the overlap of the electric fields in nonlocally coupled waveguide lasers, (b) a laser array coupled by a common highly-reflective (HR) mirror via an external cavity. (FAC stands for Fast-Axis Collimating lens).

studied and chimera states were found for both small and large delays [Böhm et al., 2015; Röhm et al., 2016]. In chimera states coherence and incoherence patterns emerge not only in the phase but also in the amplitude of the electric field and in inversion of the population of the active medium. Furthermore, the dynamics of these two synchronous and asynchronous parts is chaotic.

The experimental realization of laser arrays is challenging, but these devices have significant technological advantages: By achieving phase locking of the individual lasers we obtain a coherent and high-power optical source. In [Nixon et al., 2012] synchronization phenomena were studied in large networks with both homogeneous and heterogeneous coupling delay times. Moreover, in [Nixon et al., 2013] a new experimental approach to observe large-scale geometric frustration with 1500, both nonlocally and locally, coupled lasers was presented. In the present work, we will focus on the intermediate case, i.e., nonlocal coupling. In laser networks this kind of coupling has never been attempted before and we aim to fill this gap. In this Chapter we use nonlocal coupling, where the crucial parameters for the observed dynamics are the strength, the phase and the range of the coupling. Our focus, in particular, is to identify the parameter regions where chimera states or other phenomena emerge and subsequently characterize them following a recently proposed classification scheme [Kemeth et al., 2016].

4.2 The Model

In the present analysis, we consider a ring of $M = 200$ semiconductor lasers of class B. Each node j is symmetrically coupled with the same strength to its R neighbors on either side (nonlocal coupling). The evolution of the slowly varying complex amplitudes $\mathcal{E}_j = E_j \exp\{i\phi_j\}$ (where E_j is the amplitude and ϕ_j the phase of the electric field) and the corresponding population inversions N_j are given by,

$$\frac{d\mathcal{E}_j}{dt} = (1 + ia)\mathcal{E}_j N_j + \frac{ke^{-i2C_p}}{2R} \sum_{l=j-R}^{j+R} \mathcal{E}_l(t - \tau) \quad (4.7a)$$

$$\frac{dN_j}{dt} = \frac{1}{T} \left(p - N_j - (1 + 2N_j)|\mathcal{E}_j|^2 \right), \quad j = 1, \dots, M, \quad (4.7b)$$

where all indices has to be taken modulo M . Lasers are pumped electrically with the excess pump rate $p = 0.23$ [Böhm et al., 2015]. We consider $a = 2.5$, which is a typical value for semiconductor lasers. The coupling strength k , the phase C_p and the number of coupled neighbors on either side R , are the control parameters that are used to tune the collective dynamics of the system.

Physically, nonlocal coupling arises due to the overlap of the electric fields within a range of R neighbor waveguides of lasers (see Fig. 4.1 (a)). In this case, a portion of the electric field from one laser extends into the active region of its $2R$ neighboring lasers. The strength of this field extension decreases in space but for simplicity we assume a uniform coupling k in every active region of $2R$ lasers.

Equations 4.7 are numerically integrated using a fourth-order Runge-Kutta algorithm with a fixed time step and periodic boundary conditions. For the initial conditions, the phases of the individual lasers are randomly distributed along the complex unit circle while amplitudes and inversions are chosen identical for all lasers $E_j(t = 0) = \sqrt{p}$, $N_j(t = 0) = 0$. Moreover, the well known period $T_r = 2\pi/\Omega$ of the individual laser relaxation oscillation frequency $\Omega = \sqrt{2p/T}$ will set the time scale of the system. For the parameters considered in this work, $T_r \simeq 183$.

As we mentioned before, for small feedback strength the behavior will not change significantly. In Fig.4.2 we can see the maxima of the intensity ($|E|^2$) of the electric field for a semiconductor laser with feedback versus the time delay τ . For small τ the intensity remains constant. Only when τ reaches values above 10 a Hopf bifurcations takes place leading to periodic behavior. For larger delay time the system goes to chaos through a cascade of period doubling. This chaotic regime is interrupted by periodic windows and for a very large delay even those windows disappear. The same behavior for small τ can be shown for two coupled semiconductors lasers with feedback. Figure. 4.3 displays the bifurcation diagram of the maxima of the first coupled laser intensity as a function of τ . The influence of the delay time for small values is again negligible. There is a constant output (CW) and after a significant increase of τ there is a transition to other regimes with quasiperiodic chaotic oscillations. As expected, this diagram agree with the above ones computed for a single laser with feedback.

The above analysis motivate us to neglect the delay term from our system. More precisely, in our study, we consider the limit of short coupling delay τ , that is, much smaller than the relaxation oscillation period T_r . In what follows, the results we present are very similar to the case of $\tau = 1$, therefore, we have chosen to set the delay to zero. With this simplification, the equations of the system have the form:

$$\frac{d\mathcal{E}_j}{dt} = (1 + ia)\mathcal{E}_j N_j + \frac{ke^{-i2C_p}}{2R} \sum_{l=j-R}^{j+R} \mathcal{E}_l \quad (4.8a)$$

$$\frac{dN_j}{dt} = \frac{1}{T} \left(p - N_j - (1 + 2N_j)|\mathcal{E}_j|^2 \right), \quad j = 1, \dots, M, \quad (4.8b)$$

The complex coupling coefficient models the important effect of a phase shift introduced as the electric field of one laser couples into another [Katz et al., 1984]. Equations 4.8 are a reduced form of the Lang-Kobayashi model in the limit where the delay of the external cavity tends to zero [Böhm et al., 2015]. By replacing $k \cos(2C_p) = k_I$, $k \sin(2C_p) = k_R$ and $R = M/2$ or $R = 1$ we can obtain the model that describes the interaction of each field of semiconductor lasers in an array of waveguides where the coupling strength is $iK = i(k_R + ik_I)$, [Silber et al., 1993].

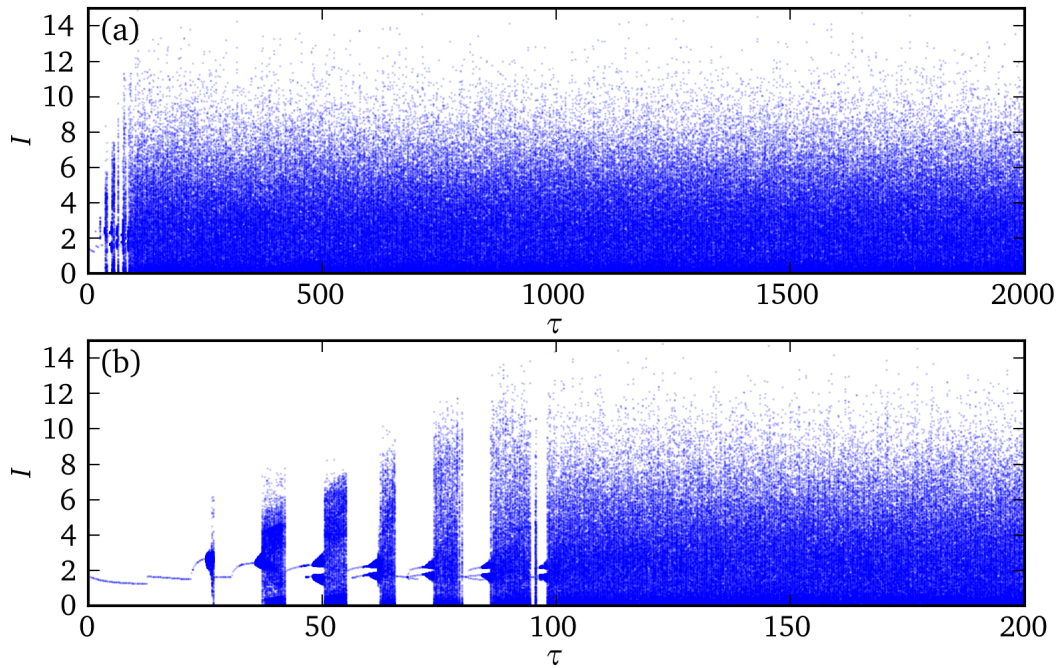


FIGURE 4.2: (a) The maxima of intensity in dependence on the delay time τ for a semiconductor laser with optical feedback. Parameters: $p = 1$, $a = 4$, $T = 200$, and $k = 0.12$. (b) Blow-up. (Redrawing from P.h.d thesis [Dahms, 2011], Fig.2.5)

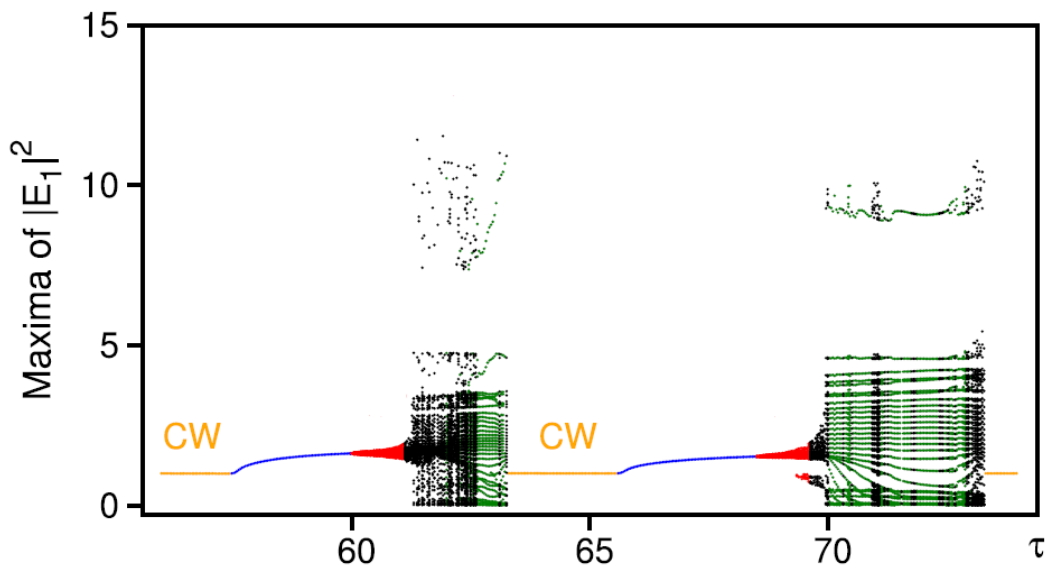


FIGURE 4.3: Bifurcation diagrams of intensity for the first laser as a function of τ . Parameters: $p = 1.155$, $a = 5$, $T = 1710$, and $k = 0.135$. (Redrawing from [Junges et al., 2015], Fig.3)

The scheme corresponding to this form of equations can be achieved by replacing all waveguides by a single external cavity where the length of it or the delay tends to zero (see Fig. 4.1 (b)). In that case the converging lens

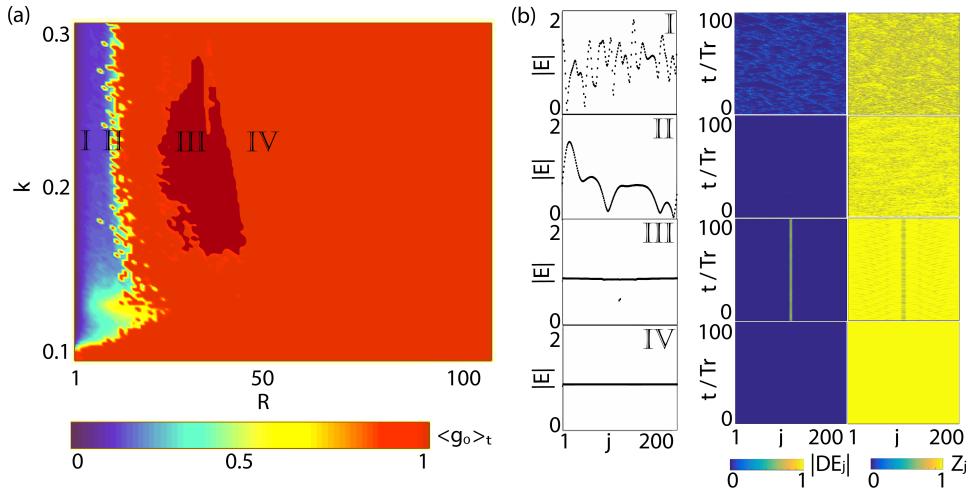


FIGURE 4.4: (a): Dependence of the temporal mean $\langle g_0(t) \rangle_t$ on parameters k and R . (b): Snapshot of the amplitude of the electric field (left), spatio-temporal evolution of the local curvature (middle), and the local order parameter (right) for fixed $k = 0.21$ and four different coupling ranges: (I) $R = 2$, (II) $R = 9$, (III) $R = 29$, and (IV) $R = 50$. Other parameters: $T = 392$, $p = 0.23$, $a = 2.5$, and $C_p = 0$.

coupler for all the lasers inside the cavity cannot converge all the M beams of light in one beam and so a nonlocal coupling is a more realistic approach than an all-to-all coupling.

In order now to understand the effect of all three control parameters, namely the coupling strength k , the coupling range R and the coupling phase C_p , we split the problem into two parts: In the first part, the coupling phase is set to zero and the co-action of the coupling strength and range is studied. In section 4.3, the coupling phase is also considered and we will show that more complex phenomena like chimera states emerge.

For proper measures, first, by using polar coordinates the characterization of the phase synchronization of our system can be done through the Kuramoto local order parameter [Omelchenko et al., 2013]:

$$Z_j = \left| \frac{1}{2\zeta} \sum_{|l-j| \leq \zeta} e^{i\phi_l} \right|. \quad (4.9)$$

We use a spatial average with a window size of $\zeta = 3$ elements. A Z_j value close to unity indicates that the j -th laser belongs to the coherent regime, whereas Z_j is closer to 0 in the incoherent part. This quantity can measure

only the phase coherence and gives no information about the amplitude synchronization of the electric field.

For the latter, we will use the classification scheme presented in Chapter 3 [Kemeth et al., 2016] for spatial coherence. In particular, we will calculate the *local curvature* at each time instance, by applying the absolute value of the discrete Laplacian $|DE|$. As we have shown, in the synchronization regime the local curvature is close to zero while in the asynchronous regime it is finite and fluctuating. Moreover, the normalized probability density function of $|DE|$, for a fully synchronized system $g(|DE| = 0) = 1$, while for a totally incoherent system it holds that $g(|DE| = 0) = 0$. A value between 0 and 1 of $g(|DE| = 0)$ indicates coexistence of synchronous and asynchronous lasers.

4.3 Collective dynamics

In panel (a) of Fig. 4.4, the temporal mean of $g_0(t)$, averaged over $100T_r$, is plotted in the (R, k) -parameter space. There are four distinct regions: The blue area corresponds to the unsynchronized region, where $g_0(t)$ is close to zero and is marked by the letter I, and the red region, marked by the letter IV, refers to a stationary state where all lasers enter a fixed point and therefore $g_0(t)$ is close to unity. Apart from those two well defined regions, there exist two more interesting ones for intermediate values of $g_0(t)$. The first one lies on the border between the incoherent and the stationary state and is marked by the letter II, while the second region exists within the stationary area and is marked by the letter III. Figure 4.4 (b) shows the corresponding snapshot representations of the amplitude of the electric field (left), the spatio-temporal evolution of the local curvature (middle), and that of the local order parameter (right). Note that the local curvature has been normalized to its maximum value [Kemeth et al., 2016].

Moving from point I to IV, the system goes from the incoherent state to the stationary one through a wave-like spatial structure (point II) and an almost fully stationary state (point III). In the incoherent state the lasers are desynchronized both in amplitude and in phase, which is depicted in the local curvature and the local order parameter. With increase of the coupling range R , the temporal oscillations of the lasers tend to become closer in amplitude. This is reflected in the smooth wave-like structure of the amplitude of the

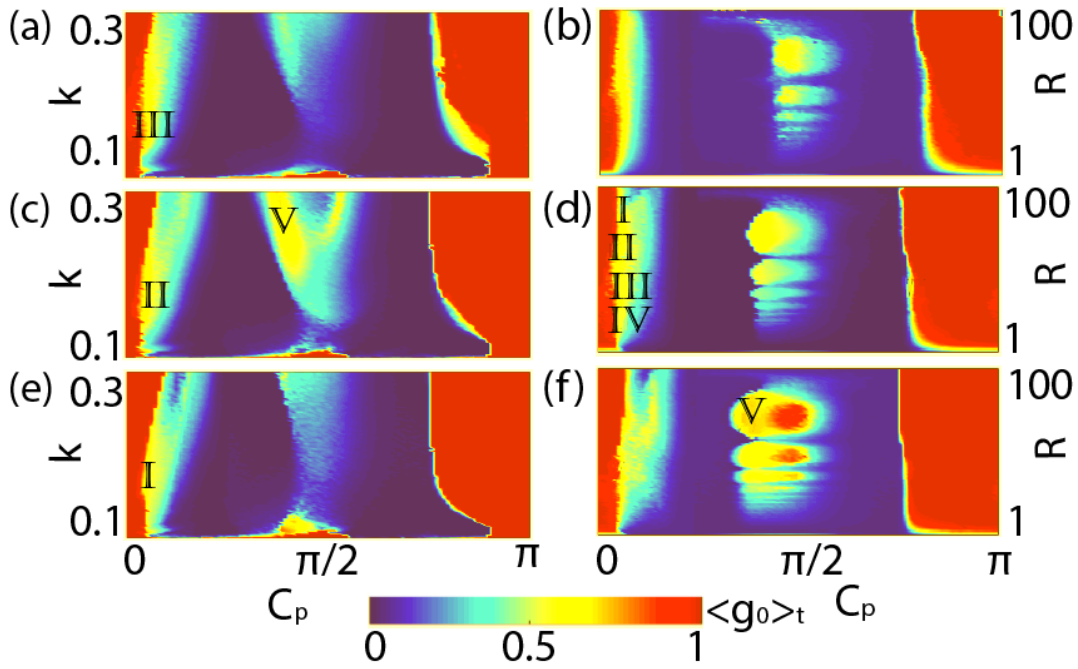


FIGURE 4.5: Dependence of the temporal mean $\langle g_0(t) \rangle_t$ on parameters k and C_p for different values of nonlocal coupling range: (a) $R = 40$, (c) $R = 64$, and (e) $R = 88$. Dependence on parameters R and C_p of the temporal mean $\langle g_0(t) \rangle_t$ for different values of the coupling strength: (b) $k = 0.075$, (d) $k = 0.15$, and (f) $k = 0.225$. Other parameters: $T = 392$, $p = 0.23$, and $a = 2.5$.

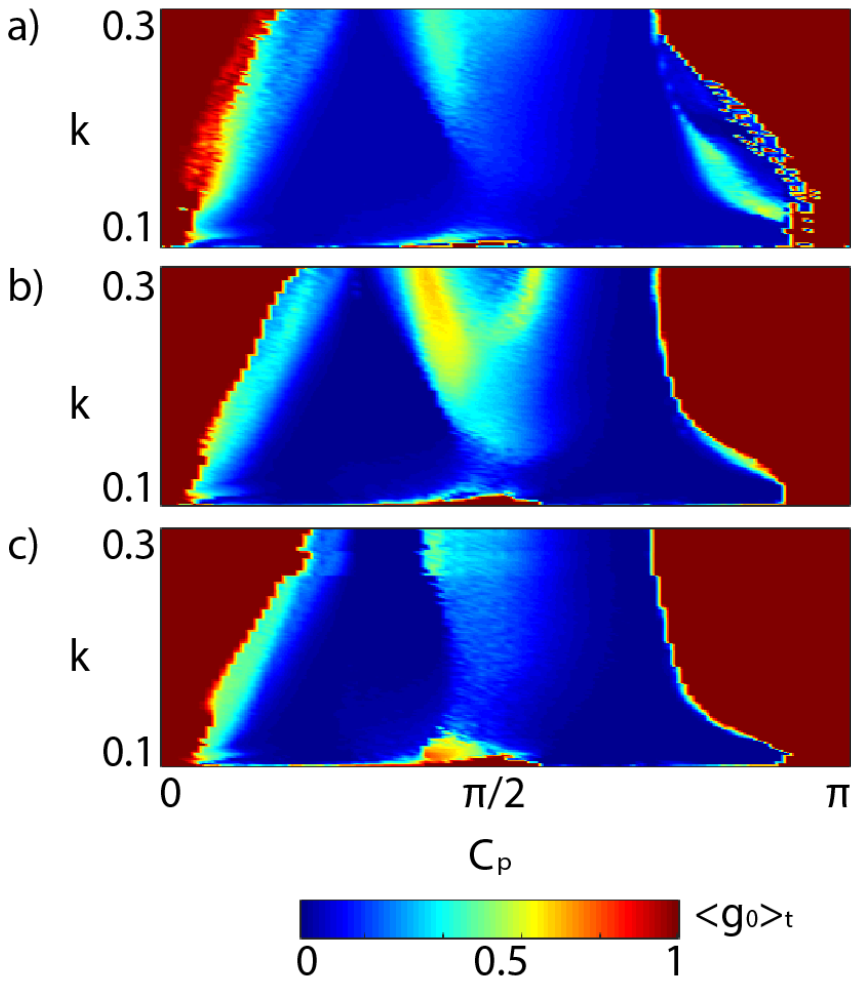


FIGURE 4.6: Dependence of the temporal mean $\langle g_0 \rangle_t$ on parameters k and C_p for different values of nonlocal coupling range: (a) $R = 40$, (b) $R = 64$, and (c) $R = 88$ for $\tau = 1$ with other parameters as in Fig.4.5.

electric fields and the discrete Laplacian which holds a value close to zero. The corresponding phase oscillations are less coherent and this is evident by the blue areas in the order parameter spatio-temporal plot.

Before entering the fully stationary state (IV) the system undergoes another interesting region where $g_0(t)$ is close, but less than one because of a deviation from the stationary state of two lasers (left panel of III), which holds for both the amplitude (middle) and the phase (right). In coupled systems, the phenomenon where one or more oscillators exhibit large amplitude oscillations whereas the rest are stationary, is called localized breather and has been intensively investigated in the past [MacKay et al., 1994; Chen et al., 1996].

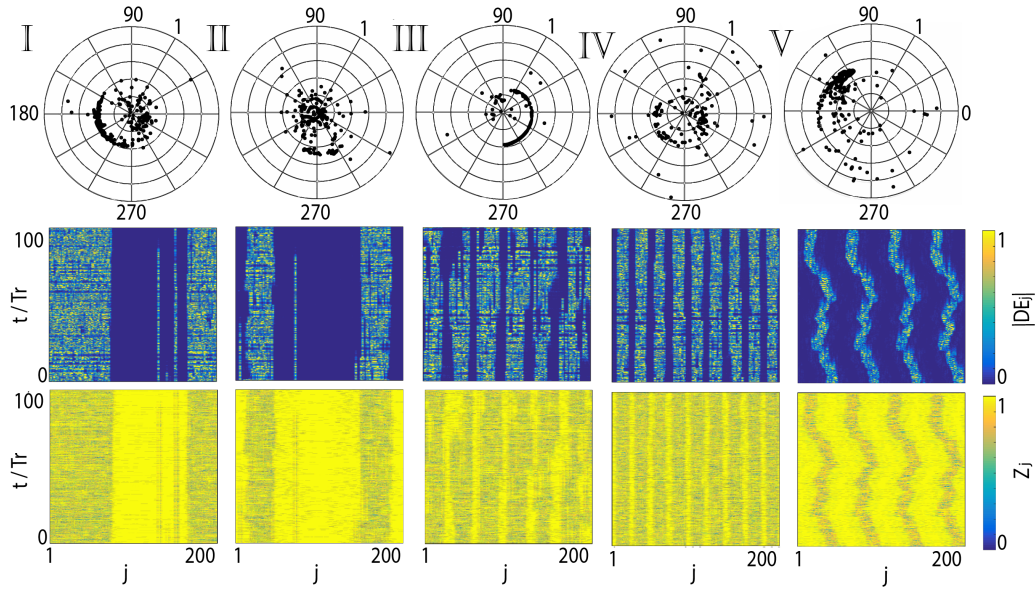


FIGURE 4.7: The electric field in the complex unit circle (top), spatio-temporal evolution of the local curvature (middle), and spatio-temporal evolution of the local order parameter (bottom) for different coupling ranges and phases: (I) $R = 88, C_p = 0.1\pi, k = 0.15$ (II) $R = 64, C_p = 0.06\pi, k = 0.15$, (III) $R = 40, C_p = 0.1\pi, k = 0.15$, (IV) $R = 27, C_p = 0.1\pi, k = 0.15$, and (V) $R = 64, C_p = 0.4\pi, k = 0.225$. Other parameters: $T = 392, p = 0.23$, and $a = 2.5$.

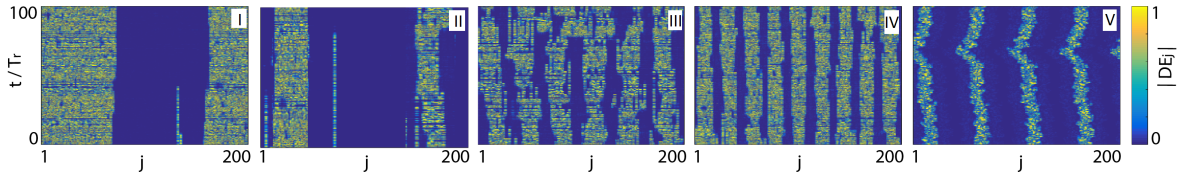


FIGURE 4.8: The spatio-temporal evolution of the local curvature for different coupling ranges and phases as in Fig.4.7 for $\tau = 1$.

For finite coupling phase C_p , the situation is much more complicated. By plotting the temporal mean of $g_0(t)$ in the (C_p, k) -plane (Fig. 4.5 (a), (c), and (e)) as well as in the (C_p, R) -plane (Fig. 4.5 (b), (d), and (f)) for various values of the coupling strength k and the coupling range R , we can identify the existence of many patterns, among which chimera states, which we have marked with roman letters. Each chimera state is characterized by its multiplicity, i.e., the number of the (in)coherent regions also known as number of chimera clusters. Single chimeras (I), as well as chimeras with two (II), six (III) and nine heads (IV) are observed. Moreover, localized oscillations and waves similar to those of Fig. 4.4 are also found (not shown). Finally, "turbulent" chimeras where the position of the (in)coherent regions changes in time

and $g_0(t)$ oscillates irregularly complete the picture of the observed patterns (V).

More specifically, for nonlocal range coupling $R > 10$ and coupling strength $k > 0.05$, we can distinguish different regions in terms of the coupling phase value. Below those two values the interaction is so weak that each laser behaves like an uncoupled one (see Fig. 4.5, lower left corners of all panels). Around the region $C_p \approx 0$ and the region $C_p \approx \pi$ the case of full synchronization is most prominent, where $\mathcal{E}_i = \mathcal{E}_j$ holds for all lasers. The opposite situation of full asynchrony where both amplitude and phase exhibit incoherent behaviour appears around the regions $C_p \approx \pi/4$ and $C_p \approx 3\pi/4$. On the boundary between full synchronization and asynchrony lies a small area where the chimeras arise.

Figure 4.7 shows typical snapshots of multi-clustered chimera states of the electric field in the complex unit circle (top panel), the spatio-temporal evolution of the local curvature (middle panel) and the spatio-temporal evolution of the local order parameter (bottom panel) for points I-IV. We observe that the decrease of R yields additional chimera heads both in amplitude and in phase. Moreover, around the region where $C_p \approx \pi/2$ turbulent chimeras appear (Fig. 4.7, V).

Finally, the investigation of the system behavior in the presence of a finite but small delay time has been performed. In Fig. 4.6 we have plotted the temporal mean of $g_0(t)$ in the (C_p, k) -plane with $\tau = 1$, for the same values of the coupling range R as in Fig. 4.5. The similarities with the system in the absence of the delay time are clear. More precisely, Fig. 4.8 depicts the spatio-temporal evolution of the local curvature of the amplitude of the electric field where chimera states emerge for delay ($\tau = 1$) and different coupling ranges. It is evident, that qualitatively, these results are in good agreement with the zero delay case (see middle panel of Fig. 4.7). Since the above results are very similar with or without delay, the choice to set the delay to zero is a reasonable limit.

4.4 Conclusions

In conclusion, multi-clustered chimera states have been obtained and characterized in large arrays of semiconductor class B lasers with nonlocal interactions. The observed chimeras display the coherence and incoherence patterns in both the amplitude and phase of the electric field and can be both stationary or "turbulent", where the size and position of the (in)coherent clusters vary in time. In addition, other spatiotemporal dynamics including wave-like spatial structures and spatially localized oscillations (breathers) are possible. The crucial parameters for the collective behavior are the complex coupling strength and the nonlocal coupling range. The latter is responsible for the multiplicity of the (in)coherent domains of the obtained chimeras which has not been observed neither for local nor for global coupling. By applying recently presented measures for spatial coherence we have identified and classified the emerging dynamics in the relevant parameter spaces. Our study addresses the effect of nonlocal coupling in large laser arrays for the first time, providing a direction for various technological applications. By considering the proposed setups for the nonlocal coupling scheme, our results can prove useful for further experimental investigations. For future studies it would be worthwhile to explore the influence of noise and anisotropy in the laser pump power.

Chapter 5

Class B lasers in star networks with optoelectronic feedback

5.1 Introduction

Solid-state and semiconductor laser arrays constitute a wide family of non-linear coupled systems with complex dynamical behavior. In these systems the emission from the individual units is often unstable with large amplitude chaotic pulsations [Wang et al., 1988; Fabiny et al., 1993; Thornburg et al., 1997], however, the overall system can show synchronization and other spatiotemporal phenomena. The dynamics of semiconductor laser arrays can be studied with conventional detectors whereas streak cameras are often necessary for solid-state laser arrays. Another difference between semiconductor and solid-state lasing media is the large value of the "linewidth enhancement factor" a , being $3 \leq a \leq 5$ for semiconductor and $a = 0$ for solid-state systems. This difference makes solid-state lasers more suitable in applications where phase locking is required.

In recent years, many studies have been concerned with semiconductor lasers and the analysis of synchronization and chimera states [Winful, 1992; Böhm et al., 2015]. Here, however, we focus on solid-state laser arrays and the formation of localized stationary patterns of activity. The dynamic behavior of each laser element is bistable and the coupling between the elements is local and arises due to the overlap of the electric fields of each separated beam [Zehnlé, 2000; Fabiny et al., 1993].

The theoretical model we use is originated from numerical and experimental studies of a CO₂ laser with an intracavity electro-optic modulator that

exhibits bistability [Ye Wang et al., 1990]. Electrical feedback is frequently used in laser design to achieve stable output and to protect the laser from burnout while optical feedback has been successfully used for stabilizing the laser frequency. This model has many similarities to that obtained by semiconductor lasers with a saturable absorber inside the cavity [Yamada, 1993]. A similar problem was revisited for a Nd:YAG laser with an acousto-optic modulator [Meucci et al., 2002]. Bistability has also been found in semiconductor lasers with strong optical injection [Wieczorek et al., 2002] and in semiconductor laser diodes with saturable absorber [Dubbeldam et al., 1999].

Rich dynamical behavior has also been recently found in complex networks of coupled bistable chemical reactions [Kouvaris et al., 2012; Kouvaris et al., 2013; Kouvaris et al., 2016; Kouvaris et al., 2017]. Such networks of coupled bistable units support the spreading or the retreating of an initial activation, but more interestingly, they support the formation of localized stationary patterns dependent on the coupling strength and the degree distribution of the nodes. The current work aims at bringing those novel results from electrochemical networks into the field of laser arrays dynamics. The topological structure of the system plays essential role in the emergent dynamics. Therefore, we start our analysis by focusing on the simple case where the laser arrays form star networks where each bistable element is connected to a central one, the hub. This connectivity structure is often found in many natural or engineered systems that consist of dynamical elements interacting with each other through a common medium. It has also been used in optically coupled semiconductor lasers [Zamora-Munt et al., 2010; Bourmpos et al., 2012] where synchronization phenomena were investigated. We present an extended numerical analysis that takes advantage of the simplicity of the star network topology to determine the conditions required for the formation of localized stationary patterns.

5.2 The Model and Stability analysis

The dynamical behavior of the CO_2 laser with feedback can be described by three coupled first-order differential equations, one for the laser field (E), the second for the population inversion (G) and the last for the feedback voltage of the electro-optic modulator (V). In dimensionless form, the evolution equations have the form [Ye Wang et al., 1990],

$$\begin{aligned}
\frac{dE}{dt} &= \frac{1}{2}(G - 1 - a \sin^2(V))E \\
\frac{dG}{dt} &= \gamma(P - G - G|E|^2) \\
\frac{dV}{dt} &= \beta(B + f|E|^2 - V)
\end{aligned} \tag{5.1}$$

where γ denotes the population decay time, P denotes the pumping and a scales the maximum loss introduced by the modulator. The damping rate β of the feedback loop is normalized by the cavity decay rate. B is the bias voltage applied to the modulator amplifier and f is the scaling of the feedback gain, i.e. it measures the relation between the intensity incident on the photodiode and the voltage delivered by the differential amplifier. In general, B is the control parameter.

Positive or negative feedback depends on the relative sign of f and B . If $B > 0$, then $V > 0$ is favored in absence of feedback. As $|E| > 0$, $f > 0$ implies that the feedback increases V and the losses through $-a \sin^2(V)$ since modulators are generally operated at $V < \pi/2$. Therefore $f > 0$ implies negative feedback and $f < 0$ positive feedback.

In the case of one laser, the phase of electric field is a constant variable in time and has no role in system dynamic. Thus, we prefer to work with the amplitude of electric field without loss of generality. In this frame, Equations. 5.1 possess a zero intensity solution given by ($|E| = 0, G = P, V = B$) and a non-zero intensity solution given by,

$$\begin{aligned}
\frac{P}{1 + |E|^2} &= 1 + a \sin^2(B + f|E|^2) \\
G &= \frac{P}{1 + |E|^2} \\
V &= B + f|E|^2
\end{aligned} \tag{5.2}$$

where $|E|$ is the amplitude of electric field.

The zero intensity solution is stable if $P - 1 - a \sin^2(B) < 0$ and always unstable if $a < P - 1$. For the non-zero intensity steady state (Eq.5.2), the

characteristic equation is,

$$\lambda^3 + c_1\lambda^2 + c_2\lambda + c_3 = 0 \quad (5.3)$$

where:

$$\begin{aligned} c_1 &= \gamma(1 + |E|^2) + \beta \\ c_2 &= \gamma G|E|^2 + a|E|^2 \sin(2V)\beta f + \gamma\beta(1 + |E|^2) \\ c_3 &= \gamma\beta|E|^2 \left[G + af \sin(2V)(1 + |E|^2) \right] \end{aligned} \quad (5.4)$$

If $c_3 = 0$ then we have the condition for a saddle-node bifurcation. Hence, we find that this condition is realized either if $|E| = 0$ or if $G + af \sin(2V)(1 + |E|^2) = 0$. The first case has no interest since the amplitude of the electric field is zero (no lasing). The second case corresponds to a saddle-node bifurcation or limit point where by using Eq. 5.2 we have:

$$f = -\frac{(1 + a \sin^2(V))^2}{aP \sin(2V)} \quad (5.5)$$

A saddle-node bifurcation is the basic mechanism where two or more fixed points are created and destroyed. The normal form of a saddle-node bifurcation is: $\dot{x} = r + x^2$ where r is a parameter. When r is negative there are two fixed points ($x^* = \pm r$) where $x^* = -r$ is stable and $x^* = r$ is unstable. As r approaches the value zero, the fixed points coalesce and the new fixed point is half stable and half unstable (extremely delicate). When $r = 0$ we say that a saddle-node bifurcation occurred (see [Strogatz, 1994]).

Now, if we introduce $\lambda = i\omega$ we get the condition for a Hopf bifurcation where f now must be equal to:

$$f = -\frac{\gamma^2 P [P - 1 - a \sin^2(V) + \beta P (1 + a \sin^2(V))^{-1}] + \gamma \beta^2 P}{\beta^2 a (P - 1 - a \sin^2(V)) \sin(2V)} \quad (5.6)$$

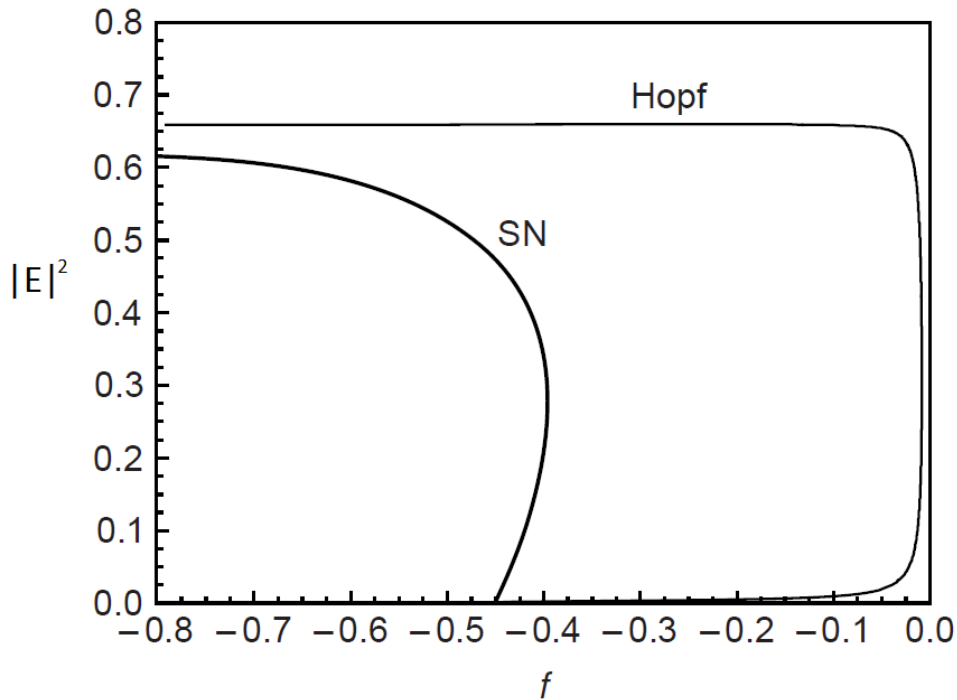


FIGURE 5.1: Saddle-node (SN) and Hopf bifurcation stability in terms of the steady state intensity $|E|^2$ and f . (redrawn from Figure 4.6 of [Erneux et al., 2010])

The Hopf stability and the saddle-node bifurcation are shown in Fig. 5.1 in terms of the steady state intensity $|E|^2$ and feedback factor f .

We illustrate the stability of these steady states by studying the bifurcation diagram in the case of high ($f = -0.6$) gain and using B as the control parameter [Ye Wang et al., 1990]. In Fig. 5.2 the system exhibits bistability (coexistence of two stable steady states) and a hysteresis cycle is observed as we increase or decrease B beyond the interval (0.35-0.40). As we progressively increase B , the transition to the zero intensity steady state does not occur at the steady state limit point but from the Hopf bifurcation branch. In the rest of our analysis we hold the bias voltage constant and equal to ($B = 0.37$). The reason for that is to build a controlled bistable system where in the presence of the coupling strength any laser to be able to achieve the passive (where $|E|^2 \approx 0$) or the active (where $|E|^2 \approx (P - 1)$) state. Moreover, the chosen $B = 0.37$ allows as to avoid transitions from the Hopf branch, something that makes the system less complex. The diagram has been determined numerically by the MatCont software.

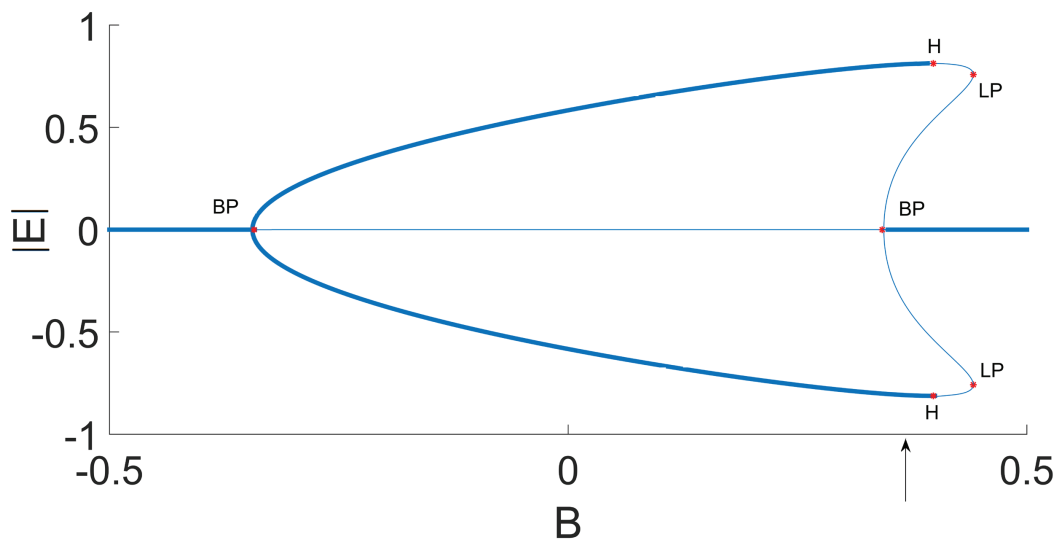


FIGURE 5.2: High-gain bifurcation diagram. The figure represents the stationary amplitude of the laser field ($|E|$) versus the bias voltage (B). The thick line marks the stable state interval. With H we denote the Hopf bifurcation point, with LP the saddle node and with BP the branch point of a pitchfork bifurcation. The constant value of B has been indicated by the arrow. Other parameters: $\gamma = 0.003125$, $P = 1.66$, $\beta = 0.0521$, $a = 5.8$, and $f = -0.6$.

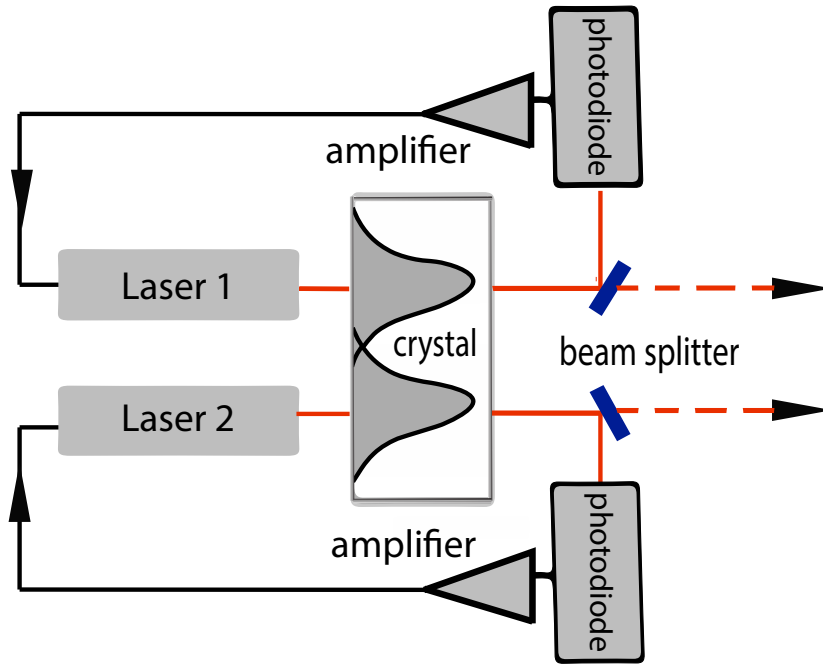


FIGURE 5.3: Schematic diagram of optoelectronic feedback of two coupled lasers. The optical power emitted by the first or the second laser is detected by a photodiode with a fixed bandwidth. The electrical output is fed back to each laser through an amplifier. The remain intensity of each laser, after the beam splitter, has been coupled by the overlap of the electric fields in a nonlinear crystal.

5.3 Two coupled lasers

With the model having been clearly defined, the next step is the contraction of two parallel waveguide of CO_2 lasers each one with a proper optoelectronic feedback (see Fig. 5.3). The mutual interaction lies on the overlap of both laser fields inside the crystal with a proper refractive index profile [Zehnlé, 2000]. The evolution equations for this coupled system have the form,

$$\begin{aligned} \frac{dE}{dt} &= \frac{E}{2}(G - 1 - a \sin^2(V)) - \eta E_H \\ \frac{dE_H}{dt} &= \frac{E_H}{2}(G_H - 1 - a \sin^2(V_H)) - \eta E \end{aligned} \quad (5.7)$$

where, with H we denote the second coupled laser. The equations for the population inversion (G and G_H) and the feedback voltage of the modulator (V and V_H) have the same form as Eq. 5.1. The parameter η is the coupling

strength between the the two lasers and in general is a complex parameter ($\eta = \eta_R + i\eta_{Im}$). The real part η_R , takes usually negative values and vanishes only when $D \simeq 2w$ where D is the distance between the two beams while w is the waist of the beam with a Gaussian portrait. Parameter η_{Im} is related to the refractive index and can be zero for a weak intensity laser beam which is the case in our model ($\eta_{Im} = 0$). Now, the phase differences between the two lasers is a time dependent variable with great importance. However, we are working in the phase locking regime which has been determined for the whole system in the last section. In this regime, for proper initial conditions and after a small time interval, the phase difference is constant (the steady state) and the dynamic of the system can be describe now, only by the amplitude of the electric field. The equilibria for this coupled system, after some algebra, has the form,

$$\begin{aligned} \frac{P}{1 + |E|^2} &= 1 + a \sin^2 \left(B + f|E|^2 \right) - 2\eta \frac{|E_H|}{|E|} \\ \frac{P}{1 + |E_H|^2} &= 1 + a \sin^2 \left(B + f|E_H|^2 \right) - 2\eta \frac{|E|}{|E_H|} \end{aligned} \quad (5.8)$$

where $|E|$ is the amplitude of the electric field.

The solution of Eq. 5.8 and the stability of Eq. 5.7 have been calculated numerically by the MatCont software using η as the control parameter. In Fig. 5.4 (a) we show the stationary amplitude of the laser field versus the coupling strength for both lasers while in Fig.5.4 (b) we show the top view of Fig. 5.4 (a). With the fine line we present the fixed points of the system and with the thick one the stable interval. With different colors we denote three dissimilar dynamical cases. In the first case (red color) the initial condition of the amplitude of the electric field for the first laser is located in the active state and for the second in the passive state. Following the same logic, in the second case (green color) we have the opposite condition where the amplitude of the electric field for the second laser is located in the active state and for the first in the passive state. Finally, in the third case (black color), the amplitude of the electric field both for the first and the second laser is located in the passive state. For clarity, we plot the stationary field both for positive and negative values of η but only the positive have physical meaning.

In the first and the second case (red and green color) the fixed points of

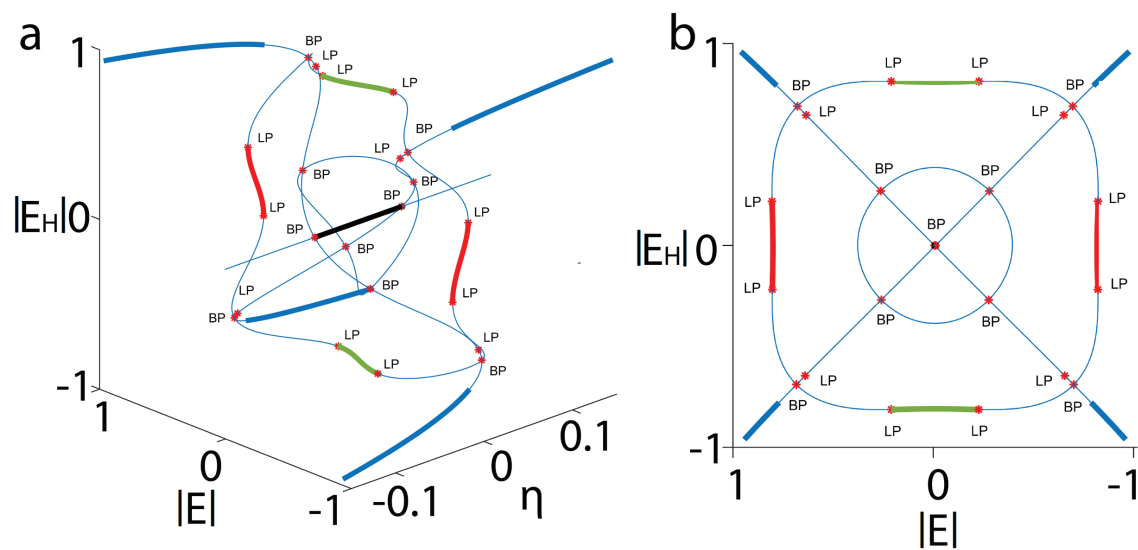


FIGURE 5.4: a) Stationary amplitude of the laser field for both the first ($|E|$) and the second ($|E_H|$) laser versus the coupling strength. The thick line represent the stable interval. Active and passive states of initial conditions for the first and the second laser respectively, are denoted by the red color and the opposite case by the green color. Passive and passive states are denoted by the black color. The (LP) notation indicates a saddle-node bifurcation where the (BP) a pitchfork bifurcation. b) The top view of (a). The values of the fixed parameters are: $\gamma = 0.003125$, $\beta = 0.0512$, $P = 1.66$, $a = 5.8$, $B = 0.37$ and $f = -0.6$.

the amplitude of the electric field, for the first laser remain stable in the passive state and for second laser remain stable in the active state. Then, at a critical coupling strength ($\eta = \pm 0.008819$), a saddle-node bifurcation (LP) occurs and the amplitude of the electric field of laser in the passive state reaches the amplitude of the active state. For the third case (black color) both the amplitude of the electric field of the first and the second laser remain in the passive state until another coupling strength ($\eta = \pm 0.04922$) where a sub-critical pitchfork bifurcation (BP) occurs and the amplitude of the electric field of two lasers moves in the active state. This last case needs much more coupling strength for the whole system to reach the active region than the previous two cases where the amplitude of the electric field of one laser was, from the beginning, in the active region. In the final case, if the initial conditions of the amplitude of the electric field are in the active state for both lasers, they remain there for any value of the coupling strength.

We point out that fixed points where Hopf bifurcations occur have also been observed. They appears slightly before each branch point as is shown in Fig. 5.4. In Fig. 5.5 we have plotted the limit cycle that had been created versus the coupling strength. The area between the two red curves depicts the stable zone. This has been done numerically and we have shown that the limit cycle is stable for a very thin region of coupling strength ($\eta_{final} - \eta_{initial} \sim 0.001$) with small amplitude ($E_{max} - E_{min} \sim 0.1$). For more clarity, in Fig. 5.6 we have calculated the Floquet multipliers of the periodic orbit. If the absolute value of these multipliers is less than one, then the limit cycle is stable, otherwise is always unstable. The red line is the barrier between the stable and unstable periodic orbit and as we see the stable area is too thin. For this reason, in our study, these phenomena are considered negligible.

5.4 Star network of coupled lasers

In this section we look for stationary patterns, in a large system where the geometry of the interaction between the lasers follows a star network configuration (a node in the center to be interacting with each laser in the periphery). Equations 5.7 for a star network can be reformulated as,

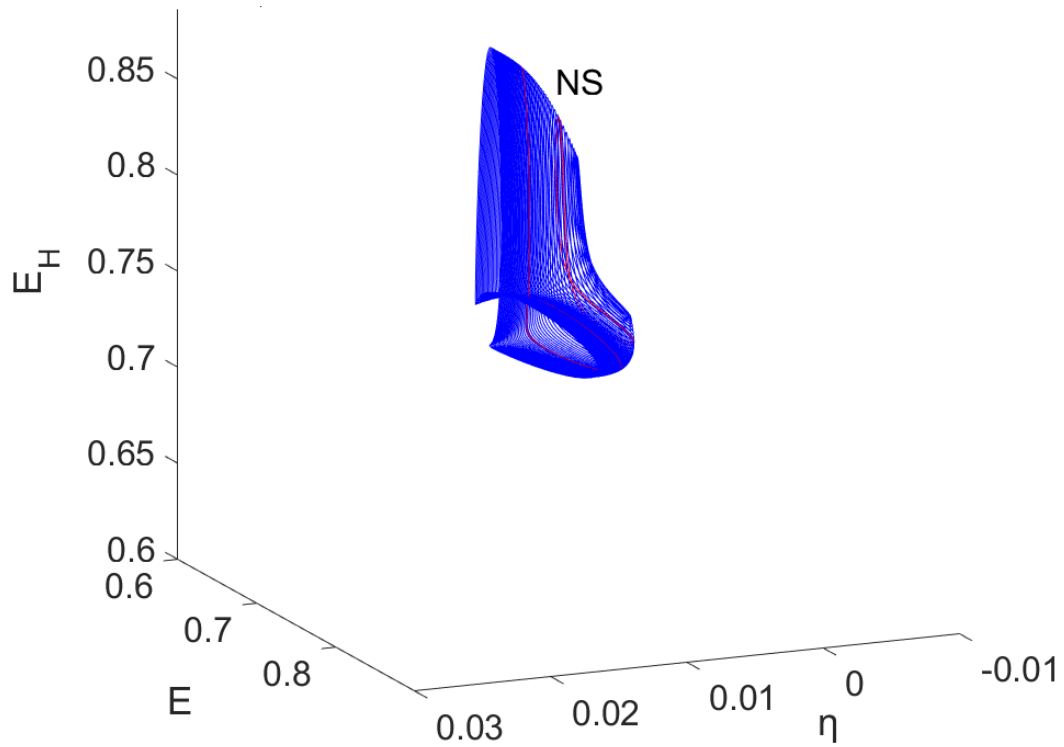


FIGURE 5.5: The limit cycle after the Hopf bifurcation before each branch point as is shown in Fig. 5.4.

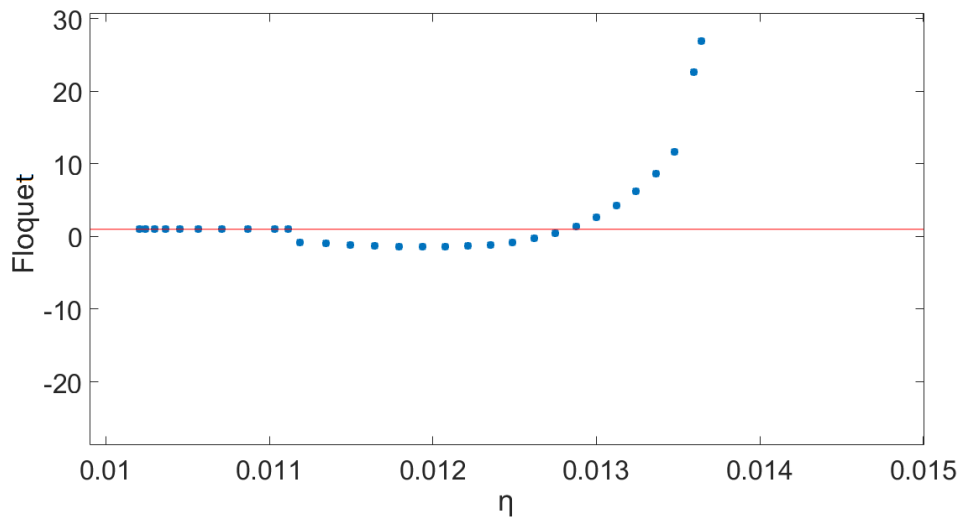


FIGURE 5.6: The Floquet multipliers for the limit cycles as is shown in Fig. 5.5.

$$\begin{aligned}
\frac{dE_j}{dt} &= \frac{E_j}{2}(G_j - 1 - a \sin^2(V_j)) - \eta E_H \\
\frac{dE_H}{dt} &= \frac{E_H}{2}(G_H - 1 - a \sin^2(V_H)) - \eta \sum_{j=1}^N E_j
\end{aligned} \tag{5.9}$$

where $j = 1, 2, 3, \dots, (N)$ and N is the size of the periphery and H is the central node. In polar coordinates where $E = |E|e^{i\phi}$ the coupled periphery-hub system becomes,

$$\begin{aligned}
\frac{d|E_j|}{dt} &= \frac{1}{2}|E_j| \left[G_j - 1 - a \sin^2(V_j) \right] - \eta |E_H| \cos(\theta_j) \\
\frac{d|E_H|}{dt} &= \frac{1}{2}|E_H| \left[G_H - 1 - a \sin^2(V_H) \right] - \eta \sum_{j=1}^N |E_j| \cos(\theta_j) \\
\frac{d\theta_j}{dt} &= \eta \left[\frac{|E_H|}{|E_j|} \sin(\theta_j) + \sum_{k=1}^N \frac{|E_k|}{|E_H|} \sin(\theta_k) \right]
\end{aligned} \tag{5.10}$$

where $\theta_j = \phi_H - \phi_j$ and $k = 1, 2, 3, \dots, (N)$. The evolution in time of variables G_j, V_j, G_H, V_H has the same form with Eq. 5.1.

We have integrated Eq. 5.10 by using a fourth order Runge-Kutta algorithm. We have used parameter values where the bias voltage applied to the modulator for each laser is constant ($B=0.37$) and random initial conditions in phases. Numerical calculations with initial conditions in amplitude of the electric field chosen to be in the passive (where $|E| \approx 0$) or the active (where $|E| \approx \sqrt{P-1}$) state, have shown that, for $\eta > 0.001$, in the whole $N - \eta$ parameters plane the phase difference θ_j , after a small time interval, remains constant and equal to zero.

To show that fact we calculate a phase order parameter which is defined as:

$$\Delta_q = \left\langle \frac{1}{N} \left| \sum_{j=1}^N e^{\theta_j - (j-1)q} \right| \right\rangle \tag{5.11}$$

which is unity for the fully ordered system, and zero when the system

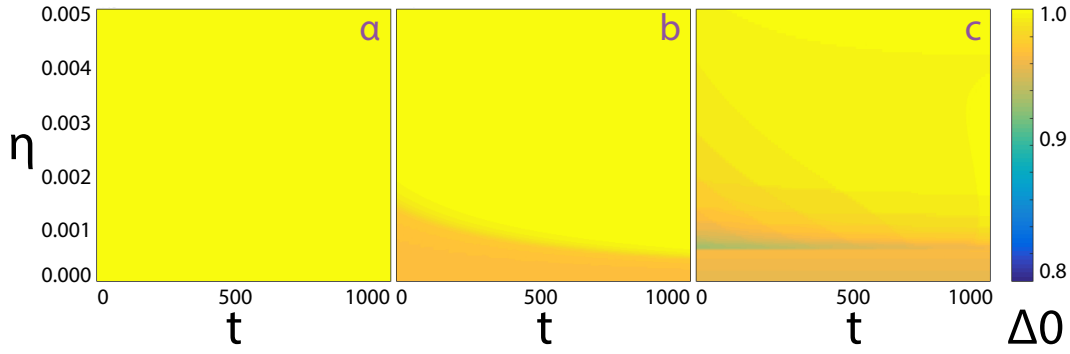


FIGURE 5.7: Order parameter Δ_0 in the η - t space for $N = 10$. a) The system starts with periphery passive-hub active, b) periphery passive-hub passive and c) periphery active-hub passive. Other parameters as in Fig.5.4.

is completely disordered. Here, q is the expected phase difference between oscillators and the average is over realizations of different, random initial conditions θ_j (see [Giver et al., 2011]). In our case the phase differences converge to zero, hence the q parameter is zero. In Fig. 5.7 we have calculated Δ_0 in the η - t space for $N = 10$ and after a relaxation time interval equal to 1000. The average has been computed over 100 different initial conditions in a range from $-\pi$ to π . As we can see, for $\eta > 0.001$ the phase order parameter $\Delta_0 \sim 1$. This is true over the three initial preparations of the system (periphery active-hub passive, periphery passive-hub active or periphery passive-hub passive). This means that the phases between the hub and all the periphery nodes are locked. This result allows us to assume that the system, after a relaxation time interval, reaches a full symmetry where $\theta_j = 0$ and all peripheral nodes can obey the steady state with the same equation and thus the index j can be dropped.

In the presence of these results, Eq. 5.10, can be reduced into this form:

$$\begin{aligned} \frac{d|E|}{dt} &= \frac{1}{2}|E| \left[G - 1 - a \sin^2(V) \right] - \eta |E_H| \\ \frac{d|E_H|}{dt} &= \frac{1}{2}|E_H| \left[G_H - 1 - a \sin^2(V_H) \right] - \eta N |E| \end{aligned} \quad (5.12)$$

The stationary solution for this system, after some algebra, implies the condition:

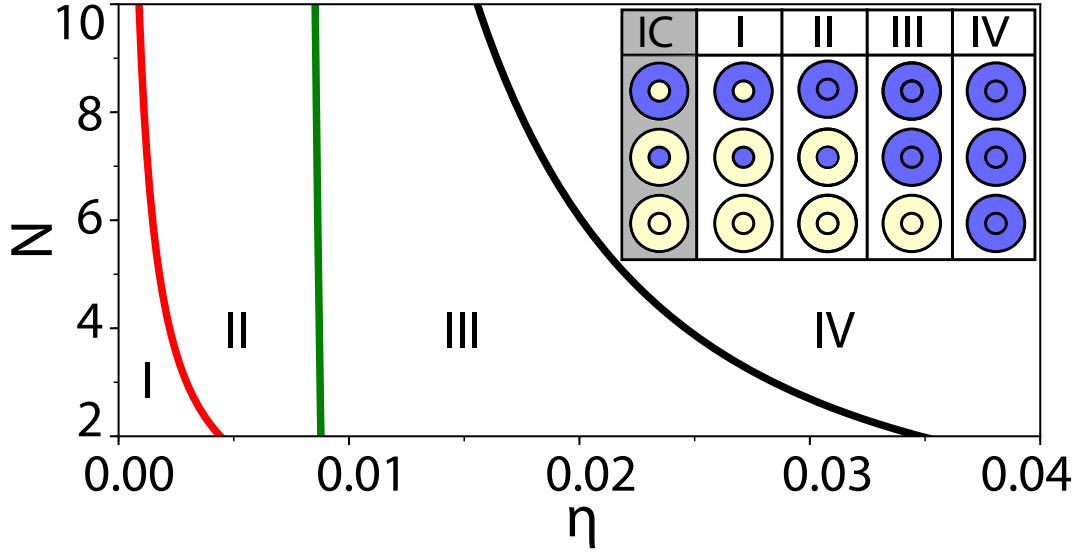


FIGURE 5.8: Phase diagram in the η - N parametric space. Four dynamical regions are separated by curves that correspond to the continuation of the bifurcation points shown in Fig.5.4 using the same colors (red and green are saddle-node bifurcations, while black curve is a pitchfork). In region *I* the coupling is weak enough and all three initial conditions (IC) shown in the inset are stable and constitute steady states of the system. In region *II* the active periphery drifts the hub to the active state. In region *III* the active hub drifts the periphery in the active state. In region *IV* the whole network goes to the active state. In the inset the inner circle represents the hub and the outer circle represents the periphery, while the active state is denoted with blue color and the passive state with yellow. Other parameters are $\gamma = 0.003125$, $\beta = 0.0512$, $P = 1.66$, $a = 5.8$, $B = 0.37$ and $f = -0.6$.

$$\begin{aligned}
 \frac{P}{1 + |E|^2} - 1 - a \sin^2 (B + f|E|^2) &= 2\eta \frac{|E_H|}{|E|} \\
 \frac{P}{1 + |E_H|^2} - 1 - a \sin^2 (B + f\epsilon_H^2) &= 2\eta N \frac{|E|}{|E_H|}
 \end{aligned} \tag{5.13}$$

Stability analysis of Eq. 5.12 has been done again by the MatCont software. The continuations of the (Fig. 5.4) bifurcations over the size parameter N has been shown in Fig. 5.8. We plot with the same color the curves which have been calculated as a continuation of the corresponding bifurcation point in any of three cases as we mentioned in the section of the two coupled lasers. In this size-coupling strength diagram there are four distinct regions. In the

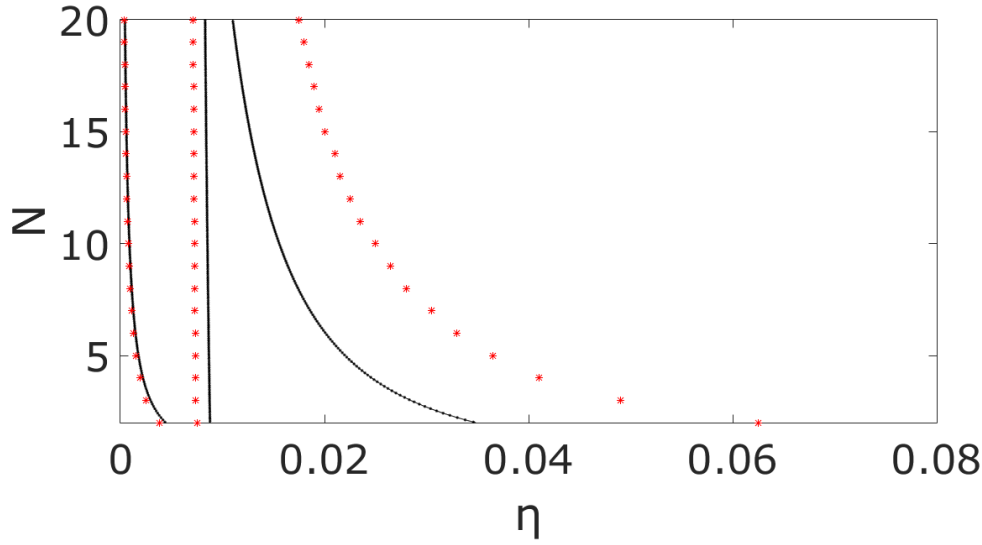


FIGURE 5.9: Phase diagram in the $\eta - N$ parametric space as in Fig.5.8. The black solid lines correspond to the continuation of the steady states calculated by the Matcont while the red points depict the results from the brutal, fourth order Runge-Kutta integration method of the system.

first region which is marked by the letter *I*, any initial state (periphery active-hub passive, periphery passive-hub active or periphery passive-hub passive) remains as it is. In the region *II* the active periphery drifts the hub in the active state where in the region *III* the active hub drifts the periphery in the active state. Finally, in the region *IV* any initial state moves in the active state. In the panel inside the figure we present the whole four cases in a schematic form. The outer circle represents the periphery of the system while the inner represents the hub. The color difference separates the active region (dark) from the passive one (light).

Moreover, brute-force numerical integrations using the fourth order Runge-Kutta algorithm leads to the same behaviour (see Fig. 5.9 shown). We have calculated for the central node the temporal mean of its intensity ($\langle I_H \rangle_t$), where $\langle . \rangle_t$ is the average over a time window of length $T = 1000$ after $T = 1000$ relaxation time. For the periphery, apart from the temporal mean of each laser intensity, we have made a calculation on the average over the whole size of periphery nodes ($I_p = \frac{1}{M} \sum_{j=1}^M I_j$) and then on the temporal mean ($\langle I_p \rangle_t$) like with the hub case. In a $N - \eta$ diagram, the borders between the active and the passive regions in the three cases of initial conditions (red points) coincide with the curves of Fig. 5.8 (black lines). The

deviation between the two calculations comes due to the very long time integration that is required from the Runge-Kutta method to approach the steady state of the MatCont continuation.

5.5 Conclusions

We have numerically demonstrated a bistable star network of coupled class B lasers that supports stationary patterns and activation spreading determined by the number of coupled lasers to the central unit, by the coupling strength, and the initial conditions. This has been implemented for a dynamical system of coupled CO_2 laser with optoelectronic feedback keeping the bias voltage applied to the modulator constant and by considering the coupling strength as a control parameter. After careful numerical calculations, the phase difference between the central laser and any peripheral unit has been locked after a very small time interval allowing us to investigate only the steady state of the system. In a system size-coupling strength diagram we demonstrate four distinct regions. A stationary activation between the peripheral and central elements, a spreading activation where the activated periphery turns on the center element, the activated center drifts the periphery into the active region, and an activating of the whole system from the passive into the operative region.

Conclusions

In this thesis we studied various spatio-temporal patterns in arrays of coupled lasers. The dynamics of the system in all cases was modeled by the rate equations for type B lasers. The derivation of this model has been done in Chapter 1 through the semi-classical approach by treating the electromagnetic field purely classically and the active medium as a quantum system.

A brief presentation of the theory of synchronization has been presented in Chapter 2. We have stressed the presence of a peculiar phenomenon, namely the chimera states where a spatio-temporal pattern of a system with identical natural frequencies oscillators, splits into coexisting regions of locked and unlocked phases.

These two chapters are useful for the theoretical background in what follows. In the next three chapters we present the main results of our work. To be more precise, in Chapter 3 we have found amplitude chimera states in a large one-dimensional network of semiconductor lasers by properly modifying the optical frequency detuning. Local coupling is sufficient to generate these states even for large noise in detuning fluctuations from the linear distribution. By using suitable classification measures we have quantified the observed dynamics. A systematic study in the optical frequency detuning and coupling strength parameter space, shows that the region of chimera states lies between full synchronization and desynchronization.

Multi-clustered chimera states have been obtained and characterized in large arrays of semiconductor class B lasers with nonlocal interactions, in Chapter 4. The observed chimeras display the coherence and incoherence patterns in both the amplitude and phase of the electric field. In addition, other spatiotemporal dynamics including wave-like spatial structures and

spatially localized oscillations (breathers) are possible. The crucial parameters for the collective behavior are the complex coupling strength and the nonlocal coupling range. The latter is responsible for the multiplicity of the (in)coherent domains of the obtained chimeras which has not been observed neither for local nor for global coupling. Our study addresses the effect of nonlocal coupling in large laser arrays for the first time, providing a direction for various technological applications.

Finally, we have numerically demonstrated a bistable star network of coupled class B lasers that supports stationary patterns and activation spreading determined by the number of coupled lasers to the central unit, by the coupling strength and the initial conditions. What we have observed is stationary activation between the peripheral and the central elements, a spreading activation of the activated periphery through the center element, a spreading activation from the active center to the peripheral inactivated lasers and an activation of the whole system from the passive into the operative region.

For future studies it would be worthwhile to explore the effects introduced by noise through the spontaneous emission of the active media. This can be done by adding into the equation an extra term of white noise with a proper amplitude and an independent uncorrelated noise source with a Gaussian distribution. Another very important parameter is the laser pump power which is the most conveniently accessible control framework in chip scale diode systems. The activation of a laser which is pumping below the threshold can arrive through its coupling with the other emitters. This phenomena may have multiple technological applications and is our next goal to investigate.

Moreover, the theoretical model of a bistable network of coupled lasers with an intracavity electro-optic modulator we use in Chapter 5 has many similarities to that obtained by semiconductor lasers with a saturable absorber inside the cavity. Our model of CO_2 lasers has a disadvantage regarding the large size of each individual laser. Our next study will be the extraction of the same results as in CO_2 model in systems that are composed by semiconductor lasers and their investigation close to the Hopf bifurcation. The effect of the star geometry on coupled lasers configuration with respect to the information spreading from one component to the other, may prove to be a useful tool for various technological applications.

Publications

Shena, J., Hizanidis, J., Kovanis, V. and Tsironis, G. P. *Turbulent chimeras in large semiconductor laser arrays*. Sci Rep, 42116, 7. 2017.

Shena, J. Hizanidis, J., Hövel, P. and Tsironis, G. P. *Multiclustered chimeras in large semiconductor laser arrays with nonlocal interactions*. Phys Rev E, 32215, 3, 96. 2017.

Shena, j., Kouvaris N. E., Hizanidis, J., and Tsironis, G. P. *Class B lasers in star networks with optoelectronic feedback*. (In preparation). 2018.

Appendix A

Chimeras classification

A.1 The chimeras temporal classification scheme

Except from the space measurements as the discrete Laplacian D and the normalized probability density function g_0 , there are additional temporal measurements which provide valuable information for a distinction between different chimera dynamics. Suppose we have two time series X_i and X_j , real or complex, with mean values μ_i and μ_j and standard deviations σ_i and σ_j . Then, we can define the correlation coefficients in the form (see [Kemeth et al., 2016]):

$$p_{ij} = \frac{\langle (X_i - \mu_i)^*(X_j - \mu_j) \rangle_t}{\sigma_i \sigma_j} \quad (\text{A.1})$$

where with $\langle \cdot \rangle_t$ we indicate the temporal mean and with $*$ the complex conjugation. The value $p_{ij} = 1$ corresponds to linear correlation time series where $p_{ij} = -1$ characterizes linear anti-correlation time series. In our system, for the case of turbulent chimeras (see Fig. 3.5 bottom (b)) the calculation of p_{ij} is shown in Fig. A.1. The next step is to construct the distribution function h of the absolute values $|p_{ij}|$ as is shown in Fig. A.2. This quantity is a measure for the correlation in time. For static chimera states, where the coherent cluster is localized at the same position over time, $h(|p_{ij}|)$ is non-zero. In practice, we consider two time series or two lasers as correlated if $|p_{ij}| > 0.99 = \gamma$. The percentage of the time-correlated oscillators can now

be quantified as in the case of density function g_0 , with:

$$h_0 = \sqrt{\int_{\gamma}^1 h(|p|) dp} \quad (\text{A.2})$$

Note that h_0 does not always reflect the size of the synchronized cluster. This is especially the case when coherent and incoherent regimes are non-static and perform spatial movements over time. Then, h_0 is much smaller than $g_0(t)$ and may vanish for large enough time windows. So, for a static chimera $h_0 > 0$ and for a moving chimera $h_0 \sim 0$. In our case we take a result where $h_0 = 0.03$. This means that our chimera is moving turbulent.

Now we have all the tools to classify any chimera behavior. For a chimera state the spacial probability density function holds values between zero and one $0 < g_0 < 1$. Then, three more subsections take place.

(1) Stationary chimera: Chimera states with constant coherent cluster size $g_0(t)$. (2) Turbulent chimera: Chimera states where the temporal evolution of $g_0(t)$ is irregular (3) Breathing chimera: States in which the behavior of $g_0(t)$ is periodic.

Based on the temporal correlation measure h_0 , these groups can be further divided into three subclasses:

(a) Static chimera, in which the coherent cluster is confined to the same position in space over time. That means, h_0 is non-zero and independent of the time window evaluated. (b) Moving chimera, where h_0 vanishes if the regarded time window is taken sufficiently large. (c) Time-coherent chimera, that is chimera states with no temporal incoherence and thus $h_0 = 1$.

Examples: In the non-locally coupled Stuart-Landau oscillators investigated by [Bordyugov et al., 2010] and in chimera states in a non-locally coupled version of the complex Ginzburg-Landau equation.[Sethia et al., 2013], a snapshot and the observables $g_0(t)$ and h_0 of the latter are depicted in Fig. A.3 (a) and (b), respectively. For this system $g_0(t)$ is constant and $h_0 > 1$, so according to our definition above, this chimera state is a static stationary chimera. Another example is the so-called type II chimera, which was reported in the CGLE with nonlinear global coupling.[Schmidt et al., 2014].

The temporal evolution of the absolute value of the complex amplitude and the observables $g_0(t)$ and h_0 are depicted in Fig. A.3 (c) and (d), respectively. The oscillatory behavior of $g_0(t)$ and the value of h_0 above zero indicates breathing static chimeras. Finally, in our system, the temporal evolution of the absolute value of the electric field and $g_0(t), h_0$ measurements are shown in Fig. A.3 (e) and (f) pointing out a turbulent moving chimeras due to the fact that g_0 has an irregular evolution and $h_0 \sim 0$.

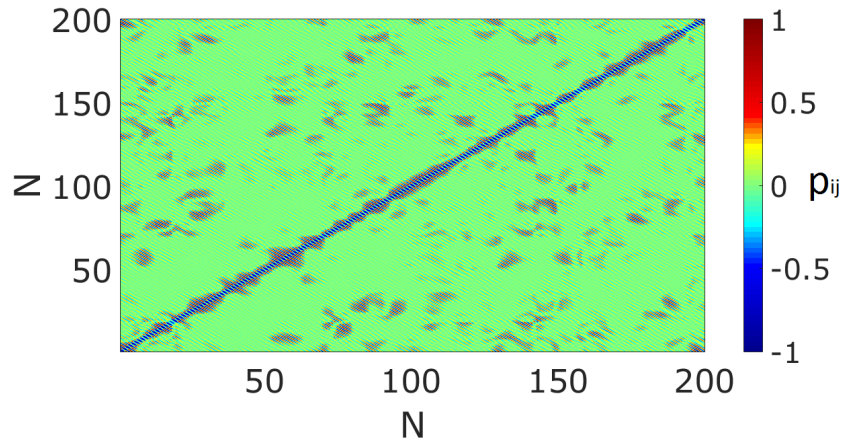


FIGURE A.1: The correlation coefficients p_{ij} for the case of turbulent chimeras (see Fig. 3.5 bottom (b)).

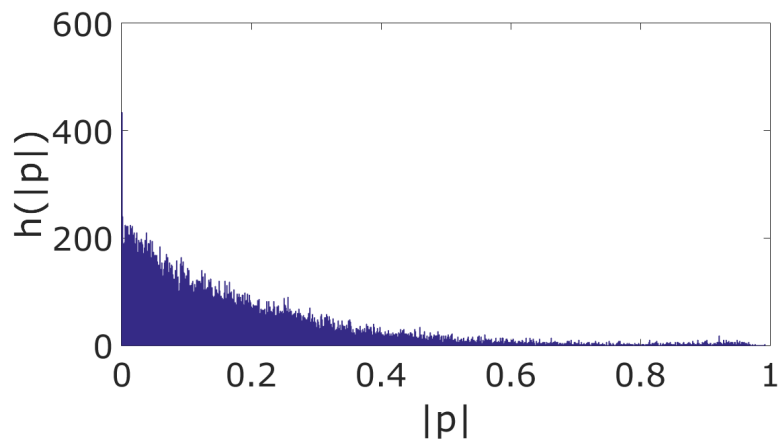


FIGURE A.2: The distribution function h of the absolute values $|p_{ij}|$.

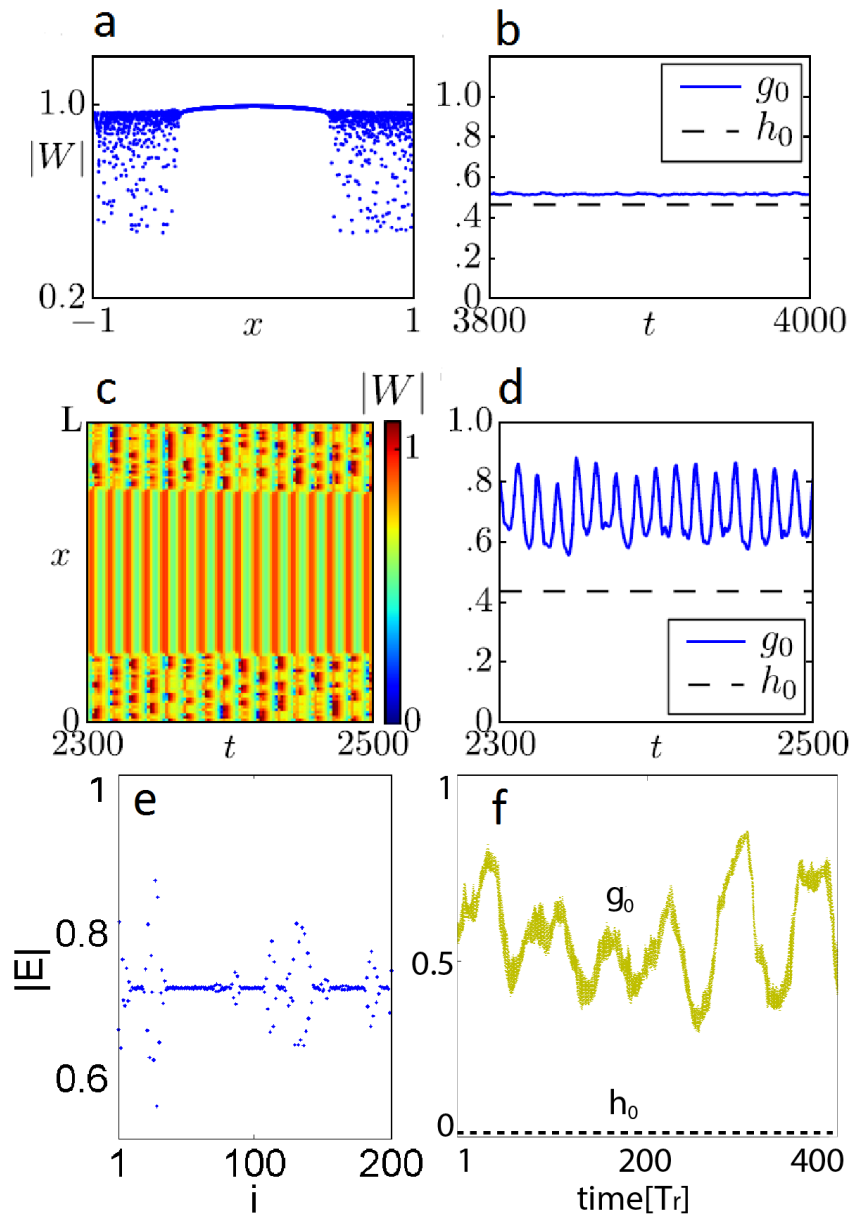


FIGURE A.3: (a) Snapshot of the amplitude of the amplitude-mediated chimera, (c) Temporal evolution of the modulus, (e) Snapshot of the amplitude of electric field. (b), (d) and (f) $g_0(t)$ and h_0 from the data shown in (a),(d) and (f).

Bibliography

- Abrams, D. M. et al. (2008). "Solvable model for chimera states of coupled oscillators". In: *Physical Review Letters* 101.8, pp. 1–4.
- Agrawal, G. et al. (1986). *Long wavelength semiconductor lasers*. Van Nostrand Reinhold Co. Inc., New York, NY.
- Alsing, P. et al. (1996). "Lang and Kobayashi phase equation." In: *Physical review A* 53.6, pp. 4429–4434. URL: <http://www.ncbi.nlm.nih.gov/pubmed/9913417>.
- Andronov, A. A. et al. (1949). *Theory of Oscillators*. 1st ed. Press, Princeton University.
- Arecchi, F. et al. (1984). "Deterministic chaos in laser with injected signal". In: *Optics Communications* 51, pp. 308–314.
- Arkady, P. et al. (2001). *Synchronization (A universal concept in nonlinear sciences)*. 1st ed. Cambridge University Press.
- Blackbeard, N. et al. (2014). "From synchronisation to persistent optical turbulence in laser arrays". In: *Physica D* 43, pp. 286–287.
- Böhm, F. et al. (2015). "Amplitude-phase coupling drives chimera states in globally coupled laser networks". In: *Physical Review E - Statistical, Nonlinear, and Soft Matter Physics* 91.4, pp. 1–6.
- Bordyugov, G. et al. (2010). "Self-emerging and turbulent chimeras in oscillator chains". In: *Physical Review E - Statistical, Nonlinear, and Soft Matter Physics* 82.3, pp. 1–4.
- Bourmpos, M. et al. (2012). "Sensitivity analysis of a star optical network based on mutually coupled semiconductor lasers". In: *J Light Technol* 30.16, pp. 2618–2624.
- Brunner, D. et al. (2015). "Reconfigurable semiconductor laser networks based on directive coupling". In: *Optics Letters* 40, p. 3854.
- Chen, D. et al. (1996). "Breather Mobility in Discrete Nonlinear Lattices". In: *Phys Rev Lett* 77.23, pp. 4776–4779.

- Crook, S. M. et al. (1997). "The role of axonal delay in the synchronization of networks of coupled cortical oscillators". In: *Journal of Computational Neuroscience* 4.2, pp. 161–172.
- Dahms, T. (2011). "Synchronization in Delay-Coupled Laser Networks". In: *Naturwissenschaften*.
- Dahms, T. et al. (2012). "Cluster and group synchronization in delay-coupled networks". In: *Physical Review E* 86, p. 16202.
- Daido, H. (1992). "Order function and macroscopic mutual entrainment in uniformly coupled limit-cycle oscillators". In: *Prog Theor Phys* 88.6, pp. 1213–1218.
- (1993). "Critical Conditions of Macroscopic Mutual Entrainment in Uniformly Coupled Limit-Cycle Oscillators". In: *Progress of theoretical physics* 89.4, pp. 929–934.
- Dubbeldam, J. L. A. et al. (1999). "Self-pulsations of lasers with saturable absorber: dynamics and bifurcations". In: *Opt Commun* 159.4-6, pp. 325–338.
- Ermentrout, G. B. et al. (1984). "Frequency Plateaus in a Chain of Weakly Coupled Oscillators, I." In: *SIAM Journal on Mathematical Analysis* 15.2, pp. 215–237.
- Erneux, T. et al. (2010). *Laser Dynamics*. Cambridge University Press.
- Fabiny, L. et al. (1993). "Coherence and phase dynamics of spatially coupled solid-state lasers". In: *Phys Rev A* 47.5, pp. 4287–4296.
- Giver, M. et al. (2011). "Phase and frequency entrainment in locally coupled phase oscillators with repulsive interactions". In: *Physical Review E - Statistical, Nonlinear, and Soft Matter Physics*.
- González-Avella, J. C. et al. (2014). "Localized coherence in two interacting populations of social agents". In: *Phys A Stat Mech its Appl* 399, pp. 24–30.
- Hagerstrom, A. M. et al. (2012). "Experimental observation of chimeras in coupled-map lattices". In: *Nature Physics* 8, pp. 658–661.
- Hall, D. et al. (1970). "Optical Guiding and electro-optic modulation in GaAs epitaxial layers". In: *Optics Communications* 1.9, pp. 403–405.
- Heck, M. J. (2013). "Hybrid silicon photonic integrated circuit technology". In: *Journal Of Selected Topics In Quantum Electronics* 19, p. 6100117.
- Hizanidis, J. et al. (2016). "Chimera-like states in modular neural networks". In: *Scientific Reports* 6, p. 19845.
- Johnson, M. T. et al. (2013). "High-speed beam steering with phased vertical cavity laser arrays". In: *Journal Of Selected Topics In Quantum Electronics* 19, p. 1701006.

- Junges, L. et al. (2015). "Stability diagrams for continuous wide-range control of two mutually delay-coupled semiconductor lasers". In: *New Journal of Physics* 17.5, p. 053038.
- Kao, T. Y. et al. (2016). "Phase-locked laser arrays through global antenna mutual coupling". In: *Nature Photonics* 10, p. 1038.
- Katz, J. et al. (1984). "Coupling coefficient of gain-guided lasers". In: *Applied Optics* 23.14, pp. 2231–2233.
- Kemeth, F. P. et al. (2016). "A classification scheme for chimera states". In: *Chaos* 26, p. 94815.
- Khanin, Y. I. (1995). *Principles of Laser dynamics*. Ed. by ELSEVIER SCIENCE. 1st Editio. ISBN: 9780444598875.
- Kouvaris, N. E. et al. (2012). "Traveling and Pinned Fronts in Bistable Reaction-Diffusion Systems on Networks". In: *PLoS ONE* 7.9.
- Kouvaris, N. E. et al. (2013). "Feedback-induced stationary localized patterns in networks of diffusively coupled bistable elements". In: *Epl* 102.1.
- Kouvaris, N. E. et al. (2016). "Chimera states in a network-organized public goods game with destructive agents". In: *Chaos* 26.12, pp. 1–8.
- Kouvaris, N. E. et al. (2017). "Stationary patterns in star networks of bistable units: Theory and application to chemical reactions". In: *Physical Review E* 95.4, pp. 1–8.
- Kozyreff, G. et al. (2000). "Global coupling with time delay in an array of semiconductor lasers". In: *Physical Review Letters* 85, p. 3809.
- Kozyreff, G. et al. (2001). "Dynamics of a semiconductor laser array with delayed global coupling". In: *Phys Rev E* 64.1, p. 16613.
- Kuramoto, Y. (1984). *Chemical Oscillations, Waves, and Turbulence*. Vol. 19. Springer Series in Synergetics. Berlin, Heidelberg: Springer Berlin Heidelberg, p. 158.
- Kuramoto, Y. et al. (2002). "Coexistence of Coherence and Incoherence in Nonlocally Coupled Phase Oscillators". In: 4, pp. 380–385.
- Kuske, R. et al. (1997). "Full length article Localized synchronization of two coupled solid state lasers". In: 39.
- Laing, C. R. (2009). "The dynamics of chimera states in heterogeneous Kuramoto networks". In: *Phys D Nonlinear Phenom* 238.16, pp. 1569–1588.
- Laing, C. R. et al. (2012). "Chimeras in random non-complete networks of phase oscillators". In: *Chaos* 22.1.
- Landau, L. D. et al. (1977). *Quantum Mechanics*. 3rd ed. Butterworth-Heinemann.
- Lang, R. et al. (1980). "External Optical Feedback Effects on Semiconductor Injection Laser Properties". In: *IEEE Journal of Quantum Electronics* 16.3, pp. 347–355.

- Larger, L. et al. (2013). "Virtual Chimera States for Delayed-Feedback Systems". In: *Phys Rev Lett* 111.5, p. 54103.
- (2015). "Laser chimeras as a paradigm for multistable patterns in complex systems". In: *Nature Communications* 6, p. 7752.
- Lythe, G. et al. (1997). "Low pump limit of the bifurcation to periodic intensities in a semiconductor laser subject to external optical feedback". In: *Physical Review A* 55, pp. 4443–4448.
- Ma, R. et al. (2010). "Robust features of chimera states and the implementation of alternating chimera states". In: *Epl* 91.4.
- MacKay, R. S. et al. (1994). "Proof of existence of breathers for time-reversible or Hamiltonian networks of weakly coupled oscillators". In: *Nonlinearity* 7.6, pp. 1623–1643.
- Martens, E. A. et al. (2013). "Chimera States in Mechanical Oscillator Networks". In: 110.26, pp. 10563–10567.
- Meucci, R. et al. (2002). "Chaotic function generator: Complex dynamics and its control in a loss-modulated Nd:YAG laser". In: *Phys Rev E - Stat Physics, Plasmas, Fluids, Relat Interdiscip Top* 66.2, pp. 1–10.
- Motter, A. E. et al. (2013). "Spontaneous synchrony in power-grid networks". In: *Nature Physics* 9.3, pp. 191–197.
- Nagourney, W. (2014). *Quantum Electronics for Atomic Physics and Telecommunication*. 2nd ed. Oxford University Press.
- Nixon, M. et al. (2012). "Controlling synchronization in large laser networks". In: *Physical Review Letters* 108.21.
- Nixon, M. et al. (2013). "Observing Geometric Frustration with Thousands of Coupled Lasers". In: *Phys Rev Lett* 110.18, p. 184102.
- Nkomo, S. et al. (2016). "Chimera and chimera-like states in populations of nonlocally coupled homogeneous and heterogeneous chemical oscillators". In: *Chaos* 26.9, pp. 1–5.
- Okuda, K. (1993). "Variety and generality of clustering in globally coupled oscillators". In: *Physica D: Nonlinear Phenomena* 63.3-4, pp. 424–436.
- Oliva, R. A. et al. (2001). "Dynamics of a large array of globally coupled lasers with distributed frequencies". In: *International Journal Of Bifurcation And Chaos* 11, p. 2359.
- Omelchenko, I. et al. (2013). "When Nonlocal Coupling between Oscillators Becomes Stronger: Patched Synchrony or Multichimera States". In: *Phys Rev Lett* 110.22, p. 224101.

- Omel'Chenko, O. E. et al. (2010). "Chimera states as chaotic spatiotemporal patterns". In: *Physical Review E - Statistical, Nonlinear, and Soft Matter Physics* 81.6, pp. 3–6.
- Pecora, L. M. et al. (2014). "Cluster synchronization and isolated desynchronization in complex networks with symmetries". In: *Nature Communications* 5, p. 4079.
- Pierre, M. et al. (2007). *Elements of Quantum Optics*. 4th ed. Springer.
- Rogister, F. et al. (2007). "Localized excitations in arrays of synchronized laser oscillators". In: *Physical Review Letters* 98.10, pp. 1–4.
- Röhm, A. et al. (2016). "Small chimera states without multistability in a globally delay-coupled network of four lasers". In: *Physical Review E* 94, p. 42204.
- Schmidt, L. et al. (2014). "Coexistence of synchrony and incoherence in oscillatory media under nonlinear global coupling". In: *Chaos (Woodbury, NY)* 24.1, p. 013102.
- Sethia, G. C. et al. (2013). "Amplitude-mediated chimera states". In: *Physical Review E - Statistical, Nonlinear, and Soft Matter Physics* 88.4, pp. 1–5.
- Silber, M. et al. (1993). "Stability results for in-phase and splay-phase states of solid-state laser arrays". In: *J Opt Soc Am B* 10.6, pp. 1121–1129.
- Soriano, M. C. et al. (2013). "Complex photonics: Dynamics and applications of delay-coupled semiconductor lasers". In: *Reviews of Modern Physics* 85.1, pp. 421–470.
- Strogatz, S. H. (1994). *Nonlinear Dynamics And Chaos*. 1st ed. Addison-Wesley Publishing Company.
- (2000). "From Kuramoto to Crawford: exploring the onset of synchronization in populations of coupled oscillators". In: *Physica D: Nonlinear Phenomena* 143.1-4, pp. 1–20.
- Tartwijk, G. H. M. V. et al. (1995). "Semiconductor lasers with optical injection and feedback". In: ... *J Eur Opt* ... 87.
- Thornburg, K. S. et al. (1997). "Chaos and coherence in coupled lasers". In: *Phys Rev E* 55.4, pp. 3865–3869.
- Tinsley, M. R. et al. (2012). "Chimera and phase-cluster states in populations of coupled chemical oscillators". In: *Nat Phys* 8, pp. 662–665.
- Uchida, A. et al. (2001). "Chaotic antiphase dynamics and synchronization in multimode semiconductor lasers". In: *Physical Review A* 64, p. 23801.
- Wang, S. S. et al. (1988). "Dynamics of phase-locked semiconductor laser arrays". In: *Applied Physics Letters* 52.21, pp. 1774–1776.
- Watanabe, S. et al. (1993). "Integrability of a globally coupled oscillator array". In: *Phys Rev Lett* 70.16, pp. 2391–2394.

- Wieczorek, S. et al. (2002). "Global quantitative predictions of complex laser dynamics". In: *Physical Review E - Statistical Physics, Plasmas, Fluids, and Related Interdisciplinary Topics* 65.4, p. 4.
- Wieczorek, S. et al. (2005). "The dynamical complexity of optically injected semiconductor lasers". In: *Physics Reports* 416, pp. 1–128.
- Winful, H. G. (1992). "Instability threshold for an array of coupled semiconductor lasers". In: *Phys Rev A* 46, p. 6093.
- Winful, H. G. et al. (1988). "Stability of phase locking in coupled semiconductor laser arrays". In: *Applied Physics Letters* 53, p. 1894.
- Winful, H. G. et al. (1990). "Synchronized chaos and spatiotemporal chaos in arrays of coupled lasers". In: *Phys Rev Lett* 65.13, pp. 1575–1578.
- Yamada, M. (1993). "A theoretical analysis of self-sustained pulsation phenomena in narrow stripe semiconductor lasers". In: *IEEE J Quantum Electron* QE-29.5, pp. 1330–1336.
- Yariv, A. (1989). *Quantum Electronics*. 3rd ed. John Wiley & Sons.
- Ye Wang, P. et al. (1990). "Onset of subcritical bifurcation in a CO₂ laser with feedback". In: *Opt Commun* 80.1, pp. 42–46.
- Zakharova, A. et al. (2014). "Chimera death: Symmetry breaking in dynamical networks". In: *Physical Review Letters* 112, p. 154101.
- Zamora-Munt, J. et al. (2010). "Crowd synchrony and quorum sensing in delay-coupled lasers". In: *Physical Review Letters* 105.26, pp. 18–21.
- Zehnlé, V. (2000). "Theoretical model for coupled solid-state lasers". In: *Phys Rev A* 62.3, p. 33814.